DELFT UNIVERSITY OF TECHNOLOGY

MASTER OF SCIENCE

Operational performance of an offshore piling template

Author:
Ö. B. Ulubaş

June 20, 2017

Operational performance of an offshore piling template

An assessment of the on-bottom stability of the piling template in soft soil strata

by

Ömer Burak Ulubaş

to obtain the degree of Master of Science
at the Delft University of Technology,
to be defended publicly on Tuesday June 20, 2017 at 09:30 AM.

Student number:	4161769	
Thesis committee:	Prof. Dr. A.V. Metrikine,	TU Delft
	Dr. F. Pisanò,	TU Delft
	Ir. J.S. Hoving,	TU Delft
	Ir. T. de Blaeij,	Boskalis
	Ir. J. Bol,	Boskalis
	Ir. P. Hendrickx,	Boskalis

An electronic version of this thesis is available at `http://repository.tudelft.nl/`.

TU Delft

Preface

Executing this thesis study would not be possible without the help and support of a number of people. I would like to express my sincere gratitude to the people who have supported me throughout this thesis work.

First of all, the members of my graduation committee. Federico Pisanò, my daily university supervisor, I am very grateful for the discussions we had, your support, your patience and the many eye-openers. Many thanks to Prof. Dr. Andrei Metrikine for his valuable input during the meetings.

I would like to thank my company supervisors for their guidance during this study. Thijs de Blaeij, my first company supervisor, many thanks for the valuable discussions we had during my time in Boskalis. Joris Bol, my second company supervisor, thank you for the data you provided me. With our fruitful discussions, I gained much practical experience and improved my knowledge on soil behaviour. Peter Hendrickx, thank you for your calm approach and your faith towards me.

Last not but least, I wish to thank my parents, my family and friends for their continuous support and advice. Feyza, many thanks for sharing my issues and your continuous encouragement during this study.

Ömer Burak Ulubaş
Delft, June 2017

Contents

List of Figures

List of Tables

List of Symbols

α	Adhesion	$[-]$
γ	Bulk unit weight	$[kN \cdot m^{-3}]$
γ'	Effective unit weight	$[kN \cdot m^{-3}]$
ν	Poisson ratio	$[-]$
ω	Excitation frequency	$[rad/s]$
ω_n	Natural frequency	$[s]$
$\sigma_{vc'}$	Effective vertical stress	$[kPa]$
σ_{vo}	Total vertical stress	$[kPa]$
φ	Internal friction angle	$[°]$
A	Area	$[m^2]$
a, b, c	Fitting coefficients	$[-]$
B	Breadth	$[m]$
b_c, b_q, b_γ	Modification factor for footing inclination	$[-]$
c	Cohesion	$[kPa]$
c_u	Undrained shear strength	$[kPa]$
D	Diameter	$[m]$
d	Embedment	$[m]$
d_c, d_q, d_γ	Modification factor for embedment	$[-]$
E_u	Undrained Young modulus	$[MPa]$
F	Load	$[kN]$
G	Shear modulus	$[MPa]$
g_c, g_q, g_γ	Modification factor for ground inclination	$[-]$
H	Horizontal load	$[kN]$
h	Normalised horizontal load	$[-]$
H_1	Upper layer thickness	$[m]$
H_d	Ultimate horizontal bearing capacity	$[kN]$
H_s	Significant wave height	$[m]$
H_{ult}	Ultimate horizontal capacity	$[kN]$
i_c, i_q, i_γ	Modification factor for load inclination	$[-]$
$I_{m,y}$	Mass moment of inertia	$[kg \cdot m^{-2}]$

K_p	Passive earth pressure coefficient	$[-]$
K_x, K_y, K_z	Soil spring stiffnesses	$[kN/m]$
L	Length	$[m]$
M	Moment load	$[kN \cdot m]$
m	Mass	$[kg]$
m	Normalised moment load	$[-]$
M_{ult}	Ultimate moment capacity	$[kN \cdot m]$
N_c, N_q, N_γ	Bearing capacity factors	$[-]$
N_{kt}	CPT cone factor	$[-]$
Q	Ultimate vertical bearing capacity	$[kN]$
q	Surcharge	$[kN \cdot m^{-2}]$
q_c	Measured cone resistance	$[kPa]$
Q_d	Ultimate vertical bearing capacity	$[kN]$
q_t	Corrected cone resistance	$[kPa]$
s_c, s_q, s_γ	Modification factor for geometry	$[-]$
s_u	Undrained shear strength	$[kPa]$
s_{u0}	Undrained shear strength at base level	$[kPa]$
T_n	Natural period	$[s]$
T_p	Peak period	$[s]$
U_c	Current velocity	$[m \cdot s^{-1}]$
U_{10}	Wind speed at 10 m height	$[m \cdot s^{-1}]$
V	Vertical load	$[kN]$
v	Normalised vertical load	$[-]$
V_s	Shear wave velocity	$[m/s]$
V_{ult}	Ultimate vertical capacity	$[kN]$

List of Abbreviations

API American Petroleum Institute

CPT Cone Penetration Tests

DNV Det Norske Veritas

EWEA The European Wind Energy Association

ISO International Organisation for Standardization

OSS Offshore Substation

PR Technique Press-Replace technique

SNAME Society of Naval Architects and Marine Engineers

UU Undrained Unconsolidated

WTG Wind Turbine Generator

1

Introduction

In the introduction, the development of the offshore wind industry and an overview of support structures is given to be used for wind turbine generators. Furthermore, the Wikinger Offshore Wind Farm is discussed followed by the installation procedure of the turbines. The problem statement and thesis objective are presented followed by the outline of this study.

1.1. Development of offshore wind industry

Traditional energy resources are on the verge of losing the fight against renewable energy. Although not sufficient clean energy is produced to keep up with the growing energy demand, it becomes increasingly important in which wind energy plays a key role. Limited space onshore, the aversion in the society, especially of environmentalists, against construction of turbines onshore pushed the wind industry to go offshore.

The offshore wind industry has grown significantly in the last decade and will keep growing in the future. Especially 2015 was a great year for the offshore wind industry, in which a total capacity of 11.027 MW was connected to the European grid. In the next decade, another 26.4 GW of consented offshore wind farms are identified that might be constructed and projects with a total capacity of 63.5 GW are presumed to be in the planning phase [18]. As the Heads of State committed to a reduction of the greenhouse gas emissions by 80-95 %, The European Wind Energy Association (EWEA) is in expectation that Europe's energy demand will be met, by both onshore and offshore wind energy, for up to 50 % in 2050 [7].

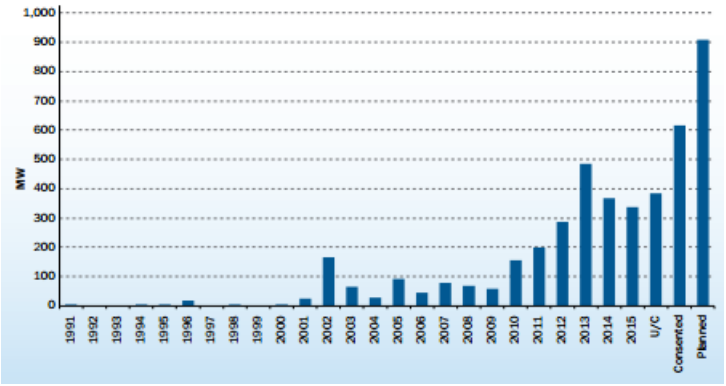

Figure 1.1: Average size of offshore wind farms [18]

The offshore wind industry is a dynamic market, developments are continuously on-going in the field of advanced technology in order to make wind energy more cost effective. Research has shown that there is a great potential for reduction in levelised cost of energy (LCOE) by developing, optimising and improving the wind turbine generators, blades and drive trains. The exploration of new areas, the great energy potential pushes the industry more offshore and more to complex conditions. To benefit from the potential, development of larger wind turbines, larger support structures and complex engineering works are required.

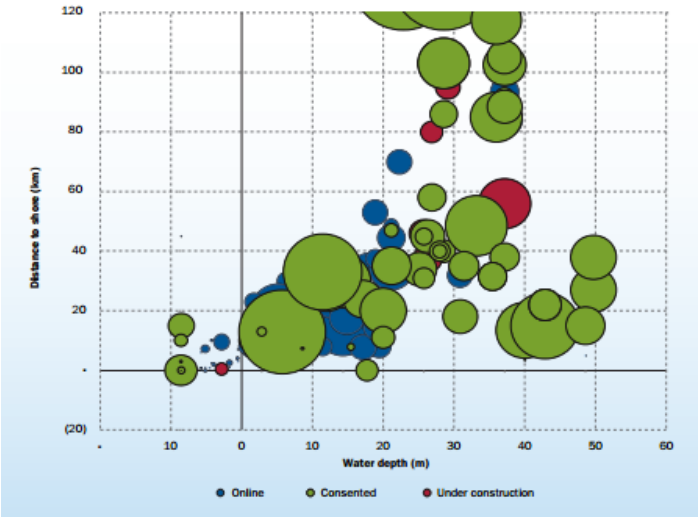

Figure 1.2: Development of wind farms with respect to shore distance, water depth and size of wind farm [18]

1.2. Offshore wind turbine foundations

Wind turbine generators can be constructed on different types of supporting structures. An overview of several types is given in Figure 1.3. In shallow waters, the most common foundation type is the monopile, which is suitable for water depths up to 30 m. It has a relatively simple design of which the pile penetration depth is adjustable to the present environmental and geotechnical conditions. These are currently the most common foundation type due to their ease of installation in shallow to medium water depths and their great supply chain capacity. Occasionally, gravity based structures are used in shallow waters. As the industry tends to go more offshore, larger wind turbine generators (6-8 MW) will be developed and installed due to the greater energy potential which is accompanied by larger water depths and thus higher loads. Larger and heavier monopiles need to be designed and constructed to cope with the loads resulting in manufacturing as well as transportation and installation difficulties.

Tripod and jacket structures are considered well-suited for sites with water depths ranges from 20-50 m. Projects are in the pipeline in water depths of 60-70 m using jacket structures. However, these still have to be consented. With increasing water depths, the hydrodynamic and wind loading increases on the supporting structure and wind turbine generator. The loads are mainly transferred in axial direction through the structural members and the large base of the structure provides a large resistance to overturning moments. In comparison with monopiles, relative low wave loading is experienced due to the large stiffness and the smaller area subjected to the waves. However, in recent projects has been observed that large monopiles are preferred as supporting structures instead of jacket structures. Initial construction costs are higher and higher maintenance costs are expected for jackets. The supply chain of large amount of jackets in a short period may also cause difficulties together with the difficult transportation of the structures.

The further from shore, the stronger winds are faced. In order to benefit from the large energy potential, new foundation types are developed called floating wind farms. Two pilot floating turbines are in operation since 2013 in deeper waters of Japan, sufficient potential was found to cover the energy demand for a couple of times. In 2016, a contract has been signed for the construction of the world's first commercial-scale floating wind farm, the Hywind project. The project is in the North Sea off the coast of Scotland and consists of five 6 MW turbines. The turbines, operating in water depths varying from 100-120 m, are moored to the seabed and are stabilised by a spar foundation. At the moment there are more than 40 projects in the development phase, each considering different designs. However, there is one obstacle named cost. Research showed the cost of energy from floating wind farms to be in the range of conventional offshore wind farms or even less, but still far more than electricity from natural gas plants. This is due to the high initial construction costs of wind farms far offshore. Still, test projects are moving forward in the hope that the technology can be improved and less costly materials can be used to cut the costs. The potential is high, if a reduction in construction costs can be realised a large amount of houses can be provided with clean energy.

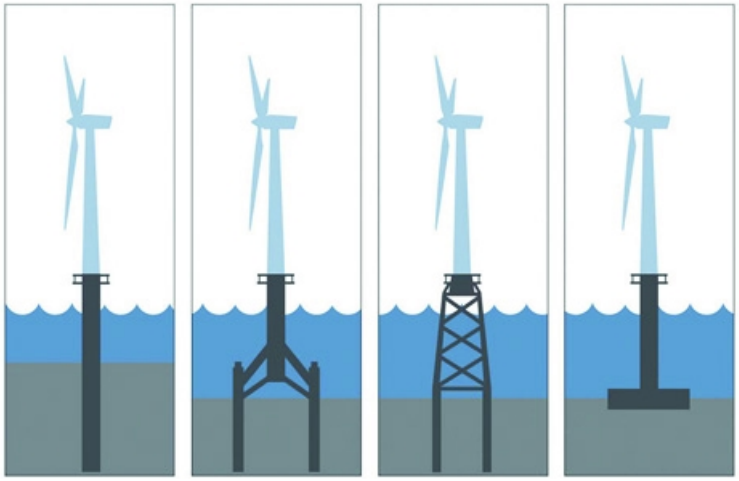

Figure 1.3: Several foundation types used in offshore wind projects. Left to right: Monopiles, Tripods, Jacket structure and Gravity based structures.

1.3. Wikinger Offshore Wind Farm

Wikinger Offshore Wind Farm is a recently finished offshore wind farm in the Baltic Sea developed by Iberdrola Renovables Deutschland GmbH and is characterised as a challenging project with difficult seabed conditions. The wind farm is constructed 34 km northeast from the German island Rügen and has a total area of 50 km^2. The wind farm consist of 70 5 MW Wind Turbine Generator (WTG) and one Offshore Substation (OSS) in water depths ranging between 36 and 42 m. Jacket structures, used to support the WTGs and OSS, in different lengths and weights are installed due to variation in water depths and soil conditions causing difficulties during the installation procedure.

Figure 1.4: Location of Wikinger wind farm

Installation procedure

The installation procedure of the foundation can be divided into two main steps, the installation of piles and the installation of the support structure. In Wikinger, the pre-piling foundation method is implemented for the foundation which basically implies that the piles are driven into the seabed prior to the installation of the support structure. An auxiliary structure, the Wikinger pre-piling template, is used for the pile installation in order to ensure the (x,y)-positions and vertical alignment of the piles. The pre-piling template is equipped with hydraulically levelling cylinders which are positioned between the mud mats and the pile guiding sleeves and functions to adjust the distance between the sleeve and mud mat, independently for all four sleeves. The levelling system is incorporated to compensate for irregularities of the seabed or settlements of the mud mats and is able to jack-up 0.80 m.

The installation is described shortly in a few steps below. After the arrival of the vessel at the installation site, the template is lifted with a template lifting tool and positioned at seabed. The internal lifting tool is attached to the crane hoist and hooked on the piles in order to upend the piles. After upending, the piles are placed one by one in the pile sleeves of the template. Next, the hydraulic hammer is lifted and placed on top of one of the piles to start the pile driving operation. The installation procedure is visualised in simple steps in Figure 1.5.

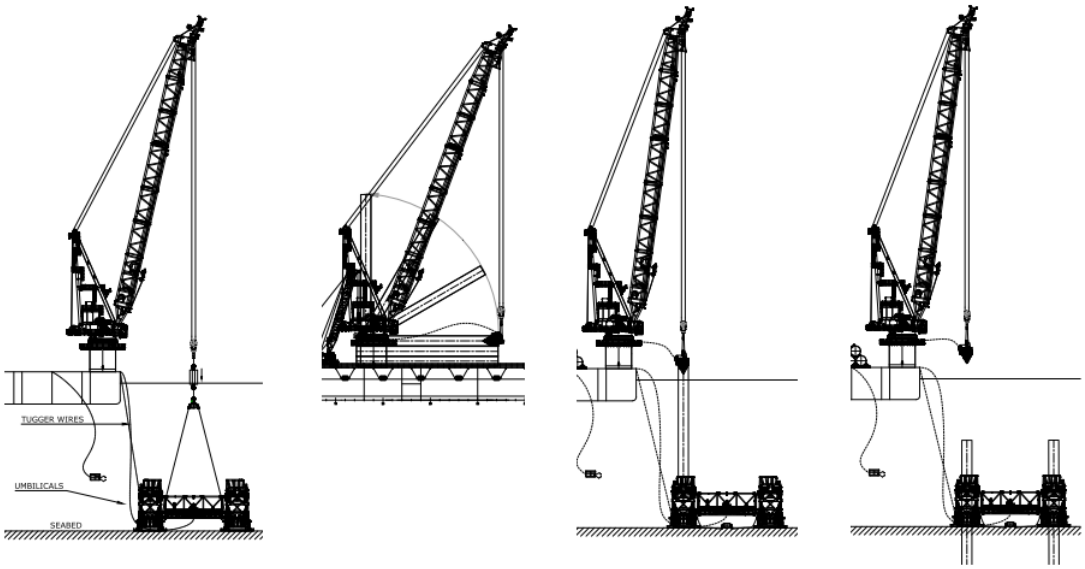

Figure 1.5: Pile installation in four steps: positioning template on seabed, upending piles, positioning pile in pile sleeves and pile driving operation.

Once the pile driving operation is finished, the template is retrieved whereupon the installation of the jacket structure can be started. The jackets are transported to the installation site by barge and are installed with a sheerleg. The jacket structure is positioned and placed on top of the pre-installed piles. Finally, a grouting operation is performed for the connection between the supporting structure and piles.

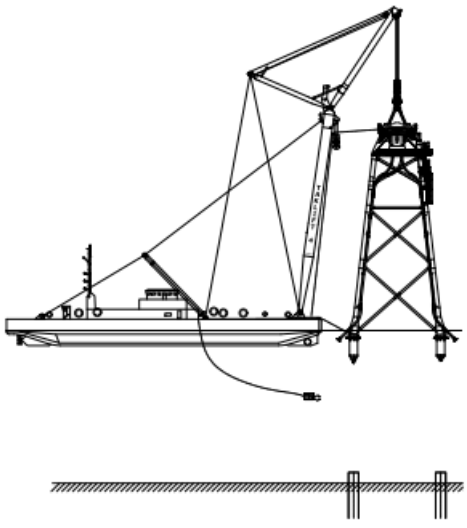

Figure 1.6: Jacket structure in the crane of the sheerleg ready for the installation on top of the pre-installed piles.

In between the positioning of the template on the seabed and the positioning of the piles into the sleeves of the template, an additional installation step is performed called preloading. The structure is preloaded in

which two towers on one diagonal are jacked-up and are lowered back to its original state followed by the same operation for the other diagonal. Performing this operation causes the self-weight of the structure to be carried by only two mud mats. Increasing the vertical load on a single mud mat with a factor of two, up to 25.6 kPa, results in squeezing of soils which causes the mud mats to settle. By the initially loading of the mud mats, additional bearing capacity is gained for the execution of the operation.

Wikinger pre-piling template
This section describes the Wikinger pre-piling template and its components, which are provided below. The template consist of four towers, one in each corner with a rigid plate connected beneath which are the mud mats. These function to transmit the load over a greater area to the soil reducing the stresses experienced and increasing the bearing capacity of the structure. In each tower, hydraulically levelling cylinders are present to compensate for the variation in settlements or irregularities in the seabed. The towers are connected to each other via large lattice beams which provide a high rigidity such that the template acts as one rigid body in which rotations of these beams hardly occur and therefore assumed to be negligible.

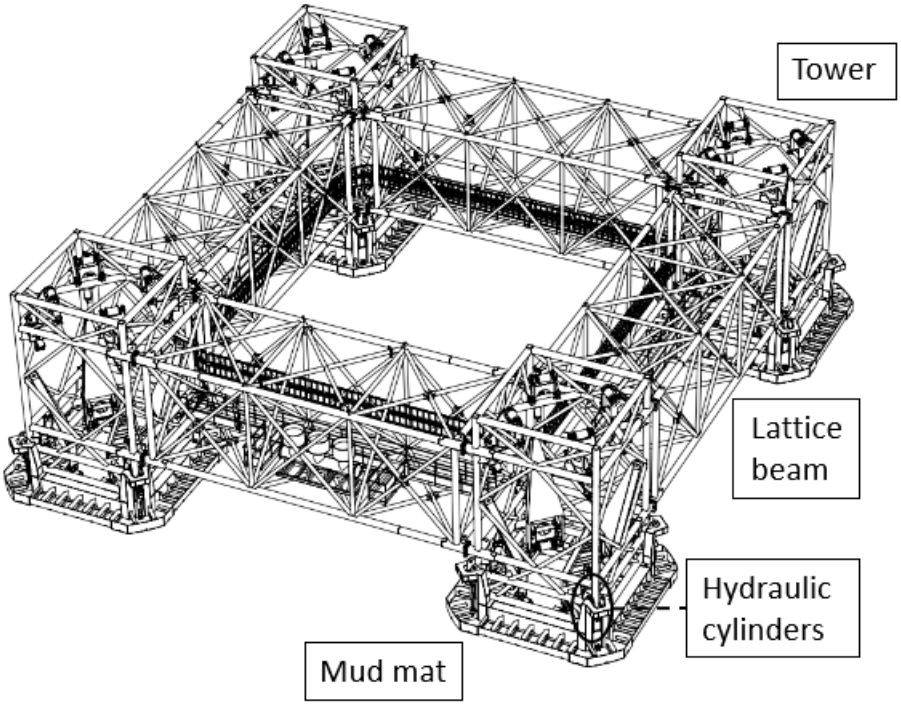

Figure 1.7: Wikinger pre-piling template and its individual components

1.4. Problem statement

A pre-piling template assists in the positioning and guidance of the piles and controls the inclination during the first meters of pile penetration. When the subsoil consist of soft soils, once in position, the template may settle due to its self-weight and/or applied preload. Application of preload is required in order to provide a safe working platform during operational conditions. A high preload incorporates a high operational safety and a lower preload results automatically in a lower operational safety.

The penetration resulting during presence of thick soft soil layers may result in operational difficulties affecting the project costs negatively. Reducing the operational window and therefore the loads and required preload is a solution to prevent operational difficulties. However, an assessment of the variables involved is required.

1.5. Thesis objective

Adjusting the operational conditions lowers the loads on the structure, which might prevent difficulties offshore such as difficult retrieval of the piling template. From this, the objective of this work is defined. The objective is formulated as:

Perform an assessment of the on-bottom stability of the Wikinger pre-piling template in soft soil strata

The operational performance of the site-specific piling template is analysed using the conditions in the Wikinger project area. The key variables are defined as the environmental loading and bearing capacity of the soil. The total hydrodynamic and wind loads are calculated, whereupon the effect of adjusting the operational conditions on the loads is investigated. Recommendations by ISO are considered to derive the bearing capacities. Finite element calculations are performed to verify and to find the conservatism in the suggestions by ISO.

The model is extended to a double footing rigidly connected system where usually a single footing is incorporated in literature. The settlements are modelled with the Press-Replace technique, originally developed for two-dimensional space but is extended and used for three-dimensional purposes. Capacity diagrams are constructed in three-dimensional loading space for footings at the seabed and at embedment. This is extended as well to a double-layered system as in reality soils are always present in multiple layers. The effect of a second stronger and stiffer layer on the capacities in the top layer is investigated. Capacity diagrams are constructed to compare both cases. As the thickness of the upper layer is another key parameter, a parametric study is performed to investigate the influence of varying the top layer thickness on the capacity.

1.6. Thesis outline

This section presents the outline of this study. This work consist roughly of three parts starting with a literature review. Secondly, a soil characterisation is performed and presented followed by the third part consisting of the results of the models.

- In Chapter 2 a literature study is presented on the different methods to determine the bearing capacity including a discussion on the parameters involved. A discussion on aspects such as adhesion and multiple footings which act together as a rigid body is provided as well.
- Chapter 3 provides the analysis of the site conditions including the site characterisation and determination of different parameters used in the analytical and numerical models.
- Chapter 4 describes the theory to determine the hydrodynamic and wind loads, presents the environmental conditions and gives the loading acting on the piles and pre-piling template and thus experienced by the soil beneath the mud mats. A dynamic analysis is performed in which the natural periods are determined to investigate the behaviour of the template in the dynamic regime.
- Chapter 5 gives an assessment of the bearing capacities of square footings positioned on a single homogeneous clay layer. Given the environmental loads, the effect of changing the operational conditions is analysed.
- Chapter 6 provides an assessment of the capacities of the mud mats on a double-layered system showing the effect of the bottom layer on the capacities in the top layer. A comparison is provided between a single and double-layered system providing the possible benefit of the second layer. Furthermore, the effect of the upper layer thickness on the capacities is investigated.
- Finally, Chapter 7 summarises the findings of this study and gives recommendations for future studies.

2

Literature review

This chapter provides a literature review on the bearing capacity of soil for different geometries. There is an elaboration made on how different cases are taken into account, such as embedment and load inclination. Different aspects such as adhesion between the soil and footing interface are discussed. Furthermore, the interaction diagrams are introduced and explained, which are used to present the bearing capacities of the footings in this study.

The footing is the part of the structure taking the load transfer from structure to soil for its account. As the load needs to be transmitted to the soil with minimal settlements nor failure, it is important to have knowledge regarding the load carrying capacity of the soil. The bearing capacity is defined as the maximum average contact pressure between the footing and the soil which may not produce plastic failure. In the past, the bearing capacity is investigated extensively for different kind of geometries. In this section, a brief review is given of the literature.

2.1. Bearing capacity

Karl Terzaghi studied the vertical bearing capacity of a plane strain footing on homogeneous soil with uniform strength over depth, which is still used extensively in geotechnical design [33]. The expression provided by Terzaghi is composed of three terms, the cohesion, the surcharge and the effective unit weight term.

$$\frac{Q}{B} = cN_c + qN_q + \frac{\gamma' B}{2} N_\gamma \tag{2.1}$$

in which N_c is the bearing capacity factor of a strip footing, c is the cohesion term, q is the surcharge acting upon the soil surface next to the footing, γ' is the effective unit weight of the soil and B is the breadth of the footing. The bearing capacity factors, N_c, N_q and N_γ, are calculated with the following formulae.

$$N_c = (N_q - 1)cot\varphi \tag{2.2}$$

$$N_q = e^{\pi tan\varphi} tan^2(45° + \frac{\varphi}{2}) \tag{2.3}$$

$$N_\gamma = 1.5(N_q - 1)tan\varphi \tag{2.4}$$

Reality shows that footings are not infinitely long and are not only subjected to vertical loading. Brinch-Hansen proposed a modification on the original equation proposed by Terzaghi [2]. Modification factors are included to take into account the influence of the shape, the embedment, inclination of the load, inclination of the footing and ground.

$$\frac{Q}{A} = \frac{1}{2}\gamma' B N_\gamma s_\gamma d_\gamma i_\gamma b_\gamma g_\gamma + cN_c s_c d_c i_c b_c g_c + qN_q s_q d_q i_q b_q g_q \tag{2.5}$$

For a infinitely long footing placed at clayey soil, with the internal friction angle equals zero and disregarding the base and ground inclination, Eq. (2.6) may be used to compute the ultimate bearing capacity.

$$\frac{Q}{A} = N_c c_u (1 + s_c^a + d_c^a - i_c^a) + q(1 + s_q^a + d_q^a - i_q^a) \tag{2.6}$$

The International Organisation for Standardization (ISO) provides a similar equation in Recommended Practice ISO 19901-4 for the bearing capacity of strip footing on clayey soils. Prandtl (1921) found the exact solution for the bearing capacity for strip footing, $N_c = 2 + \pi$ [28]. Brinch-Hansen suggests to multiply all modifications with each other, while ISO 19901-4 recommends to summarise all factors described by $K_c = 1 + s_c + d_c - i_c - b_c - g_c$.

$$Q_d = (s_u N_c K_c + q')A \tag{2.7}$$

The sliding stability of surface footings during undrained conditions depends only on the area of the footing and the strength and can be calculated with Eq. (2.8) according to ISO 19901-4.

$$H_d = \alpha s_{u0} A \tag{2.8}$$

in which s_{u0} is the undrained shear strength at base level and A is the area of the footing. ISO 19901-4 assumed a mobilisation of the full soil resistance at the interface, while at a soil-steel interface the incorporation of an adhesion factor describing the interface strength is more appropriate. Adhesion is a limiting factor describing the amount of strength can be mobilised at the interface providing knowledge regarding the roughness of the interface. Therefore, the original equation is modified with an additional variable α, which presents the adhesion.

For multi-layered soils in case of soft clay overlying a stronger soil layer, the Society of Naval Architects and Marine Engineers (SNAME) proposed an equation to compute the ultimate vertical bearing capacity of a footing. With the compression of the footing, failure with a squeezing mechanism is expected to occur which is described with Eq. (2.9). The expression holds in case the following condition is met: $B \geq 3.45 H_1 \cdot (1 + 1.1\frac{d}{B})$.

$$\frac{Q_d}{A} = \left\{\left(a + \frac{bB}{H_1} + \frac{1.2d}{B}\right) \cdot c_u + p_0'\right\} \geq \left\{N_c s_c d_c c_u + p_0'\right\} \tag{2.9}$$

in which a and b are squeezing factors, recommended as 5.00 and 0.33, respectively for B ≤ 15 m. d is the embedment, H_1 is the thickness of the soft layer, c_u is the undrained shear strength of the clay and p_0' is the surcharge on top of the clay layer. General shear failure of clay is given as the lower bound capacity.

NEN-EN 1997 provides a similar equation for the squeezing of clay. The equation is applicable when the total clay layer is affected by the load and the stronger layer beneath the clay has a minimum internal friction angle of 27.5 ° [24]. For square or circular geometries, the capacity is calculated with the following expression.

$$\frac{Q_d}{A} = \left(5.05 + \frac{B}{3 \cdot H_1}\right) \cdot c_u + \sigma'_{v;z;d} \tag{2.10}$$

where B is the breadth of the footing, H_1 is the thickness of the soft soil layer and $\sigma'_{v;z;d}$ is the surcharge term on top of the soft layer.

Shape factors

In the original and extended equations proposed by Terzaghi and Brinch-Hansen, respectively, the geometry of the structure is taken into account considering a shape factor. Several studies have been performed to determine the shape factor for different geometries. Skempton (1951) proposed a shape factor based on loading tests on undrained clay in which the factor is linearly dependent on the aspect ratio.

$$s_c^a = 0.2 \cdot \frac{B}{L} \tag{2.11}$$

Loads occur simultaneously as a combination of vertical and horizontal loading. The initial expression for the shape factor considers purely vertical loading and therefore, the expression is modified for inclined loading. Brinch-Hansen modified the original shape factor and proposed to multiply Eq. (2.11) with the inclination factor. ISO 19901-4 recommends a shape factor similar to Brinch-Hansen with a small modification.

$$s_c = 0.18 \cdot (1 - 2i_c) \cdot \frac{B'}{L'} \tag{2.12}$$

Gourvenec et al. (2006) performed a study on the undrained bearing capacity of the square and rectangular surface footings on homogeneous soils with uniform strength. Performing finite element calculations,

Gourvenec was able to validate the results for strip and circular geometries with the exact solutions, which enabled to determine best estimates of bearing capacity factors for square shaped footings. The best estimates were found as 5.56 for a smooth interface and 5.91 for a rough interface with corresponding shape factors of 1.08 and 1.15 respectively. The different values capture the different possible interfaces in which a smooth interface allows for the movement of the footing. With a rough footing, translation is prevented. To generalise the finite element results, Gourvenec proposed an equation to determine the shape factor as function of the aspect ratio for rough footings up to B/L = 1. For footings with low B/L ratio, the equation overestimates the shape factors compared to Skemptons recommendation which gets smaller with increasing B/L ratios.

$$s_c = 1 + 0.214 \cdot \frac{B}{L} - 0.067 \cdot \left(\frac{B}{L}\right)^2 \tag{2.13}$$

According to Skempton, the square geometries of the mud mats would result in an enhancement of 20 % in bearing capacity. Considering the recommendations of Gourvenec et al., the square geometry would increase the capacity with 15 % compared to a strip footing. As 5 % less capacity is obtained, this might be an indication of overestimation of the capacities for geometries with high B/L ratios proposed by Skempton.

ISO 19901-4 provides an expression to approximate the shape factor, s_q as well. In case of Tresca soil, i.e. $\varphi = 0°$ and $c = s_u$, s_q will equal 1. Terms including the effective weight of soil, γ', are disregarded as it only plays a role in case of drained material.

$$s_q = 1 - sin\varphi \cdot \frac{B}{L} \tag{2.14}$$

Depth factors

As soon as a footing starts to settle or is placed at a certain embedment, depth effects start playing a role in the bearing capacity of the soil. Soil next to the base has a certain weight, which needs to be taken into account by the surcharge term. Once soil is loaded to failure, rupture lines start developing. Since soil is present next to and above the footing base, the lines of the failure mechanisms will extend into the soil above the base resulting in improvement of the bearing capacity. This mechanism is taken into account through a depth factor.

Currently, the following equation is widely adopted in design to describe the depth factor. Several studies are performed to determine the factor n.

$$d_{cV} = 1 + n\frac{d}{B} \tag{2.15}$$

in which $0.2 \leq n \leq 0.4$.

Skempton (1951) proposed an approximating closed-form expression for depth factors of strip, square and circular geometries which holds for d/B ratios up to 2.5. For d/B ratios larger than 2.5, the depth factor equals 1.5 [30].

$$d_{cV} = 1 + 0.2 \cdot \frac{d}{B} \tag{2.16}$$

Brinch-Hansen proposed empirically determined depth factors for both the cohesion and surcharge term and distinguished two situations in which d is smaller than or equal to B and d is larger than B, which are widely accepted. An expression for the depth factor of the cohesion term is proposed as well, which is assumed to be 1 as Tresca soil is considered within this study.

$$d_c^a = \begin{cases} 0.4 \cdot \frac{d}{B} & d \leq B \\ 0.4 \cdot arctan\frac{d}{B} & d > B \end{cases}$$

in which d is the embedment of the footing.

ISO 19901-4 suggests a similar depth factor which is based on Det Norske Veritas (DNV) and is slightly more conservative compared to Brinch-Hansen.

$$d_c^a = 0.3 \cdot arctan\frac{d}{B} \tag{2.17}$$

Bransby & Randolph (1999) performed an investigation on the effect of the embedment depth on the undrained response of skirted strip foundations to combined loading. The embedment is modelled by placing the foundation at a depth equal to the skirt length. The relation between d_{cV} and d/D is non-linear and depends on the heterogeneity of the soil. For a foundation on homogeneous soil, Bransby & Randolph proposed a linear relation fitting their results obtained with plasticity analysis reasonably well. The results of the study showed that the n-factor, varying mainly between 0.2 and 0.4, is under-predicting the depth effect for strip footings on uniform soil. The difference may result due to a difference in geometry or overestimation of embedment effects by the plasticity analysis [1].

$$d_{cV} = 1 + \frac{d}{D} \tag{2.18}$$

Gourvenec (2008) performed a study on the effect of embedment on the bearing capacity of shallow foundations during undrained loading. Using finite element analysis, Gourvenec proposed a relation of the depth factor as a function of the embedment ratio holding for $0 \leq d/B \leq 1$ [14]. This equation is useful when the embedment of the footings are known. Settlements during installation or due to preloading cannot be captured with this expression.

$$d_{cV} = 1 + 0.86 \cdot \frac{d}{B} - 0.16 \cdot \left(\frac{d}{B}\right)^2 \tag{2.19}$$

The depth factors obtained by Gourvenec are compared to the widely used bearing capacity factors for embedded smooth and rough footings. By multiplying the bearing capacity of a surface foundation with the depth factor, the bearing capacity for an embedded footing is obtained.

The finite element results for smooth footings are well bracketed by the conventional factors provided by Brinch-Hansen, Skempton and Meyerhof as shown in Figure 2.1. For rough footings, the results are compared with the findings of Bransby & Randolph (1999) and Edwards et al. (2005). Bransby & Randolph provided an upper bound solution derived with plasticity analysis for an embedded strip footing. Edwards et al. studied the bearing capacity factors of shallow embedded strip and circular geometries. However, a direct comparison is not appropriate since only base shear is taken into account. Sidewall friction is neglected and therefore this solution is considered conservative [5].

Depth factors for the γ-term are not discussed as sandy soils are not of interest.

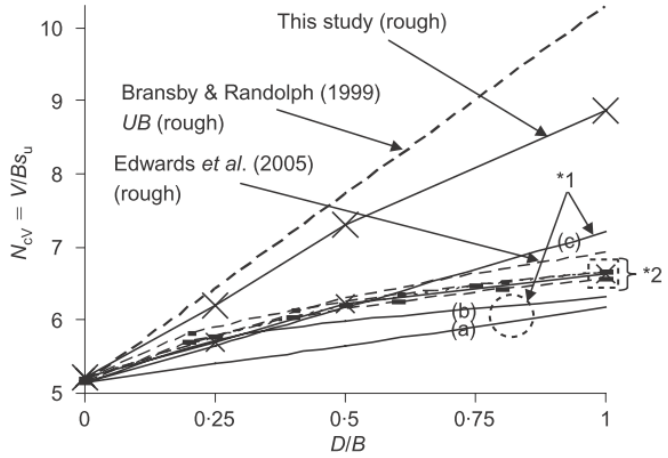

Figure 2.1: Comparison of bearing capacity factors for smooth embedded strip footings of different studies. Conventional factors *1 (a) Brinch-Hansen (1970) (b) Skempton (1951) (c) Meyerhof (1963). Numerical factors *2: This study, Salgado et al. (2004) & Edwards et al. (2005)

Besides the increase in vertical capacity, there is an increase in horizontal bearing capacity as well. Brinch-Hansen (1970) suggests to exclude depth factors for the horizontal capacity but take the passive soil pressure on the side of the footing attached to the soil into account. Bransby & Randolph performed also a study on

the effect of embedment on the pure horizontal bearing capacity by means of an upper bound plasticity calculation. For fully attached sidewalls, a double-sided wedge failure mechanism occurs while if one sidewall detaches, a one-sided wedge mechanism will develop. Based on the analyses, an approximating equation as a function of soil strength heterogeneity, soil-footing interface and soil bonding is proposed.

$$\frac{H_d}{Ds_{u0}} = 1 + a\Big(\frac{d}{D}\Big)\Big(1 - \frac{kd}{2s_{u0}}\Big)\Big[\alpha tan\delta + \frac{1}{cos\delta sin\delta}\Big] - (a-2)\Big(\frac{\gamma d}{2s_{u0}}\Big)\Big(\frac{d}{D}\Big) \tag{2.20}$$

in which a describes the attachment of the sidewalls. α is the ratio of shear stress over undrained shear strength which basically provides information regarding the interface strength between the soil and structure and δ is the angle of the wedge. In case that $\alpha = 1$, $\delta = 0.615$ providing the minimum horizontal bearing capacity, which is valid for all combinations of d/D and kD/s_{u0}. The increasing in horizontal capacity can also be expressed in terms of embedment ratio and soil strength heterogeneity. The equation holds for an embedment ratio up to unity. Interesting is the decrease of the ultimate horizontal bearing capacity with increasing soil strength heterogeneity, kD/s_{u0}. As the heterogeneity becomes larger, the soil above the footing base weakens with respect to s_{u0} resulting in a smaller ultimate horizontal bearing capacity.

$$d_h = 1 + 5.66\Big(\frac{d}{D}\Big) - 2.83\Big(\frac{d}{D}\Big)^2\frac{kD}{s_{u0}} \tag{2.21}$$

Gourvenec (2008) performed a study on the increase in horizontal capacity and proposed a quadratic function for the depth factor of pure horizontal capacity.

$$d_{cH_{ult}} = 1 + 4.46\frac{d}{B} - 1.52\Big(\frac{d}{B}\Big)^2 \tag{2.22}$$

Latter equations describe the increase in pure horizontal capacity due to passive soil pressure acting on the active side of the footing. However, there is no height variable of the footing included in the proposed equations and therefore it is rather questionable whether and when this additional capacity can be taken into account. The equations assume the sidewalls to be in fully contact with the soil which is not appropriate and therefore d needs to be chosen carefully.

The enhancement in horizontal capacity can also be determined with the passive earth pressure mobilised due to the horizontal loading as suggested by Brinch-Hansen. By integrating the pressure over the area of the sidewall, the passive horizontal force can be determined which can be considered as additional capacity.

$$H_p = \frac{1}{2}K_p\gamma' h^2 B + 2ch\sqrt{K_p}B \tag{2.23}$$

in which K_p is the passive earth pressure coefficient, h and B are the height and breadth of the footing and c is the cohesion, which is equal to the undrained shear strength. h needs to be chosen carefully, which equals the settlement depth assuming that the wall is fully in contact with the soil for partly embedded footings. The passive earth pressure coefficient is a function of internal friction angle and can be calculated with the following equation.

$$K_p = \frac{1 + sin\varphi}{1 - sin\varphi} \tag{2.24}$$

Inclination factors

Footings are subjected to combined horizontal and vertical loading triggering a combination of sliding and bearing failure mechanism affecting the bearing capacity. This inclined loading on the structure is taken into account by means of an inclination factor. Brinch-Hansen proposed inclination factors for the cohesion and surcharge term. In case of soil in undrained conditions, the inclination factor for the cohesion can be calculated with Eq. (2.25), which is adopted in adopted in ISO 19901-4 as well.

$$i_c = 0.5 - 0.5\sqrt{1 - \frac{H}{As_u}} \tag{2.25}$$

SNAME suggests in the Guidelines for Site Specific Assessment of Mobile Jack-Up Units also inclination factors for the cohesion term for soils in undrained conditions.

$$i_c = 1 - \frac{mF_H}{Ac_u N_c} \tag{2.26}$$

Brinch-Hansen and ISO suggest that inclination factors for the surcharge and effective unit weight term only starts playing a role during drained conditions. However, SNAME recommends to take the factor for the surcharge term, in case of clay, into account as well [31].

$$i_q = \left(1 - \frac{F_H}{F_{VH}}\right)^m \tag{2.27}$$

in which F_H is the horizontal capacity and F_{VH} is the vertical foundation capacity in combination with horizontal load. m is a factor taking into account the direction of inclination.

$$m = \begin{cases} \frac{2+B/L}{1+B/L} & \text{Strip footing: for inclination towards shorter side} \\ \frac{2+L/B}{1+L/B} & \text{Strip footing: for inclination towards longer side} \\ 1.5 & \text{Circular footing} \end{cases}$$

2.2. Adhesion

For many problems in geotechnical engineering it is important to have knowledge about the shearing resistance to sliding at the interface between soils and other materials. Different studies have been performed on the shearing behaviour between soils and structural materials, mainly for sand and in less extend for clay.

Potyondy (1961) did an investigation on the skin friction between various soils and construction materials. For two different types of clay, the skin friction was determined. However, the techniques used to determine these values is not explained well and it is also not clear what kind of strength parameters are presented [27].

Tomlinson (1969) published data for loading tests on driven piles and analysed his results in terms of an adhesion factor, which is defined as the mobilised shear strength in skin friction divided by the undisturbed shear strength. Tomlinson showed a decrease in adhesion factor as the shear strength of stiff clay increased, while in soft clay the bearing capacity of the piles increased with time. This is explained with the fact that soft clay sticks to the pile during pile driving and re-consolidates around the pile [34].

Another study was performed by Littleton (1976), who investigated the shearing behaviour aiming to present a complete set of strength parameters for the shearing resistance at the soil-steel interface. Tests are performed in shear in quick undrained, consolidated undrained and consolidated drained conditions with test material which had a plasticity index of 30 and 50. With the clay-steel experiments on over-consolidated clayey material, Littleton suggested to incorporate an adhesion factor of 0.75 for fast loading cases. For longer term loading, the adhesion factor drops to 0.6 [22]. Adhesion should be taken into account, especially in case of surface footings. It is less influential when the footing is embedded or equipped with skirts.

2.3. Multiple footings acting in consort

The pre-piling template consist of four towers connected with lattice beams forming a shallow foundation with multiple footings. Usually the bearing capacity of such a foundation is simply determined by superposing the bearing capacities of the individual footings as if they act independently from each other. Additional bearing capacity can be obtained by considering the kinematic constraint provided by the structural connection between the footings. However, still little research is performed on this topic.

Fisher & Cathie (2003) presented design considerations for a system with multiple footings. The considerations were especially based for a sub sea intervention valve protection unit which consisted of a rigidly connected two-footing system. The main conclusion was to consider the system as a one-being instead of individual footings as this may result in structural over design [10].

Gourvenec & Steinepreis (2007) performed an analysis on the additional capacity resulting from kinematic constraints for a skirted foundation comprised of multiple footings. By varying the distance between

footings, the effect of spacing is investigated for the different ultimate limit states. The obtained bearing capacity for a two-footing system in pure vertical direction is normalised with the bearing capacity of a single footing, as a function of the normalised spacing with footing breadth, is shown in Figure 2.2.

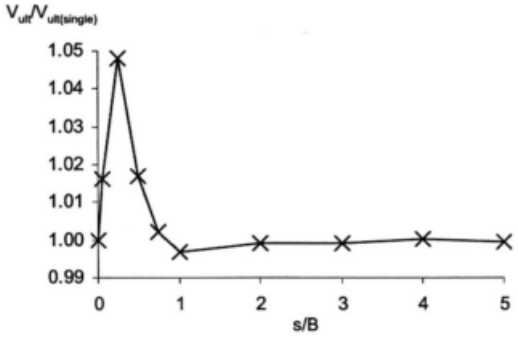

Figure 2.2: Increasing in vertical bearing capacity by considering foundation with multiple footings as one system [15]

Additional bearing capacity in vertical direction is only achieved for spacing less than s/B with a maximum of 5 % at a spacing of $0.25B$ [15]. Footings placed at larger distances than one times the breadth are found to act independently of each other and therefore no additional bearing capacity is obtained. The increase with close footings is due to the fact that the failure mechanisms are not able to develop fully. Basically, the side wedges in the failure mechanisms of the footings prevent each other to develop, which results in the enhancement of the vertical bearing capacity.

An increase in horizontal capacity is not obtained as the capacity is purely depending on the base area. The results of the study showed an increase in moment capacity. Spacing from 1B up to 8B are investigated. Different expressions are proposed to approximate the moment ultimate limit state for spacing up to 3B and for spacing between 6B and 8B. For intermediate spacing, i.e. 3B - 5B, no simple analytical expression is found as the observed failure mechanism was in a transition from a rotational to an independent push-pull mechanism.

The effect of spacing in multiple footings acting together for combined loading is also investigated. Two-footing systems with spacing of one, two and three times the breadth are considered for the combined loading cases. In the combined vertical and horizontal loading case, the footings seem to act independently and therefore no additional capacity is obtained for all three cases. A slight increase is expected when the footings are placed closer than one times the breadth to each other as an increase in pure vertical capacity was observed. However, the impact of this slight increase is rather questionable.

For the increase in capacity with V-M (eccentric), H-M and general V-H-M loading and corresponding failure mechanisms, please refer to Gourvenec & Steinepreis (2007).

2.4. Interaction diagrams

Footings are subjected to various combinations of loading such as self-weight, operational, environmental and installation loads. Traditionally, the solution for an infinite long strip resting on homogeneous soil is used and modified to account for the footing shape, inclination of the load and embedment of the footing as described earlier. Currently, a new procedure called the failure envelope diagram is getting more accepted for the prediction of the ultimate limit states of a shallow foundation during combined loading. The failure envelope is basically a locus through all points of horizontal and vertical load combinations which result in failure. When the loading falls inside the locus, elastic deformation will occur while when the locus is touched or exceeded, plastic deformation of the soil will occur. With the procedure of the envelopes, it is assumed that the soil properties are uniform over the area and the loading is uniformly distributed over the loaded area.

This approach allows for the explicit consideration of the independent load components. Optimisation of the design output as a function of a certain input variable is also possible by implementing this procedure into a spreadsheet or scripting tool.

The procedure to construct the interaction diagrams is as follows. First, the 'uni-axial' ultimate limit states have to be defined. The vertical ultimate limit state is the capacity of the soil under pure vertical loading, with $H = 0$ & $M = 0$. The horizontal ultimate limit state is the capacity in pure horizontal direction, thus when the vertical and moment loading equals zero. The second step is to define the shape of the interaction diagram through closed form expressions which are a function of vertical, horizontal and/or moment loading normalised with its ultimate limit state.

The magnitude of the uni-axial capacities and the shape of the interaction diagrams depend on the loading conditions, undrained or drained, the soil strength profile, the shape and embedment of the foundation. A kinematic constraint between adjacent footings may change the uni-axial capacities and inclusion of tension at the soil-footing interface may affect the shape of an interaction diagram.

The sign convention for the general loads to construct the interaction diagrams obeys the convention proposed by Butterfield et al. (1997). A positive vertical load acts downwards and a positive horizontal force acts towards the right. Moment loading or rotations in clockwise direction are considered as positive, while anti-clockwise implies a negative moment and rotation. The reference point is considered at the bottom of the rigid body as shown in Figure 2.3.

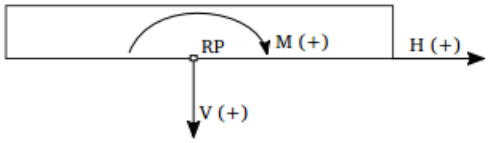

Figure 2.3: Sign convention for V-H-M loading [3]

Equations describing the shape of the interaction diagrams have been proposed for various geometries mainly considering full bonded interface between soil and footing, which accounts for the ability to transmit unlimited tension. This ability results from the generation of negative excess pore pressures between the bottom of the footing base and soil during uplift or overturning moment and is often achieved with skirted foundations, which are mainly employed offshore. Although the generation of the suction is rather doubtful as for example a small gap between skirt-soil interface may result in loss of suction, there is little literature available regarding shallow foundations subjected to combined loading with an interface unable to sustain tension. The main difference in interaction diagrams allowing unlimited tension and zero-tension interfaces is the obliqueness in the diagrams for foundations with base suction at lower vertical loads. If suction is taken into account, the footing can cope with significant larger moment loading when moment and horizontal loading acts in the same, positive direction. This is often the case since the moment loading results from the horizontal wave and wind loading acting on the superstructure.

Taiebat & Carter (2000) explained the obliqueness in the interaction diagrams by studying the plastic zones and soil movement for different combinations of loading. For footings subjected to lateral and moment loading, there is a point around which the foundation and soil tend to rotate. The position of this point depends on the ratio of moment and horizontal loading. In case that lateral and moment loading acts in the same direction, this point remains below the foundation. Reducing the lateral load and increasing the moment load brings this point above the foundation resulting in a smaller plastic zone corresponding to a reduction in the moment capacity [32]. This rotation point, determined by the ratio of applied horizontal and moment loading, determines the extent of the plastic zone and therefore the capacities. The obliqueness in the H-M interaction diagram develops therefore from the different failure mechanisms resulting from the applied moment over horizontal load ratios.

Failure envelopes are presented considering H-V, H-M, V-M or V-H-M loading. In the following sections, an elaborated follows on the V-H and V-H-M failure envelopes.

V-H loading plane

Bearing capacities may be expressed in terms of horizontal and vertical load combinations. Different studies are performed of which a small overview is given below. With numerical studies, the shape of the failure envelopes is studied. By taking advantage of the elliptical nature of the envelope is found that the envelopes

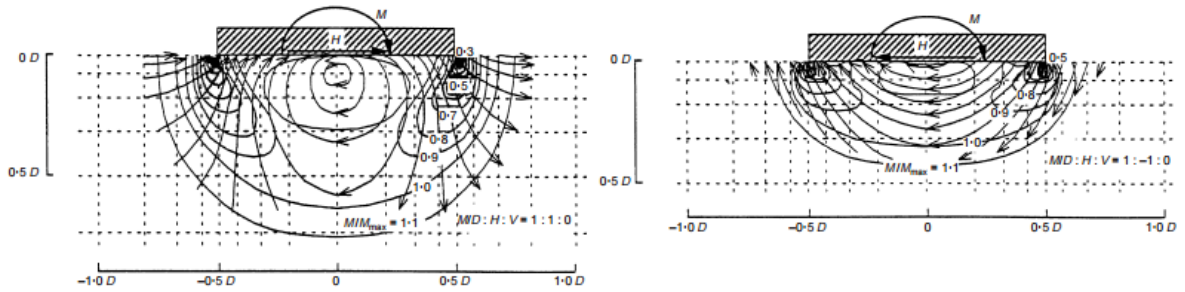

Figure 2.4: Expansion of plastic zone and direction of soil movement for lateral and moment loading acting in same and opposite direction [32]

have a general, symmetrical, form described by the following equation.

$$\left(\frac{H}{H_{ult}}\right)^a + \left(\frac{V}{V_{ult}}\right)^b = 1 \tag{2.28}$$

in which a and b are fitting coefficients.

Green (1954) performed a study on the bearing capacity of an infinitely long strip, able to sustain unlimited tension, resting on homogeneous soil and subjected to inclined (V-H) loading [17]. In his study, Green found an exact solution on the problem and presented it as follows.

$$\frac{V}{As_u} = \left(1 + \frac{\pi}{2}\right) + cos^{-1}\left(\frac{H}{As_u}\right) + \sqrt{1 - \left(\frac{H}{As_u}\right)^2} \tag{2.29}$$

where $H/As_u = 1$ for $V/As_u \leq 0.5$.

For the capacities in V-H loading plane, ISO 19901-4 refers amongst others to Gourvenec (2007). Gourvenec investigated whether the exact solution presented by Green was applicable to footings with different B/L ratios. For footings with B/L ratio up to unity, corresponding to a square, Gourvenec found the failure envelopes to fall in a very tight band with Greens normalised exact solution [12]. Gourvenec also proposed an alternative fit to the failure envelope in v-h plane for surface footings with B/L ratios up to unity on homogeneous soil given by Eq. 2.31.

$$v = 0.5 + \frac{cos^{-1} h + \sqrt{1 - h^2}}{2 + \pi} \tag{2.30}$$

$$v = 0.5 + 0.5\sqrt{1 - h} \tag{2.31}$$

where $h = 1$ for $v \leq 0.5$ for Eqs. (2.30) & (2.31). h and v are the normalised loads, H/H_{ult} and V/V_{ult}, respectively.

In order to take the depth effects into account, the embedment of the footing is considered. Studies have been performed on investigating the depth effects for various footings equipped with skirts as these are appropriate for the offshore scenario. The algebraic fits to Greens solution cannot be used for the construction of the interaction diagrams of the embedded footings as the failure envelopes are dependent on the embedment ratio and those fits does not take this aspect into account, which would result in unconservative loci [14]. The shape of the normalised v-h envelopes for shallow strip footings can be approximated by the following power law which holds for d/B ratio up to 0.5.

$$v = (1 - h)^p \tag{2.32}$$

In which p varies from 0.18 to 0.25 for $0 \leq d/B \leq 0.5$.

In general, footings equipped with skirts are considered for research. Since not all are equipped with skirts, footings with zero-tension interfaces are considered as well. Shen et al. (2016) found that the normalised Greens solution is suitable to describe the failure envelope of footings not able to sustain tension.

However, there are limitations on the applicability. It can only be used for strip and circular foundations positioned at seabed on uniform soils. For soils with increasing degree of soil strength heterogeneity, the envelope starts to diverge and will therefore provide inappropriate results [29].

Besides investigating the applicability of Greens solution on other geometries, Gourvenec (2007) performed also an analysis on whether the exact solution is useful in case of surface footings unable to sustain tension. Eq. (2.31) proposed by Gourvenec for strip, rectangular and square footings showed a good agreement, only for high vertical loads the capacity was slightly overestimated.

Feng et al. (2014) worked on a design approach for rectangular mud mats under fully three-dimensional loading. Expressions are provided that help approximating the ultimate capacities in six degrees of freedom. Using these, Feng et al. provided shapes of failure envelopes for different biaxial loading and combined three-dimensional loading in two-dimensional plane by assuming one component to be quasi-constant. This work is performed for rectangular footings but the results are accurate enough to be interpolated for $0.33 \leq B/L \leq 1.0$ and embedment ratios of $0 \leq d/B \leq 0.2$. Both uniform soil strength and linearly increasing soil strengths, $0 \leq kB/s_{u0} \leq 10$, have been considered in the study. The mud mats are modelled rigidly and are fully bonded to the soil with a rough interface. The side walls are assigned zero-tension interfaces. The method provided is applicable for a wider range of conditions. However, revision of the fitting coefficients and/or expressions for conditions other than described in the paper might be necessary.

According to Feng et al., the capacities in the V-H loading plane for horizontal loading in the x-direction ($\theta = 0°$) and y-direction ($\theta = 90°$) can be approximated with Eq. (2.33) [9].

$$v = 0.5 + 0.5(1 - h^{2.5-cos^2\theta})^{0.5} \tag{2.33}$$

for $h < 1$. When $v \leq 0.5$, h equals 1. Comparing this expression with the results of the finite element calculations showed that some points fall inside the envelope, especially with increasing d/B ratio. Therefore, a compensated fit is proposed in which the coefficients are slightly adjusted,

$$v = 0.4 + 0.6(1 - h^{2.5-cos^2\theta})^{0.5} \tag{2.34}$$

for $h < 1$. When $v \leq 0.4$, h equals 1.

As the shapes of the failure envelopes are normalised with the ultimate capacities in vertical and horizontal direction, Feng et al. presented expressions to determine these as well. These expressions are given for a rectangular footing which is verified for the conditions given above.

$$\frac{V_{ult}}{As_{u0}} = 5.7\left[1 + 0.234 tanh\left(4.78\frac{d}{B}\right)\right] \cdot (1 + 0.2\kappa - 0.012\kappa^2 + 0.0004\kappa^3) \tag{2.35}$$

$$\frac{H_{yult}}{As_{u0}} = 1 + \frac{d}{B}\left(N_p\frac{B}{L} + 2\alpha_{skirt}\right)\left(1 - \frac{\kappa d}{2B}\right) \tag{2.36}$$

in which N_p is the skirt bearing factor used to take into account the additional net contribution from active and passive soil pressures on the mud mat skirts for embedded footings. This factor is defined as $N_p = 2.2 + \gamma' d/2s_{u,avg} \leq 4.4$ for smooth skirts and $N_p = 4.4$ for fully rough skirts. α_{skirt} describes the friction ratio of the skirts.

V-H-M loading space

Reality shows that offshore structures are subjected combined vertical, horizontal and moment loads rather than only vertical and horizontal loads. Currently, the representation of the ultimate limit states under general VHM loading in terms of failure envelopes becomes increasingly popular. Incorporation of these envelopes allow to see directly the effect of a single component on the global stability of the structure.

Usually VHM failure envelopes are presented in three-dimensional graphs, which are complex shaped graphs and hard to construct. Since the vertical loads may assumed to be quasi-constant allows to represent the three-dimensional failure envelopes in two-dimensional H-M diagrams for constant vertical load [13].

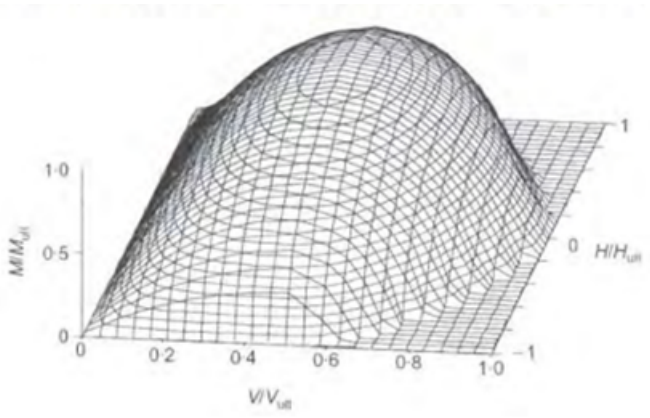

Figure 2.5: Three-dimensional failure envelope for a surface footing with a zero-tension interface

Bransby & Randolph (1999) did an analysis on the VHM failure envelopes for embedded strip footings. An expression is found which initially was derived for embedded strip footing on heterogeneous soil but is applicable to other soil strata as well by scaling the loci with H_{ult}, V_{ult} and M_{ult}. Although not theoretically justified, the differences between derived and fitted loci were minimal [1]. Taiebat & Carter (2000) studied the bearing capacity capacity of shallow circular footings able to transmit tension at the interface on homogeneous soil and proposed an equation to predict the capacities in three-dimensional space. An accurate three-dimensional equation for the envelopes, capturing the inclination and eccentricity of the loading, is likely to be a complex algebraic expression. Simplifications are therefore inevitable resulting in a slight deviation during fitting. The equation proposed by Taiebat & Carter provides an overall satisfying fit. However, there will be a slight mismatch over the whole range, especially around abrupt changes in the shape of the locus occurring with high horizontal loads.

$$\left(\frac{V}{V_{ult}}\right)^2 + \left[\frac{M}{M_{ult}}\left(1-\alpha_1\frac{HM}{H_{ult}|M|}\right)\right]^2 + \left|\left(\frac{H}{H_{ult}}\right)^3\right| - 1 = 0 \tag{2.37}$$

in which α_1 depends on the soil profile. For homogeneous soils, $\alpha_1 = 0.3$ is found to provide a good fit to numerical results.

Conventional bearing capacity theory showed to provide good representations of failure envelopes in vh and vm loading space for footings unable to sustain tension. In case of coupling of inclined and eccentric loading, conventional theory gives conservative predictions of the capacities. Therefore, Gourvenec (2007) suggested a closed-form solution in normalised space as a function of v, h and m for strip, rectangular and square footings unable to sustain tension.

$$\left(\frac{h}{h^*}\right)^2 + \left(\frac{m}{m^*}\right)^2 = 1 \tag{2.38}$$

in which h^* and m^* are

$$h^* = \frac{0.25 - (v-0.5)^2}{0.25}$$

$$m^* = 4(v - v^2)$$

Shen et al. (2016) did an investigation on the shape of the failure envelopes. Shen et al. found that a better fit was obtained by adjusting the ellipse form of the equation found by Gourvenec (2007).

$$\left(\frac{h}{h^*}\right)^2 + \left(\frac{m}{m^*}\right)^q = 1 \tag{2.39}$$

For strip and circular footings, q = 1.5 gives a better fit [29]. Dealing with a strip footing and high vertical load mobilisation, $v > 0.5$, $q = 1.0$ provides a conservative fit. Note that latter equation does not capture the asymmetry in case of increasing soil strength heterogeneity. It is hard to capture this phenomena as only the

shape only varies with - H + M and + H - M. The following equation may be used to fit asymmetrical data output.

$$\frac{M}{M_{ult}} = c\left(1 - \frac{H}{H_{ult}}\right)^a \left(1 + \frac{H}{H_{ult}}\right)^b \tag{2.40}$$

The latter equation produces zero moment capacity when the horizontal load equals the ultimate horizontal capacity, both positive and negative. The parameter c is used to set the value of M/M_{ult} when H needs to be zero. The coefficients a and b are the fitting parameters to modify the shape of the curve to match the data output.

2.5. Summary and discussion

Chapter 2 provided a brief review on the bearing capacity of shallow foundations. Prandtl (1921) derived the exact bearing capacity factor for a strip footing on homogeneous soil, whereupon Terzaghi and Brinch-Hansen continued investigating the capacities of shallow foundations. Recommendations of guidelines such as the ISO and SNAME are presented as well incorporating expressions provided by the latter researchers. The modification factors for geometry, depth and load inclination are discussed. The factors recommended by ISO 19901-4 are semi-empirical and vary therefore from values obtained with numerical studies. For a square footing, the semi-empirical factor overestimates the vertical bearing capacity with 5 % and is also disregarding friction on the sidewalls.

Adhesion is describing the shearing resistance to sliding on the base of the footing which is of importance at the seabed. Several studies are performed but in less extent for clay. Therefore, a value of 0.75 is adopted [22]. Additional vertical and horizontal capacity due to kinematic constraints provided by the beams between the footings is not expected as distance between footings is larger than one times the breadth and the horizontal capacity is only dependent on the strength near the seabed. However, increase in moment capacity might occur [15].

An introduction is given regarding a new procedure to present the ultimate limit states of a shallow foundation during combined loading. Failure envelopes describe a locus consisting of all load combinations resulting in plastic deformation. The approach to construct the diagrams is explained followed by expressions provided in literature to derive the locus in V-H loading space for different geometries fully bonded to the soil, at surface and embedded for homogeneous and heterogeneous soil strengths. Studies showed that the expression by Gourvenec (2007) is capable of approximating the capacities of strip, circular and square footings with a zero-tension interface as well. An expression is provided which can be used to derive the envelopes making use of the symmetrical character of an ellipse.

As combined loading is three-dimensional, the capacities can be expressed in H-M loading space for quasi-constant vertical loading. Providing algebraic expressions capturing the inclination and eccentricity of the V-H-M interaction diagrams is difficult. Therefore, an expression is proposed which is able to capture the capacities in both -H+M and +H+M loading space with the ability to produce the maximum moment not at H = 0. However, the fit is limited with producing the inclination of the envelope when the maximum horizontal capacity becomes larger than the ultimate horizontal capacity.

3

Soil characterisation

An offshore site campaign is carried out to obtain more knowledge regarding the composition and strength of the soil depositions in the project area. The investigation is used to study the soft soil depositions, which may cause difficulties during the piling and installation operations. Raw data from the campaign is analysed to identify the locations and provide a characterisation of the soft soil strata.

According to the geological report and data from the main geotechnical campaign, the soil is found to consist of different materials. The deepest explored layer consists of slightly consolidated white Chalk with a layer of Glacial till depositions on top. Till is a mixture of stiff over-consolidated clay, which is silty, sandy and gravelly and is characterised with undrained characteristics. Intermediate, a channel of Fluvioglacial till is found extending from the south eastern project border to the south western project border. On top of the Glacial till, Holocene deposits are formed often characterised as young soft marine sediments and very soft clay.

A set of advanced static, oedometer, triaxial and direct shear tests and cyclic tests are conducted to establish strength, deformation and consolidation characteristics of the depositions. These have been derived for Glacial till, Fluvioglacial till and Chalk depositions. No tests are performed on Holocene deposits as these were expected to scour away. Hence, Cone Penetration Tests (CPT) and boreholes at every of the 70 locations are used to establish the soil characterisation of the soft strata.

The boreholes provide information regarding the different densities (bulk, specific and dry), water content and Atterberg limits at different depths. Classification parameters are derived, considered to identify the Holocene deposits. To characterise the undrained shear strength of the soil, penetrometer, torvane and Undrained Unconsolidated (UU) triaxial tests are used along with the boreholes.

The undrained shear strength over depth is derived using the CPTs and is verified with the results from the other tests. Taking into account the possible presence of soft strata based on the classification parameters and strengths, the critical locations are determined within the project area. In the following section, the output of the soil characterisation is provided. Characteristics as densities, water content and Atterberg limits are presented followed by the derivation of the undrained shear strength.

3.1. Bulk density

The bulk densities of all locations are considered as deficiencies are present in the results of the boreholes. Tests are performed irregularly over locations and depths. However, useful information is obtained regarding the densities. Locations and depths at which high densities were found, i.e. $\rho > 1900 kg/m^3$, are disregarded as it is believed that these does not represent soft clay. Parameters obtained at equal and/or larger depths, for which high densities were found, are disregarded as well since tests used to obtain those classification parameters are considered to be reliable. This resulted in the following bulk densities over depths throughout the project area.

Figure 3.1 shows the deviation in bulk density over depth within the project area. A constant bulk density of 1600 kg/m^3 is considered to be representative for the Holocene deposits since the density varies mainly

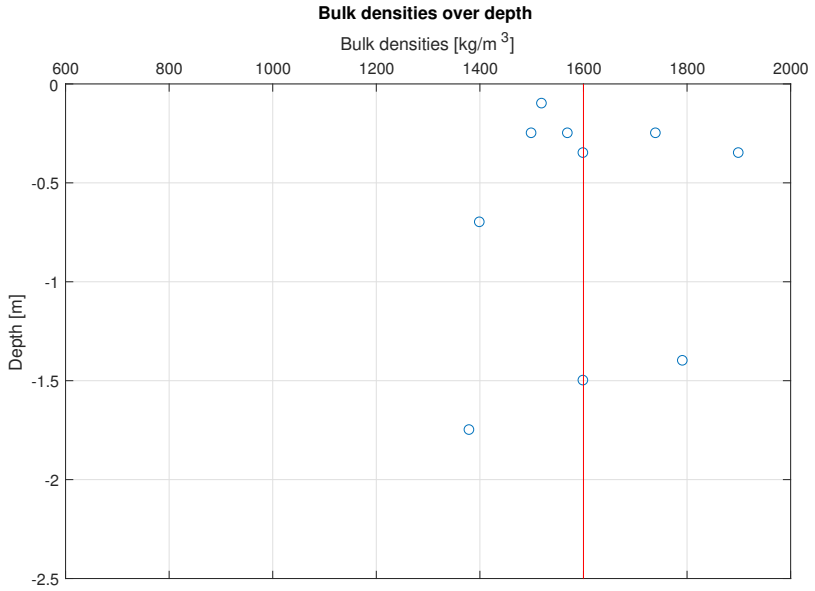

Figure 3.1: Bulk densities over depth in project area

between 1500 - 1600 kg/m^3. This value is close to typical values of bulk densities for soft clay and thus appropriate to use within this study.

3.2. Water content

The water content associated with the bulk densities are presented showing the water content to vary between 40% and 70 % representing a subsoil with medium to high plasticity. Zooming in on Figure 3.2 provides a main variation especially between between 50 % and 60 %. Considering the high plasticity of the Holocene deposits, a representative water content of 60 % is found to be appropriate.

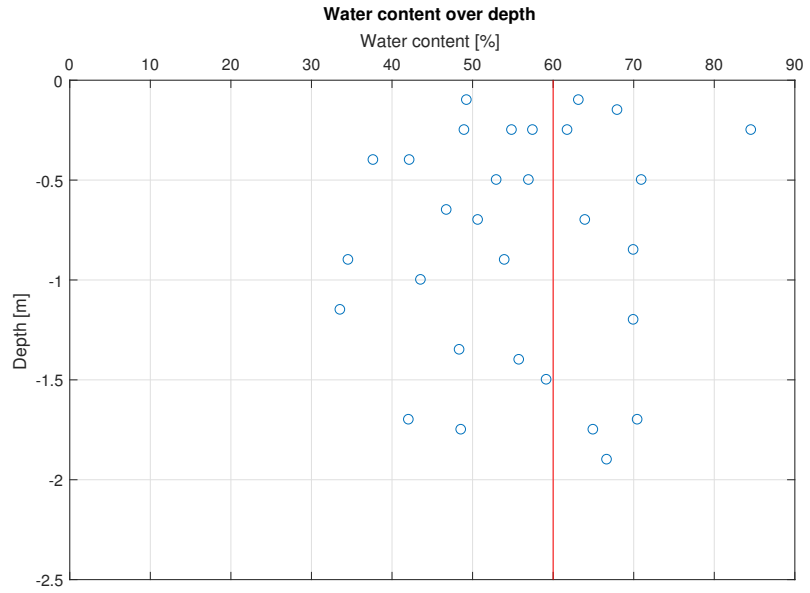

Figure 3.2: Water content over depth in project area

3.3. Atterberg limits

The next step in the analysis is to compare the water content with the Atterberg limits. These limits provide boundaries at which soil behaves like 'plastic' or as a 'liquid'. Locations where the water content reaches the

liquid limit, soil starts to behave as a fluid and thus starts to lose strength. On the contrary, approaching the plastic limit results in very plastic behaviour of soil. Atterberg limits approaching the water limit might therefore indicate the presence of Holocene deposits as these are easily deformable. Besides the plastic and liquid limit, a third parameter can be determined, the plasticity index. This parameter is determined as the difference between the liquid and plastic limit. Low values of plasticity index within the data, i.e. PI < 20, are disregarded as numbers in those range corresponds often to sandy/silty soils. Plasticity indices above 60 are considered to be scatter and are therefore not included in the analysis.

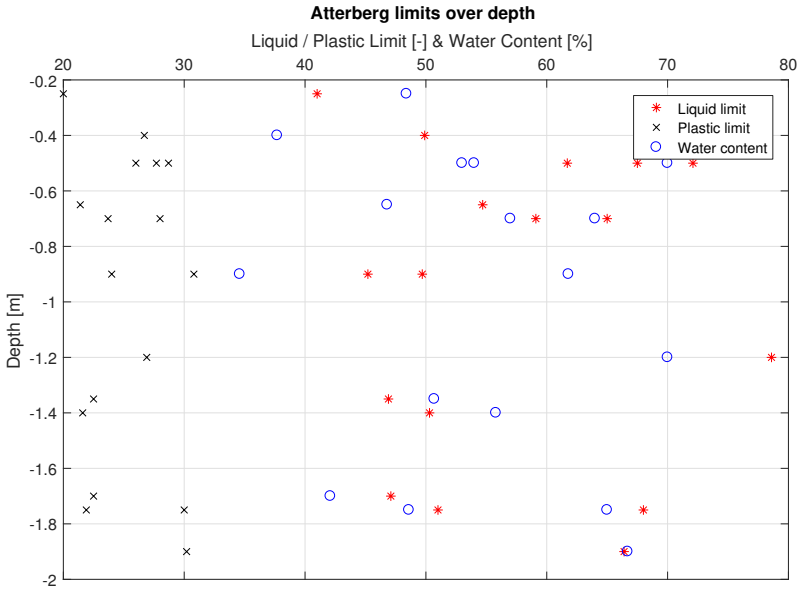

Figure 3.3: Atterberg limits with water content over depth in the project area

3.4. Undrained shear strength

To derive the classification parameters, boreholes were taken at different locations. Soil strengths have been determined by performing different tests at irregular depths. Pocket penetrometer and torvane tests are carried out and samples have been taken to perform UU triaxial tests. Cone penetration tests are performed as well at all pre-determined jacket installation locations. Before presenting the results, the strength tests are shortly described.

The pocket penetrometer consists of a gauge containing a telescoping rod which is pushed into the soil. The distance the rod goes into the soil corresponds to a certain compressive strength of the soil. However, the penetrometer is subjected to many errors for example in presence of non-uniform soil. The test may therefore be used to obtain a first approximation of the strength of the soil. It should not replace laboratory testing or field analysis and should not be used as design data. The torvane test is a four-finned probe, placed in undisturbed soil and is rotated. The amount of friction torque required to mobilise the soil outside the probe, i.e. to make the probe turn, is measured. This friction torque is used to calculate the yield strength of the soil outside the probe which equals the undrained shear strength of the soil. During both tests, stronger soils or boulders may be encountered resulting in deceptive undrained shear strengths and human errors may easily affect the results as well. The undrained unconsolidated triaxial test is the fastest way to find strength characteristics by means of a triaxial test. During the tests no consolidation occurs and water is not allowed to drain. ISO 19901-4 suggests that the strengths resulting from UU triaxial tests are often not plausible and should be used with care for (very) soft clay. The in-situ penetrometer and torvane tests are found to be more reliable techniques for determining the shear strength of soft clay and are therefore considered within the analysis.

The results from the penetrometer, torvane and UU triaxial tests are presented in Figure 3.4. The first 0.40 m shows the undrained shear strength to vary mainly between 10 and 30 kPa. Since the main interest lies at the Holocene deposits, these values are found too high to present the strengths. For increasing depth,

strengths are found with penetrometer and torvane tests varying between 15 and 30 kPa with some scatter corresponding to significant stronger soils or human errors during the tests. The results of the UU triaxial tests provide higher strengths overall seen and strength higher than 80 kPa are found as well, which are considered as scatter. Figure 3.4 shows clearly no trend which might present the strength profile over depth and the experiments provide strengths not representative to Holocene deposits.

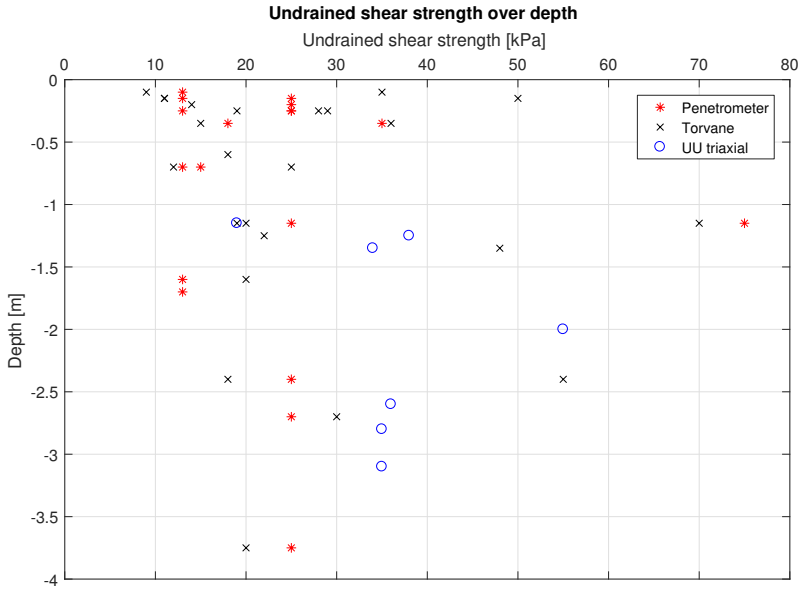

Figure 3.4: Undrained shear strength over depth based on test result from penetrometer, torvane and undrained unconsolidated triaxial tests

Therefore, the undrained shear strength over depth is determined using 70 CPTs carried out in the field. Raw data from the CPTs is analysed and interpret to determine the type of soils present in the Wikinger project area. Locations which might representative for Holocene deposits are determined based on their classification parameters. Using the availability of penetrometer and torvane tests, certain representative locations are chosen to derive the strength profile. The relation correlating the undrained shear strength and the cone resistance is given in Eq. (3.1).

$$s_u = \frac{q_t - \sigma_{vo}}{N_{kt}} \tag{3.1}$$

in which s_u is the undrained shear strength, σ_{vo} is the total stress, q_t is the corrected cone resistance and N_{kt} is a cone factor. In the following, the different components of this equation are highlighted.

The resistance measured by the CPTs needs to be corrected for pore pressure effects since the cross-sectional area of the rod is often smaller than the area of the cone resulting in pore pressures next to the rod producing additional force downwards. In the analysis, the measured cone resistance is corrected by modifying the cone resistance with the pore pressure on top of the cone multiplied by the tip net area ratio. The measurements are also corrected for the initial settlements occurred due to the self-weight of the equipment. In drained soils, the measured cone resistance equals the corrected resistance as the water is able to drain. In undrained soils, especially with very soft clay, it is important to correct the resistance.

$$q_t = q_c + (1 - a) * u_2 \tag{3.2}$$

with q_c as the measured cone resistance. a is the tip net area ratio defined as the ratio of rod over cone area depending on the manufacturer of the equipment used in the tests. The value may vary between 0.60 and 0.85 and therefore taken as 0.75 in this study. u_2 is the water pressure on top of the cone.

The cone factor in Eq. (3.1), N_{kt}, is determined by verifying the shear strength output from the CPTs with the in-situ penetrometer and torvane tests. CPT data for five representative locations is plot, based on their classification parameters, after which Eq. (3.1) is fit to the penetrometer and torvane tests by varying

the cone factor N_{kt}. Cone factors between 14 and 18 are obtained but mainly a cone factor of 18 fitted the experimental data best. Literature provides that cone factors varying between 15 and 20 for soft soils are commonly adopted [8]. Therefore, N_{kt} equals to 18 is considered as appropriate for the analysis assuming that the cone factor is representative for the total area.

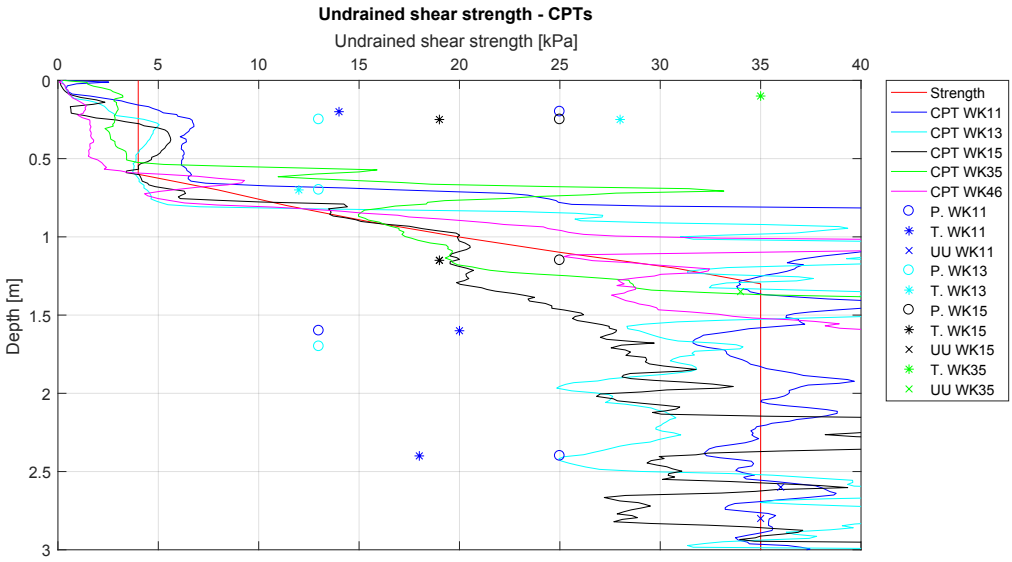

Figure 3.5: Undrained shear strength profile based on CPT data

The derived strength profile is shown in Figure 3.5. The area is shown to be characterised with an undrained shear strength up to 4 kPa near the subsurface and is more or less constant within the first 0.7 m. After 0.7 m, the strength is increasing significantly over a relatively small depth up to values which are not representative for Holocene deposits. This part of the subsoil, in which the strength is increasing linearly, corresponds to a soil layer consisting of different material. At depths larger than 1.0 - 1.2 m, the strength stops increasing linearly and remains constant within a certain range. This uniform strength over depth given by the CPTs is verified with the data obtained from the penetrometer, torvane and UU triaxial tests. Based on the comparison, the soil strata can be characterised as a three-layer system with a layer of soft clayey soil with a small undrained shear strength. Below this layer, a stronger layer is found in which the strength increases linearly over a small depth. The deepest layer found is characterised with an uniform strength over depth varying in a certain range.

A different way to present the strengths is in a normalised way. The undrained shear strength is normalised with the effective stress providing a linear relation between the strength and effective stress. For the soft soil strata, s_u/σ'_{vc} ratios of 1.1 - 1.2 have been found. As normally consolidated soils has usually ratios varying between 0.16 and 0.4 [23], this is an indication of over-consolidation of the soft clay. Considering the design procedure for the stability of soft soils presented by Ladd & Foott (1974), an overconsolidation ratio between 6 and 8 would be representative. An overconsolidation ratio of 6 is chosen for the analysis as the material, Maine Organic Clay, has almost equal Atterberg limits as the Holocene depositions in the Wikinger area [21].

Figure 3.5 shows the CPTs for certain locations starting at 0 kPa which is impossible since soil with no strength does not exist. As the strength varies up to 7 kPa until depths of 0.6/0.7 m, a constant undrained shear strength of 4 kPa is assumed to representative for the Holocene deposits. The strength of the intermediate layer increases drastically up to 35 kPa at a depth of 1.3 m. The bottom layer is assumed to have a constant strength of 35 kPa. As the operational performance of the pre-piling template is studied on soft soils, the soil is simplified to a single-layer system with an uniform strength over depth.

3.5. Critical locations

Using the strength profiles over depth, the locations where Holocene depositions might be present are determined. If the layer is close to or thicker than 0.80 m, the location is considered critical as the pre-piling template has the ability to jack-up its towers individually for only 0.80 m. In critical situations, settlements become uncontrollable providing difficulties during operation. Table 3.1 provides a brief overview of the locations at which Holocene depositions might present. The thicknesses and strengths of the top soft and intermediate, transition, layer are given. Half of the 23 locations at which soft soil is found are considered to be critical of which a few are exceeding the threshold of 0.80 m. Other locations possess thicknesses close to the threshold and therefore this case have to be considered with care.

Table 3.1: Brief overview of locations at which Holocene deposits are determined with thickness and strength of the top soft and intermediate soft layer. Critical locations are marked with *

Holocene deposits					
No.	Location	Top soft layer		Intermediate soft layer	
		Thickness [m]	s_u [kPa]	Thickness [m]	s_u [kPa]
1	WK01*	0.0 - 0.79	< 5.0	0.79 - 0.85	7.0 - 15.0
2	WK02	0.0 - 0.62	< 4.7	0.62 - 0.69	8.0 - 55.0
3	WK03*	0.0 - 0.79	< 4.7	0.79 - 1.06	7.8 - 38.2
4	WK04*	0.0 - 0.92	< 5.9	0.92 - 0.96	9.0 - 39.5
5	WK05*	0.0 - 0.78	< 6.2	0.78 - 0.80	7.6 - 13.6
6	WK06	0.0 - 0.60	< 5.8	0.63 - 0.65	14.0 - 14.3
7	WK08	0.0 - 0.59	< 6.4	0.60 - 1.20	7.3 - 23.7
8	WK09*	0.0 - 0.86	< 6.3	0.86 - 1.61	6.3 - 34.6
9	WK10	0.0 - 0.60	< 6.6	0.61 - 0.64	8.0 - 46.0
10	WK11	0.0 - 0.66	< 7.0	0.67 - 0.83	7.0 - 48.5
11	WK12	0.0 - 0.61	< 7.0	0.62 - 2.67	7.3 - 39.5
12	WK13*	0.0 - 0.81	< 6.7	0.82 - 1.03	12.0 - 39.2
13	WK14*	0.0 - 0.79	< 5.0	0.79 - 0.82	15.0 - 46.8
14	WK15*	0.0 - 0.76	< 6.1	0.76 - 2.15	8.0 - 35.0
15	WK19*	0.0 - 0.82	< 6.5	-	-
16	WK22	0.0 - 0.58	< 7.6	0.59 - 0.88	9.0 - 37.5
17	WK25*	0.0 - 0.95	< 5.4	0.96 - 1.29	7.2 - 38.7
18	WK26	0.0 - 0.60	< 5.0	0.62 - 0.76	8.7 - 35.1
19	WK30	0.0 - 0.65	< 6.3	0.66 - 1.60	7.0 - 42.7
20	WK34	0.0 - 0.63	< 6.7	0.63 - 1.73	7.0 - 41.2
21	WK36	0.0 - 0.56	< 6.0	0.57 - 1.54	11.0 - 41.0
22	WK37*	0.0 - 0.75	< 5.7	-	-
23	WK46*	0.0 - 0.80	< 6.2	0.80 - 1.61	8.3 - 38.8

3.6. Summary and discussion

An offshore site investigation is performed to characterise the soil in the Wikinger project area. Different kind of soil have been found, among other things, young soft marine sediments and very soft clay often denoted as Holocene depositions, which may cause difficulties during pile installation. Oedometer, triaxial and direct shear tests are performed for the strength parameters expect in the Holocene depositions as these are expected to scour away.

Using data from boreholes, representative values for density, water content and Atterberg limits are derived for the soft clay to examine whether soft soils are present. To derive the undrained shear strength, cone penetration tests are verified with scarce and controversial data available from penetrometer, torvane and UU triaxial tests which are taken irregularly over depth and locations to derive the cone factor to compute the undrained shear strength over depth. The experimental data included often scatter implying the presence of stronger soils/boulders or human errors. The cone factor is used to derive the measured cone resistance, which is corrected for the pore pressures on top of the cone. Based on the strength, a soil characterisation is given consisting of a three-layered system in which the soft soil has a constant increase over depth resting on top of layers with linearly and again uniformly increasing strength over depth. For this study, the soil is simplified to a single layer system consisting of soft soil with an undrained shear strength of 4 kPa.

4

Environmental Loads

This chapter describes the theory to determine the environmental loads and presents the load based on environmental data measured in the field. After positioning of the pre-piling template on the seabed, the piles are stabbed in the template, which are subjected to wave, current and wind loading. Via the piles and template is the loading transferred to the subsoil. By integration of the loads over the piles, the total forces acting on the soil are determined. The main source of the loading is the wave loads. The theory behind the wave loading is explained after which the current and wind loads are discussed as well. The environmental conditions measured within the field are presented followed by the derivation of the loads used during this study.

4.1. Wave loads

Wave loads contribute primarily to the total environmental loading experienced by an offshore structure. This loading consists actually of different components contributing all to the loading exerted to the structure. This section describes how the wave load is calculated. Furthermore, the components contributing to the load are given and is explained how these contribute to the wave load.

After positioning of the piles in the sleeves, the piles are subjected to wave loading. The loading acting on the piles can be simplified to loading acting on slender cylinders. In order to apply this simplification, the following condition needs to be met. The pile's outer diameter should be rather small compared to the wave length, i.e. ratio of D over λ should be smaller than 0.1 to 0.2. This method divides the pile into small pieces at which the loads are determined providing loads per unit meter. To determine the total load transferred to the subsoil and thus experienced by the soil, the loads are basically integrated over the total pile length. As this approach is often used for its simplicity, it is well worth to state its basic assumptions. The ambient water motions in the immediate vicinity around the structure are considered to be equal at any time instant. The spatial variation of ambient motions in both horizontal and vertical direction are neglected.

Secondly, the flow around the cylinder is considered to be two-dimensional implying that the flow and the resulting forces parallel to the cylinder axes are neglected. The resulting loads are due to the ambient flow and cylinder motion components perpendicular to the cylinder axes. To determine the resulting motions, the water particle velocity and acceleration needs to be defined. The particle velocities in the x- and z-direction can be calculated by taking the partial derivation of the velocity potentials.

$$u = \frac{\partial \Phi_w}{\partial x} = \frac{dx}{dt} = \zeta_a \omega \frac{cosh[k(h+z)]}{sinh(kz)} \cdot cos(kx - \omega t) \tag{4.1}$$

$$w = \frac{\partial \Phi_w}{\partial z} = \frac{dz}{dt} = \zeta_a \omega \frac{sinh[k(h+z)]}{sinh(kz)} \cdot sin(kx - \omega t) \tag{4.2}$$

with ζ_a as the wave amplitude, ω as the wave frequency, k as the wave number and h as the water depth. The equations for the resulting water motions are often described with the following equations in which the $\zeta_a \omega$ times the fraction term is denoted as u_a.

$$u(t) = u_a \cdot cos(kx - \omega t) \tag{4.3}$$

in which u_a is the amplitude of the wave generated horizontal water velocity at an elevation z in m/s. The acceleration of the water particles is obtained by taking the time derivative of the particle velocity.

$$\dot{u}(t) = -\omega u_a \cdot sin(kx - \omega t) \tag{4.4}$$

Potential theory is well-known for its describing capabilities of the behaviour of waves. The presented equations in this section are therefore considered as suitable to determine the velocities and accelerations of undisturbed wave flow for the load calculation [20].

The piles and pre-piling template experiences wave loading composed of different components. This section describes these different components.

- Inertia force
- Drag force

Inertia force

The first component is the inertia force, which is related to added mass of the body in water. This force can be subdivided into two components, the Froude-Krylov force and the disturbance force. Imagine first an undisturbed flow without any cylinder disrupting the flow. According to the second law of motion of Newton accelerations are resulting from forces. Therefore, the horizontal acceleration of the ambient flow must be resulting from a force in the water which, in turn, must arise from horizontal pressure gradients. These gradients are always present, with and without a cylinder in the flow. The force resulting from these gradients is the Froude-Krylov force and is described by Eq. (4.5).

$$F_{FK} = \rho \pi R^2 \cdot \dot{u}(t) \tag{4.5}$$

As the flow is disturbed when a cylinder enters the water, an additional term has to be added. Since the cylinder is impermeable, the fluid is forced to go around the cylinder which results local velocities and accelerations around the slender structure. Again according to the Law of Newton, this is only possible if a force is exerted on the fluid coming from the cylinder. This extra force, causing the disturbance field around the cylinder, is taken into account by considering the difference in kinetic energy of the disturbed and undisturbed flow field.

$$F_{dis} = \rho \pi R^2 \cdot \dot{u}(t) \tag{4.6}$$

As both have the same phase, the total inertia force is the sum of Eqs. (4.5) and (4.6).

$$F_I(t) = F_{FK} + F_{dis} = 2 \cdot \rho \pi R^2 \cdot \dot{u}(t) \tag{4.7}$$

$$= C_M \cdot \rho \pi R^2 \cdot \dot{u}(t) \tag{4.8}$$

in which ρ is the density of the fluid and R is the radius of the slender structure. The theoretical value of 2 in Eq. (4.8) is often replaced by an experimental coefficient, the inertia coefficient C_M. The theoretical coefficient of 1 resulting from the Froude-Krylov force is considered as suitable as potential theory describes the water motion in undisturbed waves well. However, the coefficient for the disturbed flow is usually lower than 1. The effect of the disturbed flow is taken into account by using the added mass coefficient, C_a. Therefore, the inertia coefficient, C_M, equals $1 + C_a$.

Drag force

The second component contributing to the wave loading is the drag force, which is the component in the direction of the flow velocity. By means of experiments was shown that the drag force, which is proportional to u^2 and D, was caused by a constant current. As the drag force is in equal direction as the flow velocity, the constant current u^2 is replaced by its time-dependent counterpart in order to remain the proper sign. Substituting the equations found for the water particles, the following equation is found to calculate the drag load.

$$F_D(t) = \frac{1}{2} \rho C_D D u_a^2 \cdot cos(kx - \omega t) |cos(kx - \omega t)| \tag{4.9}$$

in which F_D is the drag force per unit length, C_D is the drag coefficient and D is the diameter of the slender structure. The drag coefficient should be derived for an oscillating flow which is time dependent rather than for a constant flow.

Morison Equation

The Morison Equation is used to determine the wave loading on the piles. The linear inertia term and the quadratic drag term are basically superposed to obtain a resultant load per unit length. As the two components are added to each other, a phase difference of 90 ° occurs which is visible when plotting Eqs. (4.8) and (4.9).

$$F(t) = \frac{\pi}{4}\rho C_M D^2 \cdot \dot{u}(t) + \frac{1}{2}\rho C_D D \cdot u(t)|u(t)| \tag{4.10}$$

Inertia and drag coefficients

Extensive research with different methods is performed in order to determine the inertia and drag coefficients, C_M and C_D. Different experimental setups and methods are available to process the measurements and derive these coefficients. More information about the different experimental setups and methods can be found in Chapter 12, Offshore Hydromechanics [20].

In this section a brief overview is given of the available values which are currently used for the inertia and drag coefficients. The coefficients are derived using different approaches and therefore a discrepancy in C_M and C_D is observed when deriving the coefficients from exactly the same time series. It is impossible to expect the exact same values for C_M and C_D for different methods, only values with a tolerance of several percent may be expected. Since the inertia and drag coefficients are found for a certain flow condition, the next step is often to present these nicely in a graph as a function of a certain variable making it useful for design.

The coefficients can be shown as a function of many variables. Coefficients have been presented as function of the Reynolds number, the Froude number, the Keulegan-Carpenter numer, the Iversen modulus, the Sarpkaya beta and as a function of the dimensionless roughness of the surface of the structure. Expressing the coefficients as a function of the Keulegan-Carpenter number, defined as $u_a \cdot T/D$, provides the most suitable and realistic results. Some of the researches extended their work by providing the coefficients as a function of two variables instead of one. In the following, a brief review is given of the values which are commonly used in practice.

A significant amount of research is performed on the inertia and drag coefficients. The applicability of the coefficients are limited to the specific tests conditions. Clauss (1992) suggested for example coefficients which are a function of both the Keulegan-Carpenter number and the Reynolds number.

Table 4.1: C_M and C_D values [4]

	$Rn < 10^5$		$Rn > 10^5$	
KC	C_D	C_M	C_D	C_M
< 10	1.2	2.0	0.6	2.0
> 10	1.2	1.5	0.6	1.5

Sarpkaya performed experiments with smooth cylinders in U-tubes to obtain inertia and drag coefficients for which the results of the tests are presented as a function of $\beta = D^2/\nu \cdot T = Rn/KC$ and the KC number. Guidelines as Det Norske Veritas, the American Petroleum Institute and the Society of Naval Architects and Marine Engineers proposed values for C_M and C_M as well. Those proposed by DNV and API are currently most widely accepted. DNV provided coefficients in graphs as a function of the KC number and the roughness of the surface of the cylinder, while API and SNAME provided values in a table distinguishing smooth and rough cylinders. API provides C_M values varying from 1.2 - 1.6 and C_D values of 0.65 - 1.05, while SNAME proposes 1.8 - 2 and 0.65 - 1.0 for inertia and drag coefficients, respectively. Considering the values provided in literature for low Keulegan-Carpenter values (KC < 1), which means that the load is inertia dominated, an inertia coefficient of 2.0 and a drag coefficient of 1.2 is incorporated within this study.

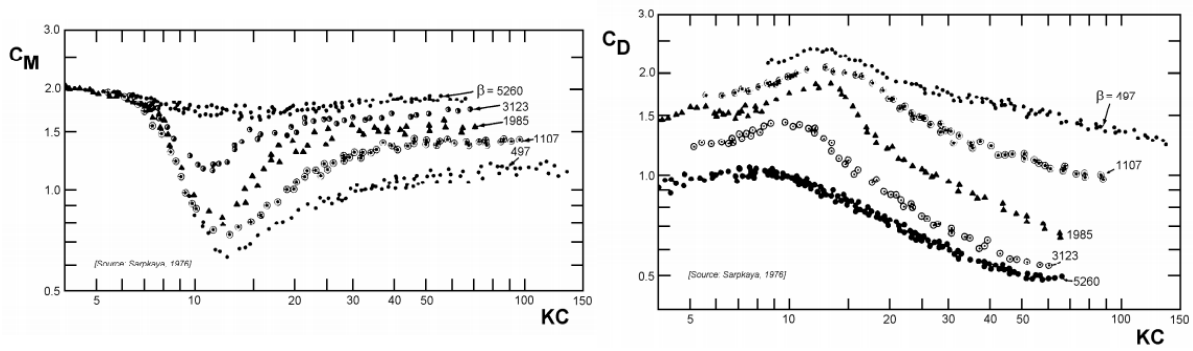

Figure 4.1: Laboratory results for C_M and C_D as function of β and Keulegan-Carpenter number from Sarpkaya

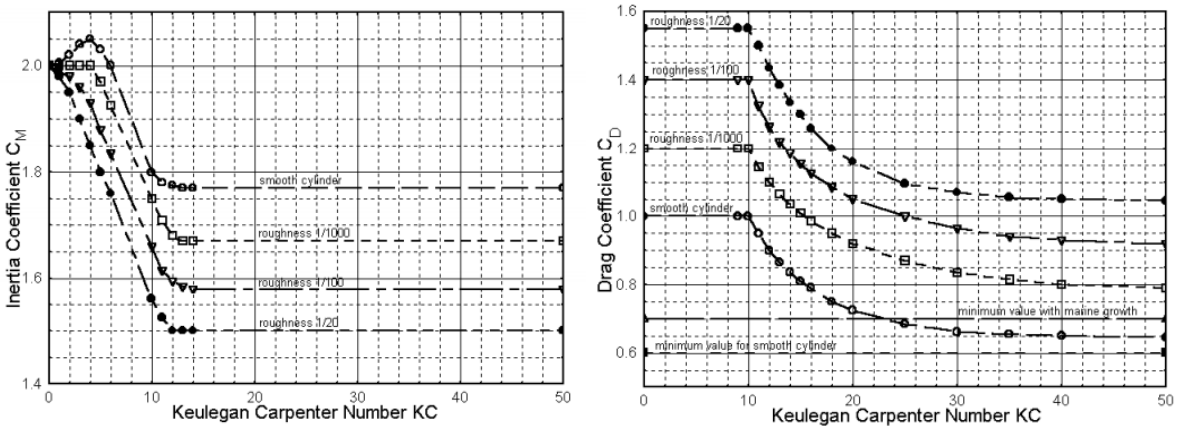

Figure 4.2: Suggested values for C_M and C_D as function of the Keulegan-Carpenter number and the roughness of the surface of the cylinder by Det Norske Veritas

4.2. Current and wind loads

Next to waves, currents are also present resulting in additional loads onto the piles. However, in much less extent compared to the wave loading. As the piles are larger in length than the water depth, they reach out of the water and are subjected to wind resulting in additional loads to be transferred to the subsoil. In this section, the velocity profiles of these additional load sources are given and is discussed how the loads due to the current and wind are computed.

Measurements are taken within the project area. Based on the results, it was very challenging to model the hydrodynamic behaviour of the currents with present standard models which were not able to capture the local behaviour. Therefore, a decision was made to base the design of the project on a five years time series measured close to the Wikinger project area. The data set is collected using an Acoustic Wave and Current Profiler which showed that the current profile could be described by the idealised $1/7^{th}$ power law which is normally used for tidal currents.

$$U_c(z) = U_{c,sub} \cdot \left(\frac{d+z}{d}\right)^{1/7} \tag{4.11}$$

The drag load due to the current is calculated using the Morison Equation. The total drag load is calculated by taking the sum of the velocities of the water particles and current. Computing the loads individually for the waves and currents and superposing at the end of the calculation would result in underestimation. Since the current is not time dependent, it cancels out for the acceleration of the water particles. Wind loads

are especially involved when the hammer is placed on top of the piles for the driving operation. The occurring wind velocity profile is approximated using the idealised $1/7^{th}$ power law depending on the wind speed measured at 10 m height, measured offshore.

$$U_w(z) = U_{w,10} \cdot \left(\frac{z}{h_{10}}\right)^{1/7} \tag{4.12}$$

The drag loads resulting from the wind are calculated with Eq. 4.13.

$$F_w(t) = \frac{1}{2}\rho C_D D \cdot U_w |U_w| \tag{4.13}$$

4.3. Environmental conditions

Devices were present in the field to measure the different wave, current and wind characteristics. These are used to set the environmental conditions for the operational limits for the pile driving operation. Executing operations with higher operational waves will result in the difficulties in the bottom stability of the pre-piling template. In this section, the measured environmental conditions within the area are given. Based on this information, two load cases are determined for which the bottom stability of the pre-piling template will be assessed.

Along the measurements, the directions of the waves are measured. A wave rose is constructed containing the average of a data set of 1 year presenting this data nicely.

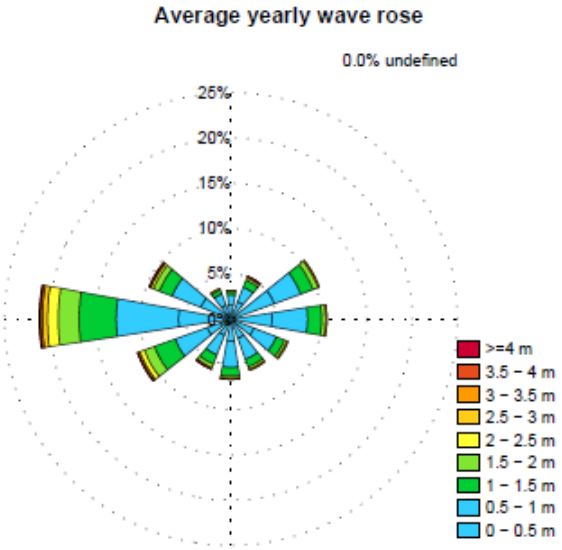

Figure 4.3: Average yearly wave rose of measurements in project area

To provide representative load cases, the direction of the wave loading is considered first. Figure 4.3 shows the waves mainly arising from the west, i.e. 270 ° covering 42 % of the data set of a one-year time series. In a lesser extent, waves are arising from northeast to the east, i.e. 60 to 90 °, which covers 21 % of the data set. Assuming this one year time series to be representative for the waves in the field, the west and northeast are considered as main directions of the waves.

These two main wave directions are taken as base for the two load cases. In the first load case, the waves are arising from the west which results in that the piles and pre-piling template are loaded horizontally. The second load case considers the waves from the northeast which results in a diagonal load case. To have a certain conservatism, the load in the diagonal load case is considered not with an angle of 60 ° but with 45 °. This load case is usually examined assuming the intermediate footings to hardly take any load for its account which results in full compression and full release of a single mud mat.

The first load case assumes horizontal loading of the pre-piling template. Wave heights higher than 2.25

m in this specific direction does hardly occur (<2 %). Therefore, wave height of 2.25 m is considered covering more than 97 % of the total data set. The wave heights and corresponding peak periods measured are used to construct scatter diagrams. Corresponding peak periods are chosen using the scatter diagrams. For a wave height H_s of 2.25 m, peak periods between 6 and 7 seconds are found mainly to occur. Therefore, a peak period of 7 seconds is chosen. Scatter diagrams are also plot expressing a correlation between the significant wave height and measured wind speeds. Assuming the wave height chosen in load case 1 results in a wind speed of 15 m/s.

In the second load case, waves are found not to be higher than 1.75 m. Incorporating a significant wave height of 1.75 m covers 93 % of the data set and is therefore found to be appropriate. Corresponding peak period and wind speed are determined with the correlations in Figure 4.4. A peak period between 5 and 7 seconds corresponds to a significant wave height of 1.75 m. For this load case, a period of 5 seconds and a wind speeds of 12 m/s are chosen as operational limits.

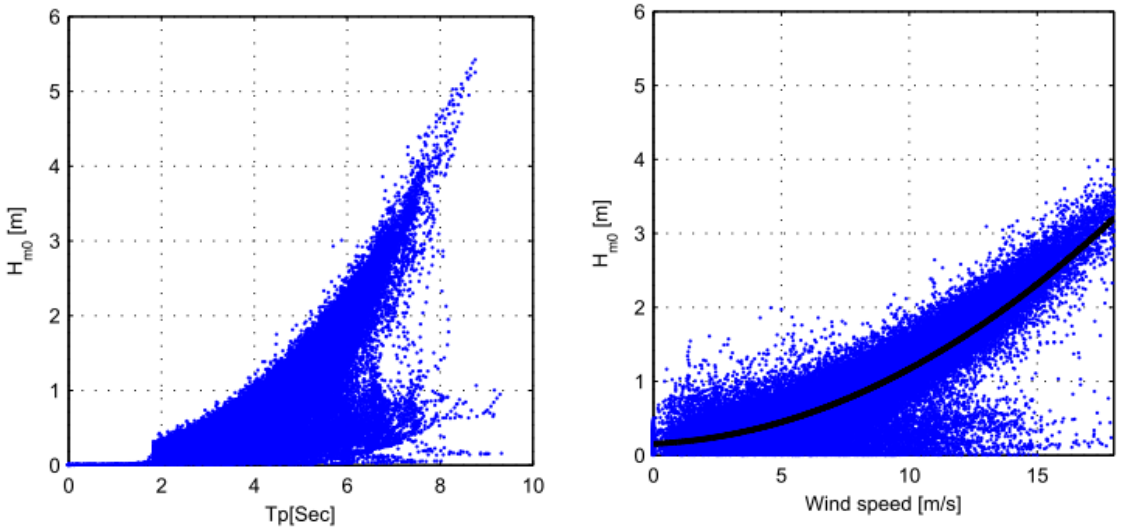

Figure 4.4: Scatter diagrams with the relation between the significant wave height and peak period (L) and the significant wave height and wind speed (R) from measurements in project area

Standard models were not able to describe the local behaviour of the currents. Instead a five years data set from a measurement device close to the project area is used for the design. The average current velocity is found to be 0.13 - 0.14 m/s over depth. This velocity is rather small and the current will therefore not impede the operations offshore. However, to be conservative, a current velocity of 0.30 m/s is taken into account and is taken constant during all computations.

Wind, waves and the current may all arise from different directions at different time moments resulting in loading from different directions, which might be beneficial. A major assumption considered currently in studies and also assumed in this study is that all of the load components are acting simultaneously in the same direction. This does not represent the reality, the actual load will be overestimated and therefore a certain conservatism is build-in in the calculations.

4.4. Loads

This section provides the total hydrodynamic and wind loads experienced by the piles and pre-piling template. The loads are distributed over the mud mats showing the amount of load the soil has to bear. In this study is assumed that the piles do not penetrate into the soil due to self-weight and therefore is chosen to consider the total pile length during the load calculations.

The total hydrodynamic load and wind load acting on the piles is determined at t = 0. The time dependency of the hydrodynamic load is incorporated in time steps of $\triangle$t = 0.1 s. The wind loading is added as a static load to obtain the total load acting on the system. The loads are assumed to be quasi-static and are

calculated for different pile combinations for both load cases. The load orientations for the horizontal and diagonal loading cases are given in Figure 4.5 including the neutral axis around which the template will rotate due to the impact of the moment loading.

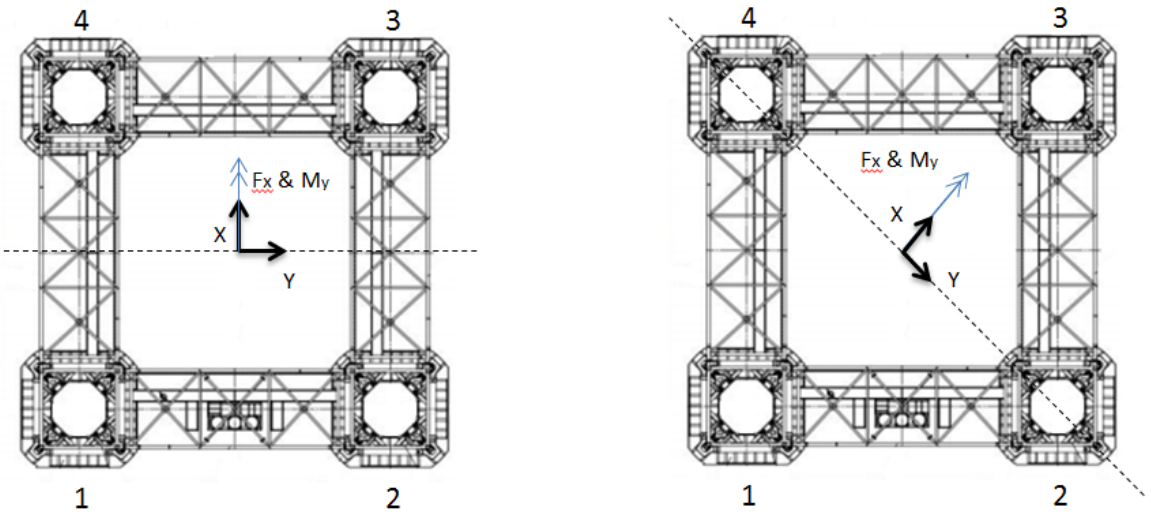

Figure 4.5: Load directions for horizontal (L) and diagonal (R) loading case including its neutral axis

The piles are stabbed individually resulting in different loads each time. With increasing piles, the loads are expected to increase as well. However, the sequence of stabbing the piles might affect the loading. Hence, the maximum horizontal and moment loading for different pile combinations are calculated and presented in Table 4.2.

Table 4.2: Loads on different pile combinations considering the horizontal loading case

Pile combination	$F_x(t)$	$M_y(tm)$
1 or 2	26.07	762.53
3 or 4	25.80	751.19
1 & 2	49.26	1428.58
3 & 4	48.83	1411.59
1 & 3	34.50	1005.20
1, 2 & 3	53.26	1533.11
1, 3 & 4	52.76	1534.77
1, 2, 3 & 4	65.58	1910.09

The loads remain equal with equal amount of piles stabbed except in case that piles 1 & 3 are stabbed during in less loads. The maximum loads are obtained in case that all piles are stabbed in the template. As hydrodynamic loads do cycle over time, its time-dependent character is shown in Figure 4.6. The restoring moment due to self-weight is presented as well showing that the moment due to environmental loading will not cause mechanical stability issues.

The loads are transferred via the piles and template to the subsoil. The piles stabbed are fixed by the installed rollers in the towers of the template. As the template self acts as a single rigid body due to high rigidity of the lattice beams, the loads are assumed to act in the center of the template. The horizontal load is transmitted through the soil as shear stresses. The moment loading is distributed and decoupled over the mud mats. The resulting compressive loads from self-weight and moment have to be balanced by the soil reactions beneath the mud mats which is the total vertical load experienced by the footings. During horizontal loading, mud mats 3 & 4 contribute to the compressive load transfer. An overview of the loads experienced for each single mud mat are given in Table 4.3.

The resulting horizontal load and overturning moment are calculated for the diagonal loading case as

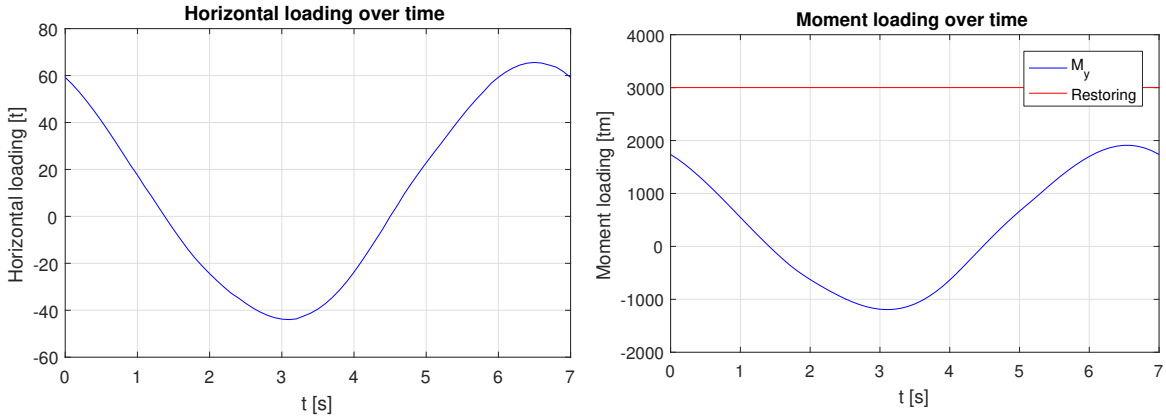

Figure 4.6: Distributed environmental load integrated over the pile length and its accompanying moment loading for load case 1

Table 4.3: Loads per individual mud mat considering the horizontal loading case

Loads per mud mat [kN]					
Pile combination		1	2	3	4
1 or 2	V	489.7	489.7	815.0	815.0
	H	63.9	63.9	63.9	63.9
3 or 4	V	492.2	492.2	812.6	812.6
	H	63.3	63.3	63.3	63.3
1 & 2	V	347.7	347.7	957.0	957.0
	H	120.8	120.8	120.8	120.8
3 & 4	V	351.3	351.3	953.4	953.4
	H	84.6	84.6	84.6	84.6
1 & 3	V	438.0	438.0	866.7	866.7
	H	84.6	84.6	84.6	84.6
1, 2 & 3	V	325.4	325.4	979.3	979.3
	H	130.6	130.6	130.6	130.6
1, 3 & 4	V	325.1	325.1	979.7	979.7
	H	129.4	129.4	129.4	129.4
1, 2, 3 & 4	V	245.0	245.0	1059.7	1059.7
	H	160.8	160.8	160.8	160.8

well. The loading acts in the direction from mud mat 1 towards mud mat 3 causing mud mat 3 to be fully in compression. The loads for different configurations of pile stabbing sequence are calculated as well and given in Table 4.4.

Table 4.4: Loads with different pile combinations considering the second load case

Pile combination	$F_x(t)$	$M_y(tm)$
1 or 2	19.37	660.93
3 or 4	19.34	658.34
1 & 2	13.90	474.90
3 & 4	12.92	440.67
1 & 3	33.76	1143.84
2, 3 & 4	22.64	736.47
1, 2 & 4	22.04	732.23
1, 3 & 4	19.81	683.17
1, 2, 3 & 4	8.63	303.17

During diagonal loading is found that more piles does not directly imply a higher load experienced by the system. For all four piles is found that the loads cancel each other out while for pile combination 1 & 3 higher loads are obtained. The distance between the diagonal piles which equals 32.5 m coincides with the wave length for T_p resulting in loads which are in phase and therefore higher. The resulting loads are distributed over the mud mats and presented in Table 4.5 showing that mud mat 3 is fully in compression and mud mat is in relaxation since mud mats 2 and 4 does not contribute to the load transfer and are therefore only subjected to the self-weight. The loads provide that pile combination 1 and 3 is able to create uplift. Since the mass of the hammer, 215 t, on top of the pile and the mass of the piles, 136 t each, are not included, uplift is not expected.

Table 4.5: Loads per individual mud mat considering the diagonal load case

Loads per mud mat [kN]					
Pile combination		1	2	3	4
1 or 2	V	253.7	652.4	1051.0	652.4
	H	47.5	47.5	47.5	47.5
3 or 4	V	255.3	652.4	1049.5	652.4
	H	47.4	47.4	47.4	47.4
1 & 2	V	365.9	652.4	938.8	652.4
	H	34.1	34.1	34.1	34.1
3 & 4	V	386.6	652.4	918.2	652.4
	H	31.7	31.7	31.7	31.7
1 & 3	V	-37.6	652.4	1342.32	652.4
	H	82.8	82.8	82.8	82.8
1, 2 & 4	V	210.7	652.4	1094.0	652.4
	H	54.1	54.1	54.1	54.1
1, 3 & 4	V	240.3	652.4	1064.4	652.4
	H	48.6	48.6	48.6	48.6
2, 3 & 4	V	208.1	652.4	1096.6	652.4
	H	55.5	55.5	55.5	55.5
1, 2, 3 & 4	V	469.5	652.4	835.2	652.4
	H	21.1	21.1	21.1	21.1

The time-dependent horizontal and moment loading are given in Figure 4.7 for pile combination 1 & 3 since these result in the highest loads. Mechanical instability is not considered as an issue since the restoring moment is found to be higher than the resulting environmental moment.

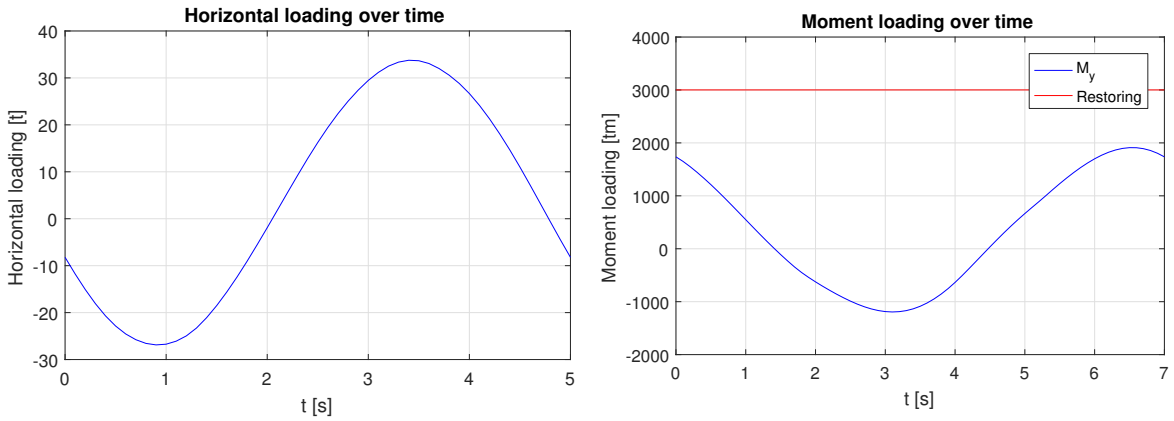

Figure 4.7: Distributed environmental load integrated over the pile length and its accompanying moment loading for load case 2

During diagonal loading, the pre-piling template tends to rotate around the diagonal perpendicular to the loading direction. The center of rotation is assumed to be in the centre of the structure allowing to consider

a single mud mat taking the total compressive load while the other mud mat is in full relaxation. This is conservative as in reality a shift in centre of rotation is expected to occur. Due to the shift, the intermediate mud mats will contribute to the load transfer as well. The load distribution is determined using the software Plaxis 3D as the problem is an interaction between structure, soil and loading. Four mud mats, rigid bodies rigidly connected to each other, are modelled on an elastic foundation to save upon calculation time. The load is defined at the centre of the structure with a lever arm resulting in the same moment loading as provided in Table 4.4.

Plaxis 3D provided the stress distributions beneath the mud mats which are integrated over the area to find an uniform total stress. This is corrected for the water pressures providing the effective stresses. With the uniform stress, the load distribution to the mud mats is determined and therefore the direction in the shift in center of rotation as well. The distributions for different levels of moment loading are determined and presented in Table 4.6.

Table 4.6: Distribution of load to the mud mats for the different pile combinations in the diagonal loading case

Loads [t]	Compressed [%]			Released [%]		
	1	2/4	3	1	2/4	3
8.63	0	0	100	97	1.5	0
12.92	0	0	100	97	1.5	0
13.90	0	0	100	97	1.5	0
19.34	0	0	100	97	1.5	0
19.37	0	0	100	97	1.5	0
19.81	0	0	100	97	1.5	0
22.04	0	0	100	97	1.5	0
22.64	0	0	100	97	1.5	0
33.76	0	0	100	97	1.5	0

Table 4.6 shows that the level of moment loading does not affect the distributions of the loading. The compressive load is fully taken by a single mud mat, while the intermediate footings cope with a small part of the tensile loading. Figure 4.8 is an extraction from Plaxis 3D and shows the effective stresses beneath the mud mats for all piles stabbed in the template. Considering that the load is in positive x, y direction, the load results in compression in mud mat 3, indicated with the yellow to red colour, and relaxation in mud mat 1, indicated by blue. At the intermediate mud mats, both compressive and tensile stresses are observed at the edges. However, all the intense colours present stress concentrations which is a known issue in numerical modelling.

To find the direction of the shift, the mud mat is divided and the effective stresses beneath are integrated over the area to find a representative effective stress for the total mud mat. Comparing the representative stresses showed that the intermediate mud mats experienced little tensile stresses implying that the neutral axis at which the pre-piling tends to rotate is slightly shifted in the direction of the loading. However, this effect is little and is therefore negligible.

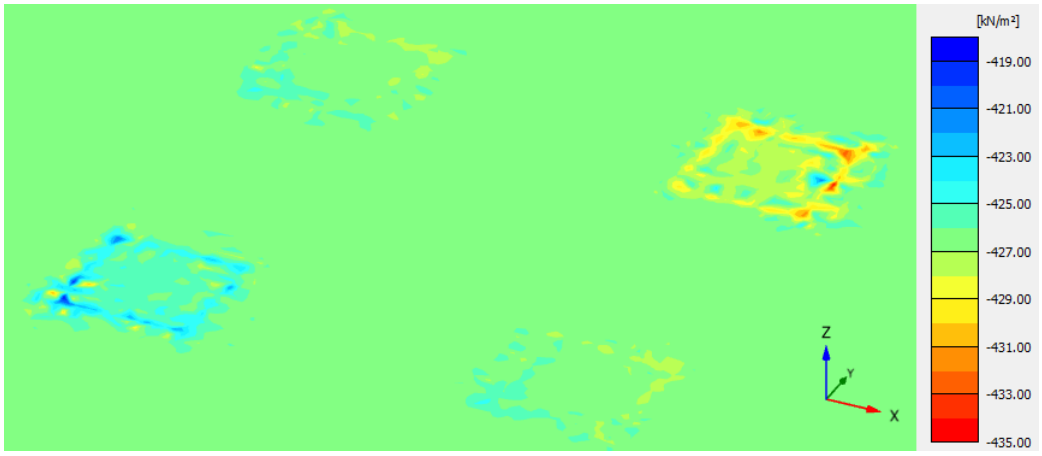

Figure 4.8: Load distribution over the mud mats with diagonal loading

4.5. Dynamic analysis

The hydrodynamic load acting on the piles and pre-piling is assumed to be slow enough such that inertial effects can be ignored. Hence, time, as only the maximum load is taken, and the inertial mass are not considered to be important. To justify this, a dynamic analysis is performed to see if the system is accelerated due to the hydrodynamic loads implying that the inertial effects may not be neglected.

An equivalent model of the actual pre-piling template is derived in order to the determine the equations of motion. These equations are used to determine the natural frequencies of the system. Comparing these frequencies with the excitation frequencies, possible dynamic amplification can be observed and therefore the assumption of considering the load to be quasi-static can be justified.

This section describes the simplification of the pre-piling template given with a visualisation of the incorporated model. Theory is given regarding the spring stiffnesses of this soil-structure problem and an overview is given of the parameters used in this analysis. The natural periods of the system are derived whereupon a comparison is given with the excitation periods.

Model of the pre-piling template

The pre-piling template is a structure consisting of steel tubular elements connected to each other with gaps between the elements. To perform the dynamic analysis, the structure is simplified to a two-dimensional problem as the structure is symmetric and is loaded in the center. Since it is assumed that the system acts as a rigid system with lattice beams connecting the towers rigidly and piles fixed by the rollers in the towers, the actual structure may be simplified to an equivalent beam structure with equal mass and mass moment of inertia properties. In order to derive the dimensions of this equivalent structure, the mass moment of inertia of the pre-piling template is calculated.

$$I_{m,y} = \int_A \rho(x,y,z) \cdot x^2 \, dA \tag{4.14}$$

in which $\rho(x,y,z)$ is the mass density in units of mass per unit length and x is the distance to the axis over which the system rotates. To determine the mass moment of inertia, all main structural elements are considered of the towers, lattice beams and mud mats. The secondary diagonal braces and plates are believed to be of little influence and therefore not included. For each individual element, numbered according to the structural drawings in Appendix B, the density, the length and the lever arm towards the center of rotation is determined, which is assumed to be in the center of the template. Superposing the values for all elements provides an approximation of the mass moment of inertia. After calculating the mass moment of inertia, the radius of gyration is determined. For a complex shaped structure with several rotating masses about an axis in a two-dimensional plane, the radius of gyration is defined as the distance to that axis such that the total mass can be concentrated in one point to obtain the same mass moment of inertia. The radius of gyration is calculated with Eq. (4.15).

$$R_y = \sqrt{\frac{I_{m,y}}{m}} \tag{4.15}$$

Since the mass moment of inertia is determined, $\rho(x, y, z)$ is known and the radius of gyration is the lever arm to the axis, dA can be solved providing the dimensions of the equivalent square to be used in this analysis. The following mass moment of inertia and radius of gyration are obtained on which is elaborated in Appendix C.

$$I_{m,y} = 1.01 \cdot 10^7 kg \cdot m^2$$

$$R_y = \sqrt{\frac{1.01 \cdot 10^7}{266 \cdot 10^3}} = 6.15m$$

The equivalent structure represents the mud mats, therefore the mass density of the mud mats, $\rho = 318.3 kg/m^2$, is considered to determine the dimensions of the square. Substituting all the known parameters in Eq. (4.14) results in the following parameters.

$$1.01 \cdot 10^7 = \int_A 318.3 \cdot 6.15^2 dA$$

Solving dA provides the area of the equivalent square structure.

$$L = B = 28.9m$$

The same procedure is applied to determine the second order moment of area for the dynamic analysis. Assuming the center of gravity to be perfectly in the center of the template and at half of the height of the lattice beams, the lever arms are determined for the individual elements to obtain the second moment of area about the center of gravity. By superposing the second order moments of the elements and the contribution of Steiner's theorem, the proper second order moment of area is determined on which is elaborated in Appendix C. The second order moment, I'_y, is determined to be:

$$I'_y = I_y + a^2 A = 6.16 \cdot 10^{13} mm^4$$

The mud mats in contact with the soil are representing the supporting points of the structure. The footings are able to move in the horizontal and vertical direction and therefore two springs are added at each corner for each possible movement of the footings. The vertical springs are also able to create a moment loading as soon as the structure wants to rotate. The vertical springs may be replaced by two springs in the center, a vertical spring and a rotational spring. As the considered spring stiffnesses are known, this model is believed to present the actual situation more suitable. The load F(t) acts on the contact point between the pile and template, the roller, as the load is introduced via the rollers into the template. Since, the main interest lies within the natural periods of the structure, an idealisation is proposed without dashpots as the system has to be analysed with free vibrations.

Spring stiffness

An important step in the dynamic analysis of soil-structure systems is the estimation of the spring stiffness to determine the resistance of the system to a certain motion when subjected to harmonic loading and to determine the natural periods of the structure.

Different numerical and analytical studies are performed to develop simplified methods, which may be used as a practical alternative instead of using computational power. This allows for a fast analysis of the problem. Gazetas (1991) performed a study aiming to provide a complete set of algebraic formulas and charts to compute the dynamic stiffnesses and damping coefficients of footings oscillating on a homogeneous half-space.

Gazetas stated a set of key characteristics which are found important to the soil-structure interaction problem. Coefficients incorporated in an analysis has to adequately reflect the shape of the soil-footing interface as the geometry of the structure influences these values. Other key characteristics to be taken into account are the amount of embedment of the footing and the composition of the soil. Stiffness and dashpot

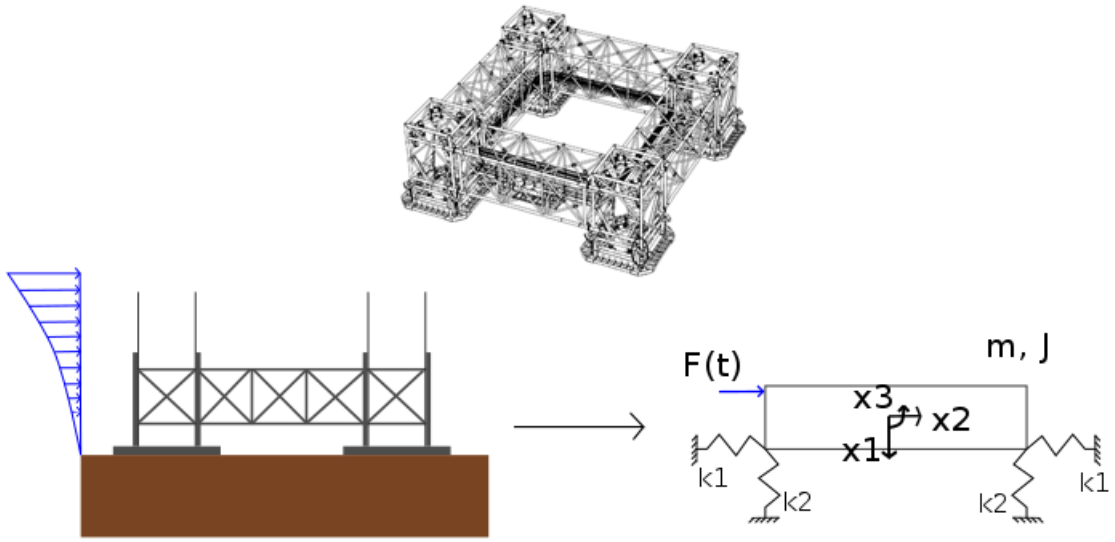

Figure 4.9: Actual and simplified model of the pre-piling template used in the dynamic analysis

coefficients may vary for soils which are uniform over depth and for soils consisting of layered depositions. The mode of vibration and the excitation frequency influences these parameters as well.

Soil properties are known to be frequency independent. However, the dynamic stiffness is a function of the frequency which presents the influence of the frequency on the inertia of the soil. The dashpot term reflects the radiation as energy is spread away by waves moving into the soil and the material damping generated in the system, which is the dissipation of energy due to hysteresis in the soil.

Gazetas presented tables for arbitrarily shaped footings on surface and at embedment in which algebraic expressions and associated graphs are given compiled from previous publications by the author and his coworkers. Algebraic expressions are presented to estimate the dynamic stiffnesses and damping coefficients for six and eight different vibration modes for surface and embedded foundations, respectively. The equations and graphs cover nearly all foundations except ring shaped geometries. A difference is made between footings which are partial and which are fully embedded. The provided expressions and graphs may only be used in case a reasonably deep and uniform soil deposition is considered which can be modelled as a homogeneous half-space.

To determine the spring stiffnesses, first the static stiffness with $\omega = 0$, denoted with a capital K, is derived. This stiffness is derived for footings on surface of a homogeneous half-space according to the dimensionless graphs presented by Gazetas. By multiplying the static stiffness with the dynamic stiffness coefficient, denoted with a small k, the frequency dependency of the stiffnesses is incorporated resulting in the dynamic stiffness. Latter coefficients are presented in Figure 4.10. The static stiffnesses for the vertical and horizontal vibration modes are calculated with Eqs. (4.16), (4.17) and (4.18).

$$K_z = \frac{2GL}{1-\nu}\left(0.73 + 1.54\chi^{0.75}\right) \tag{4.16}$$

$$K_y = \frac{2GL}{2-\nu}\left(2 + 2.5\chi^{0.85}\right) \tag{4.17}$$

$$K_x = K_y - \left(\frac{0.2}{0.75-\nu}\right)GL\left(1 - B/L\right) \tag{4.18}$$

in which G is the shear modulus, L is the length of the footing and ν is the Poisson ratio. χ is defined as $A_b/4L^2$. Since the mud mats have square geometries, stiffness in lateral direction, K_y, and longitudinal direction, K_x, are equal to each other.

Figure 4.10 provides graphs in which the dynamic spring coefficients for the vertical and horizontal (lateral) mode are plot validated for $0 \leq a_0 \leq 2$. a_0 is defined as the excitation frequency times breadth of the

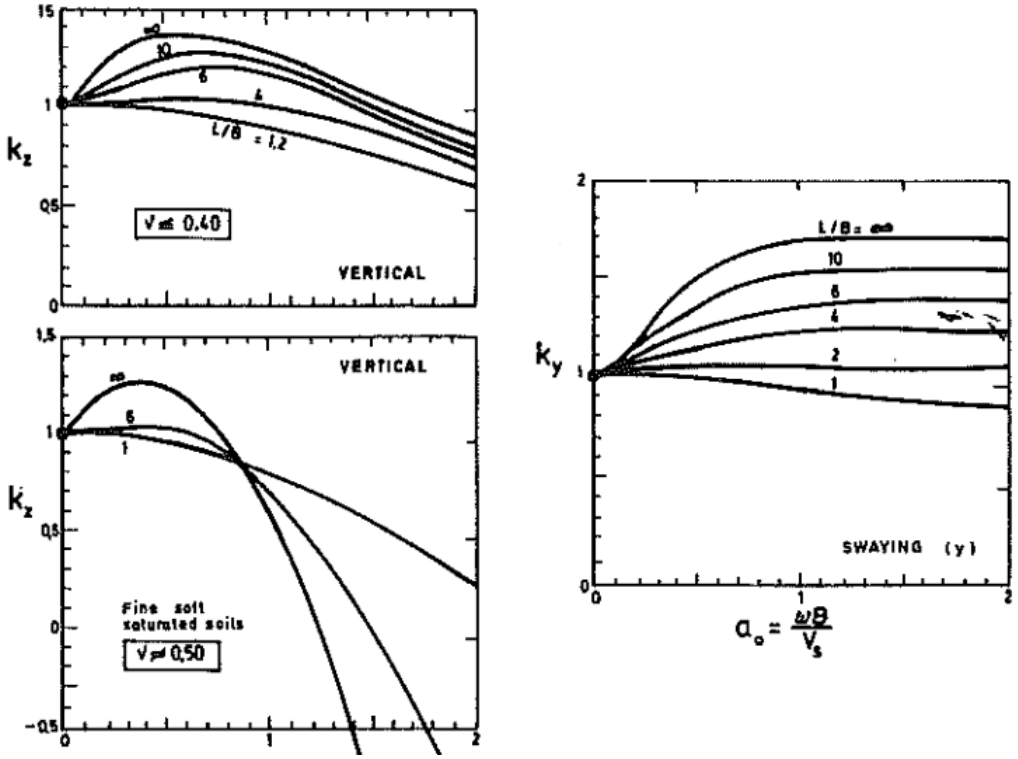

Figure 4.10: Dynamic spring coefficients for the vertical and horizontal (lateral) mode [11]

foundation divided by the shear wave velocity, $\omega B/V_s$. The figure shows the dependence of the vertical mode on the Poisson ratio. The horizontal mode is apparently not influenced by the level of the Poisson ratio. The shear wave velocity depends on the shear modulus and the density of the material and is calculated with Eq. (4.19).

$$V_s = \sqrt{\frac{G}{\rho}} \tag{4.19}$$

The density, ρ, is calculated as γ/g. Since no measurements are available of the shear modulus of the soil, the modulus is estimated. According to Look (2007), the undrained modulus of clay with an overconsolidation ratio between 4 and 10 and a plasticity index between 30-50 % equals E_u/c_u = 100 - 400. Since the plasticity index is mainly in the order of 30 % (Fig. 3.3), the undrained modulus is taken as $400c_u$ with a Poisson ratio of 0.5. Given the Young modulus, the shear modulus can be determined with Eq. (4.20).

$$G = \frac{E}{2(1+\nu)} \tag{4.20}$$

To use the approach presented by Gazetas, a circumscribed rectangle of width $2B$ and length $2L$, in which $L > B$, must be drawn in case of a non-rectangular geometry of the foundation. With the area, A_b, the area moments of inertia around the x-, y- and z-axes of the actual soil-foundation contact surface are calculated. The half-length and half-width of the circumscribed rectangle, L and B, can be determined while the shear wave modulus can be calculated as all input parameters are known. All parameters used to determine the spring stiffnesses for the different vibrations modes are given in a brief overview in Table 4.7.

The spring stiffnesses determined are divided by two as the equivalent model is supported by two vertical and two horizontal springs assuming that each spring in particular direction has equal stiffness. This assumption implies that the soil is uniform and therefore no spatial variation is considered in the shear modulus. However, this is an idealisation of reality in order to perform this simplified analysis. The vertical and horizontal static spring stiffnesses per spring are derived in the following equations.

Table 4.7: Input parameters to determine the spring stiffnesses for the dynamic analysis

Pre-piling template	
A_b	$835.6 \cdot 10^6 mm^2$
L	14454 mm
B	14454 mm
χ	1.0
Soil	
E_u	1.6 MPa
ν	0.5
G	0.533 MPa
ρ	1600 kg/m^3
V_s	18.25 m/s

$$K_z = \frac{2 \cdot 0.533 \cdot 14454}{1-0.5} \cdot \frac{0.73 + 1.54 \cdot 1^{0.75}}{2} = 34995 kN/m \tag{4.21}$$

$$K_h = \frac{2 \cdot 0.533 \cdot 14454}{2-0.5} \cdot \frac{2 + 2.5 \cdot 1^{0.85}}{2} = 23125 kN/m \tag{4.22}$$

Dynamic stiffnesses are determined by multiplying the static stiffnesses with the coefficients presented in the graph for fine soft soils with ν = 0.5 in Figure 4.10. As the soil stiffness is frequency dependent, the stiffnesses are computed for different periods. Table 4.8 provides an overview of the coefficients and dynamic stiffnesses, denoted with $\overline{K}$, belonging to the different frequencies.

Table 4.8: Dynamic stiffnesses for different periods

$T_p[s]$	a_0	k_z	k_h	$\overline{K_z}[kN/m]$	$\overline{K_h}[kN/m]$
2.5	2.008880179	0.31	0.85	10849.15067	19657.2181
3	1.674066816	0.42	0.87	14698.84929	20119.64233
4	1.255550112	0.68	0.9	23798.13695	20813.4231
5	1.00444009	0.78	0.92	27297.86297	21275.94361
6	0.837033408	0.88	0.95	30797.589	21969.72438
7	0.717457207	0.9	0.98	31497.5342	22663.50515
8	0.627775056	0.92	0.98	32197.4794	22663.50515
9	0.558022272	0.92	0.99	32197.4794	22894.7654
10	0.502220045	0.95	0.99	33247.39721	22894.7654
11	0.456563677	0.96	0.99	33597.36981	22894.7654
12	0.418516704	0.98	0.99	34297.31502	22894.7654
13	0.386323111	0.98	0.99	34297.31502	22894.7654
14	0.358728603	0.98	0.99	34297.31502	22894.7654
15	0.334813363	0.98	0.99	34297.31502	22894.7654
16	0.313887528	0.98	0.99	34297.31502	22894.7654
17	0.295423556	0.99	1	34647.28762	23126.02566
18	0.279011136	0.99	1	34647.28762	23126.02566
19	0.264326339	0.99	1	34647.28762	23126.02566
20	0.251110022	0.99	1	34647.28762	23126.02566
21	0.239152402	0.99	1	34647.28762	23126.02566
22	0.228281839	0.99	1	34647.28762	23126.02566
23	0.218356541	0.99	1	34647.28762	23126.02566
24	0.209258352	0.99	1	34647.28762	23126.02566
25	0.200888018	0.99	1	34647.28762	23126.02566

Table 4.8 provides the dynamic stiffness coefficients for peak periods varying from T_p = 2.5 up to 7 s. Gazetas verified the coefficients a_0 up to 2 which is obtained with a period of 2.5 s. It is found that the frequency

dependent stiffness are increasing with higher periods and therefore lower frequencies. After a period of 12 s, the stiffnesses remain almost equal for increasing periods.

Structure characteristics: natural periods

The pre-piling template is simplified to a model and the stiffnesses of the vertical and horizontal springs are derived. The vertical displacements of the template are denoted with x_1, the horizontal displacements is represented by x_2 and the rotation is given by x_3, all with respect to the neutral position of the centre of gravity of the template, which is assumed to be in the centre of the structure.

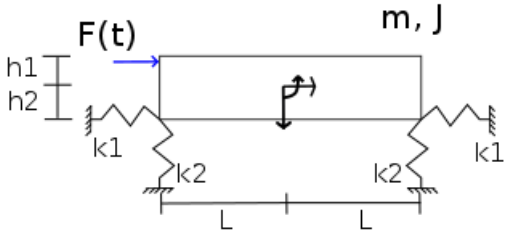

Figure 4.11: Idealisation of the reality to derive the equations of motion for this soil-structure interaction problem.

The equations of motion for the three degrees of freedom mass-spring system subjected to the hydrodynamic loading are given by Eqs. (4.23), (4.24) and (4.25).

$$m\frac{d^2x_1(t)}{dt^2} = m\cdot g - 2k_2x_1(t) \tag{4.23}$$

$$m\frac{d^2x_2(t)}{dt^2} = F(t) - 2k_1x_2(t) - 2k_1h_2x_3(t) \tag{4.24}$$

$$J\frac{d^2x_3(t)}{dt^2} = -F(t)\cdot(z+h_1) - 2k_1h_2x_2(t) - 2k_2l^2x_3(t) - 2k_1h_2^2x_3(t) \tag{4.25}$$

in which h_1 is the distance between the centre of gravity and location were the load enters the template, i.e. first contact point between pile and structure, the rollers. h_2 is distance between centre of gravity and mud mat and z is the distance between the reference point in which the integrated load over the pile acts and the roller. From the equations of motion, the mass and stiffness matrices are derived.

$$M = \begin{bmatrix} m & 0 & 0 \\ 0 & m & 0 \\ 0 & 0 & J \end{bmatrix}$$

$$K = \begin{bmatrix} 2k_2 & 0 & 0 \\ 0 & 2k_1 & 2k_1h_2 \\ 0 & 2k_1h_2 & 2k_1h_2^2 + 2k_2l^2 \end{bmatrix}$$

The program Maple, a powerful engine to solve complex mathematical problems both numerically and symbolically, is used to compute the natural periods during free vibrations taking into account the frequency dependence of the soil stiffness.

Table 4.9 presents the natural periods found in the analysis shown for the stiffnesses given in Table 4.8. For increasing spring stiffnesses is observed that the natural periods decrease and therefore the natural frequencies increase. As the stiffnesses become constant irrespective of the frequency since the dynamic stiffness coefficients tends towards 1 providing the static stiffness, the natural periods become frequency independent as well.

The shear modulus G incorporated in the stiffness is estimated based on a range of values provided in literature. As soil properties deviate spatially, an analysis is performed to see the effect of varying the shear

Table 4.9: Natural periods and normalised frequencies of the pre-piling template taking into account the frequency dependence of the soil stiffness

T_p	$T_{n1}[s]$	$T_{n2}[s]$	$T_{n3}[s]$	ω/ω_{n1}	ω/ω_{n2}	ω/ω_{n3}
2.5	22.0	14.3	26.46	8.80	5.72	10.58
3	18.90	13.83	23.25	6.30	4.61	7.75
4	14.85	19.52	12.72	3.71	4.88	3.18
5	13.87	18.71	12.26	2.77	3.74	2.45
6	13.06	18.01	11.80	2.18	3.0	1.97
7	12.91	17.77	11.64	1.84	2.54	1.66
8	12.77	17.68	11.57	1.60	2.21	1.46
9	12.77	17.63	11.55	1.42	1.96	1.28
10	12.57	17.51	11.44	1.26	1.75	1.14
11	12.50	17.47	11.41	1.14	1.59	1.04
12	12.37	17.39	11.34	1.03	1.45	0.95
13	12.37	17.39	11.34	0.95	1.34	0.87
14	12.37	17.39	11.34	0.88	1.24	0.81
15	12.37	17.39	11.34	0.82	1.16	0.76
16	12.37	17.39	11.34	0.77	1.09	0.71
17	12.31	17.30	11.29	0.72	1.01	0.66
18	12.31	17.30	11.29	0.68	0.96	0.63
19	12.31	17.30	11.29	0.65	0.91	0.59
20	12.31	17.30	11.29	0.62	0.87	0.56
21	12.31	17.30	11.29	0.59	0.82	0.54
22	12.31	17.30	11.29	0.56	0.78	0.51
23	12.31	17.30	11.29	0.54	0.75	0.49
24	12.31	17.30	11.29	0.51	0.72	0.47
25	12.31	17.30	11.29	0.49	0.69	0.45

modulus. A reduction in G results first in a reduction in the shear wave velocity leading to an increase in the dimensionless frequency factor since the shear wave velocity is in the denominator. As a_0 increases, the dynamic stiffness coefficients decreases implying a lower dynamic stiffness. Therefore, a reduction in shear modulus results in larger natural periods.

Comparison natural period with occurring load periods

An important aspect in dynamics is to ensure that during the design of a structure, the natural frequencies/periods are such that these will not coincide with the excitation frequencies/periods of the loading. In case that the natural frequencies do coincide, the system will start oscillating with greater amplitudes which is called resonance. The amount of natural frequencies depend on and is equal to the amount of degrees of freedom of the system. To visualise, an example of dynamic amplification factors against normalised frequencies of a 1-degree of freedom system are given in Figure 4.12. The dynamic amplification factor describes the magnification of the static displacements in case a dynamic loading is applied.

The wave periods are converted to circular frequencies, are normalised with the natural frequencies and are presented in Table 4.9 for the different frequency dependent stiffnesses. In case that normalised frequencies approach the value of 1, the situation becomes critical, magnification will occur and the structure will start vibrating heavily. It is found that peak periods from 9 s may already amplify the pre-piling template. Table 4.9 shows that for approximate periods of 11 s, 12 s and 17 s resonance will occur as ω/ω_n equals 1 which basically implies that these periods are the natural periods of the system. As mainly waves are observed with a period of 2 - 7 s, vibrations of the system will not be amplified. Reducing the shear modulus of soil increases the natural periods and thus decreases the natural frequencies. Therefore, the normalised frequencies will go down resulting in resonance for larger peak periods.

4.6. Summary and discussion

Theory is provided regarding the wave loads and its several components. An explanation is given on determining the wave loads on slender structures in which the inertia and drag components are highlighted. As the wave load is determined with the Morison Equation, a short review is given of the inertia and drag coeffi-

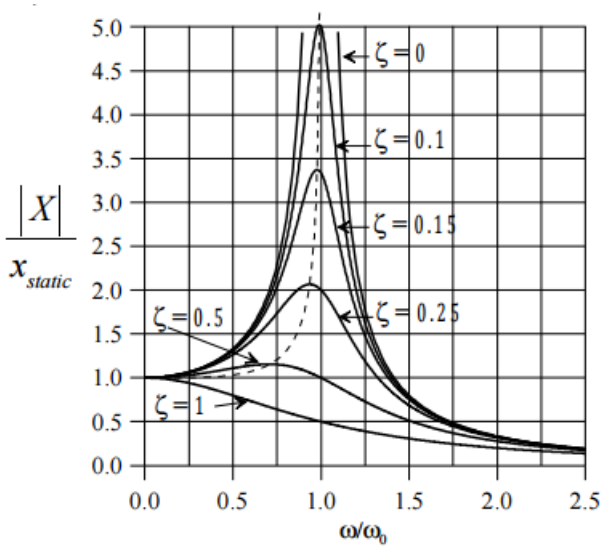

Figure 4.12: Example of dynamic amplification factors for different normalised frequencies of a 1-DOF system

cients proposed by different studies and guidelines. In this study, well-known coefficients of C_M = 2.0 and C_D = 1.2 proposed by DNV are chosen as the load is inertia dominated.

The velocity profile of the current and wind is described by the idealised $1/7^{th}$ power law. The current velocity is added to the wave particle velocity providing the total drag load. The drag component due to the wind is added as a constant load but is not expected to interfere the operations as it has a relatively small contribution to the total load.

Two load cases are determined based on the main wave directions. Its characteristics, $H_s; T_p; U_{10}$, are determined with scatter plots from 14 years data set. The loads are determined for different pile combinations showing that when the wave length is in phase with the distance between the piles greater loads can be achieved with less piles. Assuming the pre-piling template with piles acting as one rigid body, the loads can be decoupled over the mud mats. The hydrodynamic loading is assumed to be quasi-static and therefore slow enough to disregard inertial effects. As the loading is harmonic, the mud mats are examined with the maximum occurring load the soil has to bear. Although it remains for a short period, it is believed that the soil provides an immediate response to the loading.

The loads acting on the system are uniformly distributed to the mud mats with a push-pull mechanism whereupon these are transferred to the subsoil. As moment loading induces an angular rotation of the pre-piling template, the stresses beneath the mud mats are believed not to be uniformly distributed but having a triangular stress distribution expecting that the intermediate mud mats may help in the load transfer as well. This is verified for diagonal loading case. The contribution was rather small and is therefore neglected. The stress distribution beneath the mud mats is assumed to be uniform. However, the importance of the difference between both mechanism is still unknown.

To justify the quasi-static character of the loading, a dynamic analysis is performed. An equivalent square structure is derived with equal mass and mass moment of inertia properties. Frequency dependent spring stiffnesses are estimated from expressions given in literature which are given for footings on a homogeneous half-space. With the dynamic stiffnesses for the vertical and horizontal mode, the system is analysed for free vibrations showing that the natural periods of the structure are higher than the excitation periods which are measured in the field implying that resonance will not occur. A parametric study showed that decreasing the shear modulus resulted in the decrease of dynamic stiffness and natural frequency and therefore in an increase of the natural period causing resonance for larger periods. Based upon this simplified analysis, the load may assumed to be quasi-static.

5

Assessment of the bearing capacity of a single clay layer

The Wikinger pre-piling template is positioned at the seabed and is subsequently preloaded in order to create a safe working platform. After finishing this operation, the piles are stabbed individually whereupon the pile driving operation may start. As soon as the piles are placed in the sleeves, they are subjected to environmental loading. The loads are transmitted via the piles and the template to the subsoil. An analysis has to be performed for the investigation of possible soil failure and thus settlements and which conditions triggers the failure of soil.

A brief recap is given about the load cases and corresponding loads. Interaction diagrams are presented which are required for the bearing capacity assessment. Subsequently, the effect of considering different pile combinations stabbed and the effect of changing the operational limits are presented.

5.1. Environmental loading

Two load cases are determined based on measurements conducted in the project area. The first load case consists of horizontal loading of the system while the second load case incorporates diagonal loading in which a single mud mat is fully in compression/relaxation. Based on the data, scatter diagrams are constructed used to derive the main parameters (H_s, T_p, U_{10}) to determine the operational limits of the load cases.

The total hydrodynamic load acting on the piles and template is calculated with the Morison Equation, Eq. (4.10). Extensive research is performed on the coefficients for inertia and drag loading. In this study, C_m = 2.0 and C_D = 1.2, proposed by DNV, are incorporated as these are widely used. The wave and current velocities, described by the idealised $1/7^{th}$ power law, are superposed prior to the calculation. The wind load is assumed to sustain continuously over time and is therefore simply added to the hydrodynamic load as a constant load. The contribution of the wind to the total environmental load is rather small as only a small part of the piles and the hammer is subjected to wind.

Given the load components, the total loading is calculated in steps of 0.1 seconds. For the horizontal load case, a horizontal load F_x = 65.58 t and a moment loading of M_y of 1910.09 tm is found. The critical loading during the second load case consists of F_x = 33.76 t and M_y = 1143.84 tm.

5.2. V-H interaction diagrams - analytical assessment

The capacities are presented in terms of failure envelopes which are nowadays more and more accepted. This approach allows for an explicit consideration of the individual load components in horizontal, vertical and rotational direction. The envelopes show all combinations of loads for which plastic deformation occurs. Loads falling within the envelope will cause solely elastic deformations. In this study is chosen to describe the capacities first in the two-dimensional V-H loading space in which the moment loading is decoupled over the mud mats. The failure envelopes assume uniformly distributed loads over the area.

ISO 19901-4 provides different recommendations for different situations and geometries to determine the interaction diagrams. For square surface footings on soil with uniform soil strength, Eq. 2.31 provided by Gourvenec (2007) is recommended. Gourvenec derived this expression from the exact solution for a strip footing which is fully bonded to the soil. On the contrary, the given expression is applicable to footings not able to sustain tension. For comparison, the expression given by Gourvenec is compared to its origin (Eq. (2.30)).

Figure 5.1 shows the V-H interaction diagrams according to ISO 19901-4 and Green (1954). The diagrams are given in normalised space to provide the shape of the envelopes and to leave out the discrepancies in the ultimate horizontal and vertical capacities.

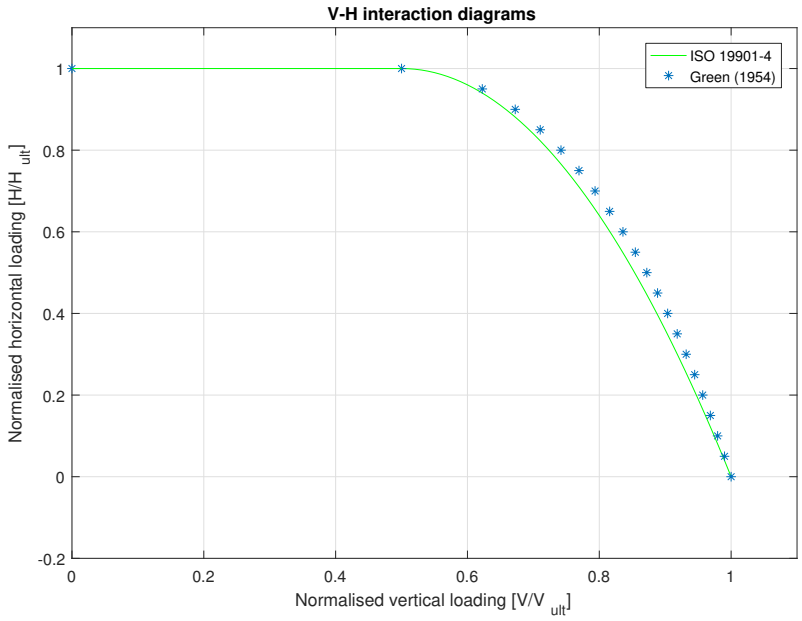

Figure 5.1: Shapes of V-H interaction diagrams in normalised space proposed by Green (1954) (Strip) & Gourvenec (2007) (Square)

The shape of the failure envelopes remains flat up to v = 0.5 for both expressions. This basically means that the vertical loading does not have any effect until this threshold and failure consist of a purely sliding mechanism. During the transition to a combined sliding and bearing failure mechanism, the expression proposed by Gourvenec falls slightly within the envelope proposed by Green. From this point, the vertical capacity starts becoming important up to purely vertical failure producing a Prandtl failure mechanism.

To obtain the interaction diagram in normal V-H loading plane, the shapes of the envelopes have to be multiplied with the ultimate horizontal and vertical bearing capacities calculated with Eqs. (2.7) and (2.8). The parameters used to determine the ultimate capacities are given in Table 5.1. Holocene deposits are characterised as Tresca soil, therefore φ is chosen to be 0. An adhesion factor of 0.75 is incorporated by the recommendation of Littleton (1976). The modification factors for the inclination of the loading, the shape of footing and the embedment are taken according to ISO 19901-4 with Eqs. (2.25), (2.12) and (2.17), respectively.

Figure 5.2 shows the capacities in horizontal and vertical loading space for a single mud mat derived according to ISO 19901-4 and Green (1954). Additional vertical capacity due to kinematic constraints is possible in case the failure mechanism beneath the individual footings of the template would prevent each other from

Table 5.1: Overview of parameters used to determine the V-H interaction diagrams of square surface footings placed at homogeneous soil

Pre-piling template	
A	50.97 m^2
L	7.14 m
B	7.14 m
Soil	
s_u	4 kPa
φ	0 °
K_p	1
γ'	5.7 kN/m^3
α	0.75
Bearing capacity	
N_{cV}	$2+\pi$
N_{cH}	1
i_c	0
s_c	0.18
d_c	0

developing. As the footings are placed more than one times the breadth from each other, the mechanisms are able to develop and therefore no additional vertical capacity can be taken into account. The bearing capacity for the total pre-piling template equals therefore four times the capacity of a single mud mat.

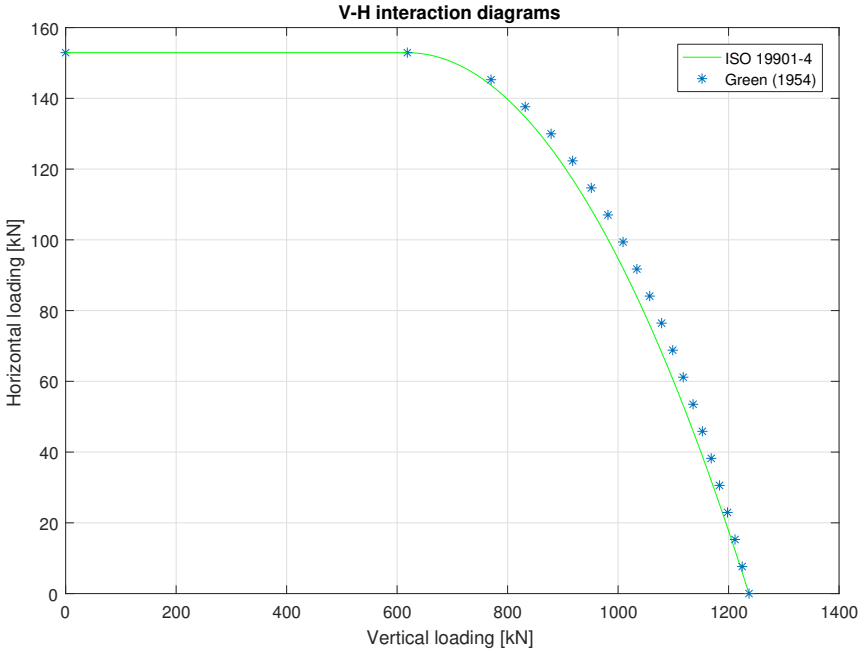

Figure 5.2: V-H interaction diagram for a single surface square mud mat

The next installation step is the preloading phase of the template. By preloading soil is brought to failure in order to achieve higher bearing capacities and thus a safer working platform. This is shown in the interaction diagrams as an expansion of the locus in which the pure vertical capacity equals to the applied preload. The settlement can be calculated with Eq. (2.7) since the ultimate vertical bearing capacity and all other input parameters are known. Settlement stops after the equilibrium between the load and capacity is recovered. Therefore, the settlement is back calculated by solving the term d in the equation and is found to be 0.20 m with the application of a preload of 25.6 kPa.

As soon as preloading starts, footings become embedded resulting in the influence of the surcharge term and depth effects. These cause an increase in the vertical bearing capacity, while the horizontal capacity is enhanced since soil in contact with the sidewalls is mobilised during sliding providing additional resistance.

A significant amount of research is performed to capture the bearing capacities of different geometries in various conditions during combined loading as nicely as possible. Various studies have been performed to propose factors taking into the account for example the shape or embedment of a footing. Therefore, the failure envelope according to ISO 19901-4 is compared to a failure envelope of which the modification factors are found in different numerical studies. The shape and depth factors provided by Gourvenec are considered, Eqs. (2.13) and (2.19), respectively. The horizontal capacity is determined according to Bransby & Randolph, which proposed a bearing capacity factor for the horizontal capacity for strip footings fully bonded on the soil, Eq. (2.20).

Figure 5.3 provides the envelopes for ISO 19901-4 and the other studies. Good agreement is found between both envelopes implying that for this study, the semi-empirical factors recommended by ISO 19901-4 are useful describing the capacities in V-H loading space. The slight overestimation of the envelope results due to overestimation in horizontal capacity, initially not derived for square footings with ZTI. The great increase in horizontal capacity for embedded footings arises as adhesion is only influential when the footings are positioned at the subsoil. The horizontal capacity is factored with the adhesion factor lowering the ultimate horizontal and therefore the combined horizontal - vertical capacities as well.

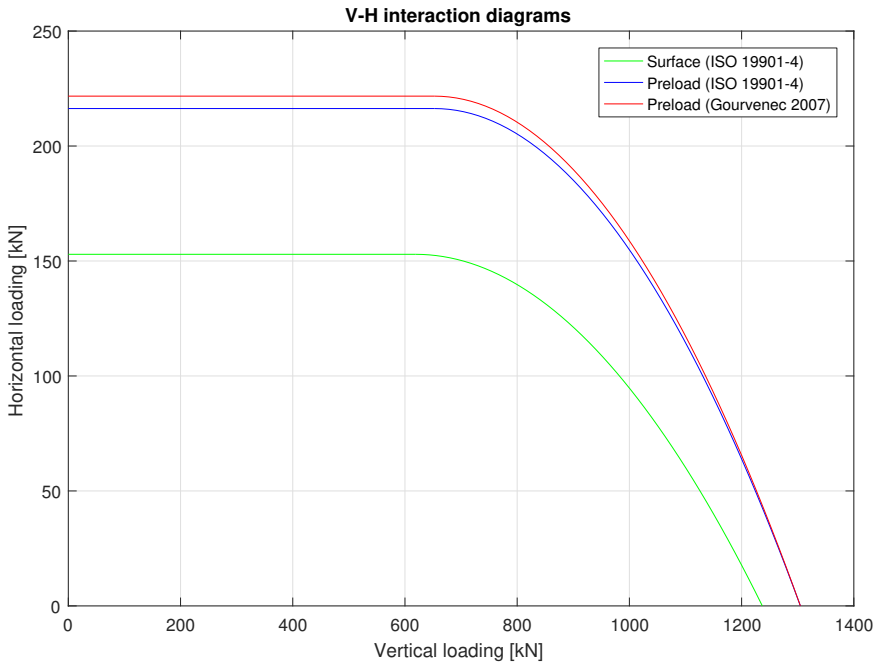

Figure 5.3: V-H interaction diagrams for a single surface and embedded square mud mat

5.3. Horizontal load case LC1

Comparing the loads with the failure envelopes, an assessment is performed on possible soil failure during specific loading conditions. During the horizontal loading case, two footings are equally responsible for the load transfer. The loads and corresponding loads for a single mud mat are plot in Figure 5.4. The loads for the different pile combinations are given in Table 4.3.

Figure 5.4 shows the bearing capacity at seabed to be sufficient for a single pile or two piles at fore and aft. With preloading, additional capacities are created and since adhesion loses its influence, sufficient capacities are created to cope with loads arising from three piles. Failure occurs when all piles are placed in the template resulting in the expansion of the failure envelopes.

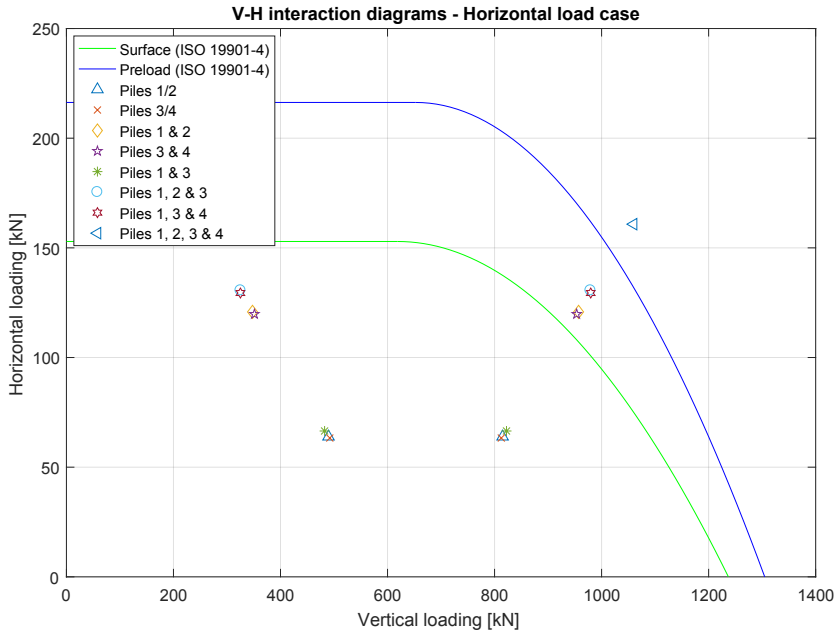

Figure 5.4: Loads of LC1 on a single mud mat plot within the interaction diagrams for a mud mat at surface and after preloading.

The chosen operational limits in the first load case result in an settlement of 0.40 m calculated with Eq. (2.7). As the settlements are lower than 0.80 m, the situation is not considered to be critical. The template is able to recover its alignment and therefore the pile driving operation can be proceeded without any disturbance due to the soft clay layer. As waves occur in with wave heights and peak periods, the effect of changing the operational limits on the operability is investigated for the limits considered in this study.

Effect changing operational limits

Waves are highly non-linear but are assumed for simplicity to be a superposition of all kind of linear waves with different wave heights and peak periods. Therefore it is important to know what happens with the soil when these different wave heights and periods occur. Sea states might occur which make the settlements uncontrollable anymore. In case settlements approach the critical value of 0.80 m, the operational limits have to be reduced such that the pre-piling template does not settle anymore. Modifying the operational limits and the level of required preload are possible solutions to tackle the problem. Figure 5.5 shows the envelopes in which the pre-piling template is at subsurface and after preloaded. The compressive loads acting on a single mud mat for wave heights varying from 0.25 up to 2.25 m and peak periods from 2 to 7 seconds are plot within the figure assuming that all four piles are stabbed in the pre-piling template.

The current conditions shows that sufficient capacity is created to bear the loads from waves within the given limits except for the operational limits chosen in the horizontal load case and for waves higher than 1.25 m with a peak period of 4 s is local instability beneath the footing observed. A peak period of 4 seconds corresponds to a wave length of 25 m which approximately equals the pile center-to-center distance which is 23 m. This results in the amplification of the occurring loads and therefore in the exceedance of the failure envelope. In the total data set, less than 2 % of the waves are higher than 1.25 m with a T_p of 4 seconds and therefore, the possible occurrence is rather small.

5.4. Diagonal load case LC2

The second load case consists of diagonal loading in which a single mud mat takes the compression loads while the other mud mat on the diagonal is in relaxation. The contribution of the intermediate mud mats to the load transfer is shown to be rather small in Table 4.6. Figure 5.6 shows the loads acting on the mud mats and the envelopes at surface and after preloading.

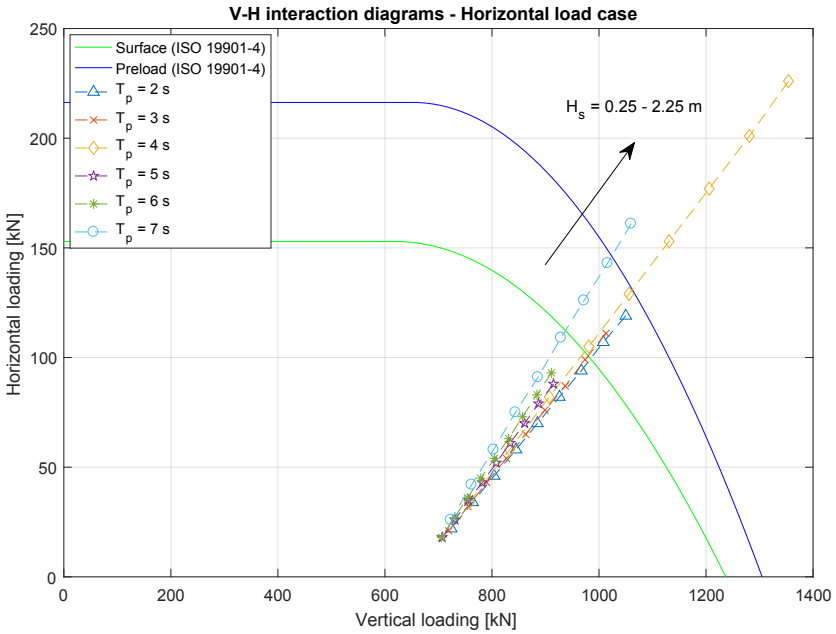

Figure 5.5: Local stability check of a single mud mat in compression for H_S = 0.25 - 2.25 and T_p = 2 - 7 s with V-H interaction diagrams at surface, after preload and after failure in horizontal load case

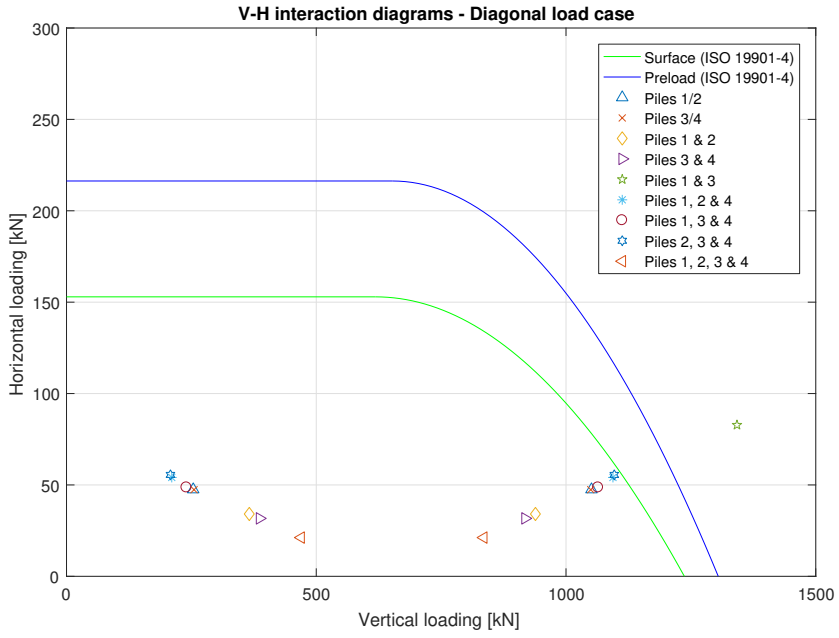

Figure 5.6: Loads for different pile combinations in diagonal load case with interaction diagrams in case of a surface footing and after preloading

Preloading enables the soil to deal with loads arising from all pile combinations except pile combination 1 and 3. Sufficient bearing capacity is present even without preloading. As the loads exceed the capacities, the envelope will start expanding until the equilibrium is recovered. The mud mat of the pre-piling template is found to settle 0.72 m, which starts to approach a critical situation if any further settlement occurs.

Effect changing operational limits

The effect of changing the operational conditions on the local stability of the mud mat is assessed for the diagonal loading case. Compressive loads acting on the mud mat are determined for H_s varying from 0.25 to 2.25 m and T_p from 2 up to 7 s and are presented together with the interaction diagrams. The graphs show that failure does not specially occur prior to the piling operation when four piles are stabbed. Figure 5.7 shows for instance that more sea states are present causing operational difficulties with the on-bottom stability of the pre-piling template. In case piles 1 and 3 are stabbed in the template, waves slightly higher than 1.25 m irrespective of the peak period may result in difficulties.

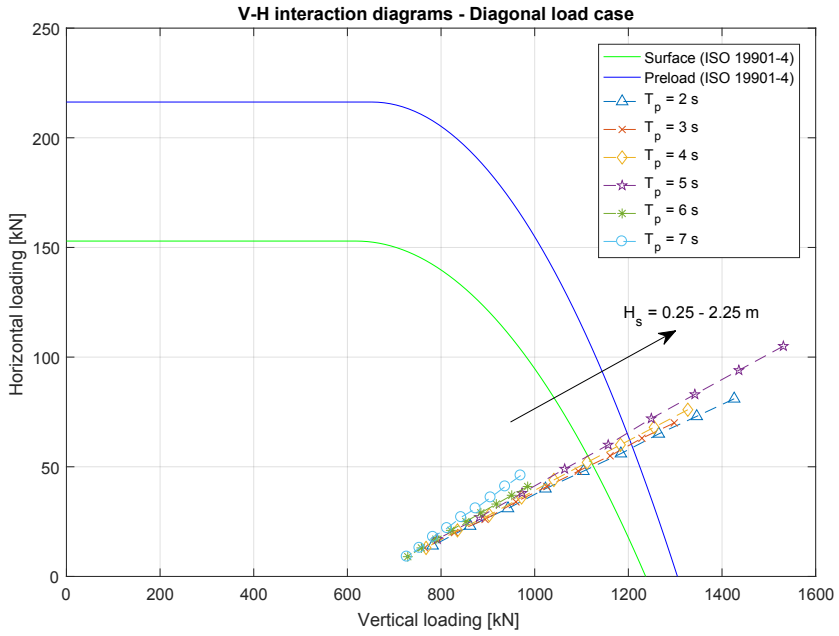

Figure 5.7: Local stability check of a single mud mat in compression for H_S = 0.25 - 2.25 and T_p = 2 - 7 s with V-H interaction diagrams at surface, after preload and after failure in diagonal load case

Failure seems to occur for different sea states with different pile combinations as well. Loads corresponding to waves at two, three or four piles placed in the template may cause failure. The effect of changing the operational limits for different pile combinations is provided in Appendix D. The operation of positioning the template and performing the installation can be safely executed for waves higher than approximately 0.9 m regardless of the peak periods between 2 and 7 s showing that the diagonal loading case is the most critical case.

5.5. V-H interaction diagrams - numerical assessment

Section 5.2 provided an assessment of the bearing capacity assuming a single mud mat on soft clay layer with uniform over depth. The capacities were derived according to the recommendations of ISO 19901-4 providing recommendations for specific geometries. This section provides a numerical assessment of the bearing capacity of a single square footing to verify the recommendations of the guideline for this specific case.

The software package Plaxis 3D is used to perform three-dimensional finite element calculations. In the following, the finite element model used in the analysis is explained. An elaboration is given on the chosen constitutive soil model followed by a mesh dependency study. The obtained interaction diagrams are presented in V-H loading plane whereupon a comparison is provided between the recommendation by ISO 19901-4 and the results of this study.

Finite element model

The situation concerning the Wikinger pre-piling template is a three-dimensional problem and may not be simplified to a two-dimensional problem. Symmetry is taken around the y-axes with elements containing 10 nodes. Double symmetry is not considered since the failure mechanism during combined loading is not symmetric as failure in the +H+M plane has a different failure mechanism than in the -H+M plane. Assuming double symmetry would therefore lead to an incorrect assessment of the stability. The boundaries of the model are determined as four times the breadth from the origin in the all directions.

A Mohr-Coulomb soil model is used as constitutive model since it is a well-known linear elastic perfectly plastic model used to obtain a first approximation of the soil behaviour including the bearing capacities of the soil. The elastic part is based on Hookes law of isotropic elasticity, while the plastic part is described using the Mohr-Coulomb failure criterion. The model is often used by engineers for its simplicity as it overlooks the non-linear and complex behaviour of soils. Phenomena as hardening or softening are not captured within this model and therefore the model has to be used carefully, especially when soils with undrained characteristics are involved. For this study, involvement of complex soil behaviour as hardening/softening is not required and therefore a Mohr-Coulomb model is considered sufficient.

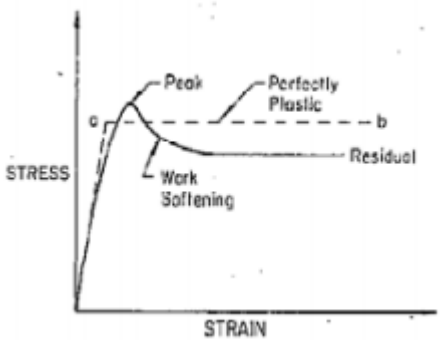

Figure 5.8: Linear elastic perfectly plastic assumption within the Mohr-Coulomb soil model

Footing

Mud mats are often much stiffer and stronger compared to the soil on which they are resting. When internal forces and deformations are not relevant to the problem, footings may be modelled as rigid bodies, which are able to translate and rotate, but not able to deform [25]. The mats are therefore modelled as rigid bodies since the main interest lies in the stresses beneath the footing. The contact stresses between the mud mats and soil are modelled properly by including interface elements.

The American Petroleum Institute (API) suggests that during undrained analysis engineering judgement is required to determine whether suctions will be generated and the duration over which they can be maintained. The interface between the mud mats and the soil is modelled as an interface not able to sustain tension, i.e. tension cut-off is enabled within Plaxis 3D. The mud mats are not deployed with skirts which usually enables the development of suction. The mud mats contain holes with plungers allowing water to enter beneath the mud mats to minimise the suction and therefore to facilitate the retraction of the template. Therefore, the decision to incorporate a zero-tension interface is found appropriate.

Mesh

The mesh used in this analysis is shown in Figure 5.9d. A refinement has been applied beneath the footings for more accurate results without adding unnecessary calculation time by refining the entire mesh. The boundaries are chosen such that the displacements and strains are captured by the refinement. Additional nodes, i.e. interface elements, are defined between the footing and soil in order to capture the interaction in a proper way.

Mesh dependency

The results from finite element analysis are dependent on the smoothness of the mesh. To examine this dependency, a mesh dependency study is performed considering both the ultimate vertical and horizontal capacities. Mesh configuration with 95064 elements and 138825 nodes is founded to be well suited to describe

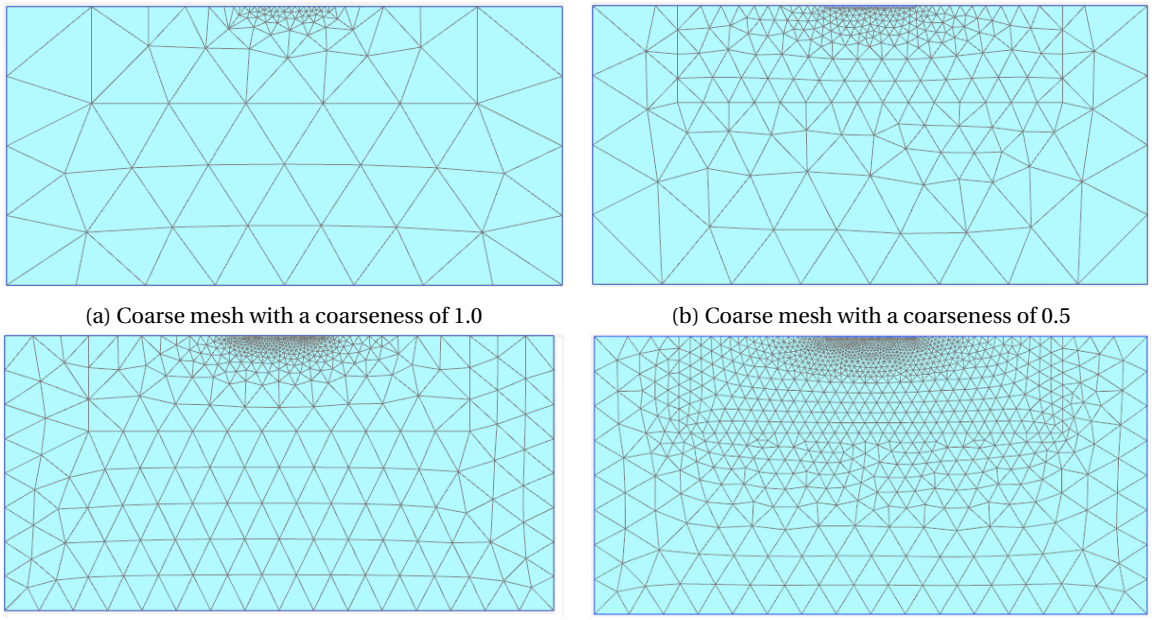

(a) Coarse mesh with a coarseness of 1.0

(b) Coarse mesh with a coarseness of 0.5

(c) Fine mesh with a coarseness of 1.0

(d) Fine mesh with a coarseness of 0.5

Figure 5.9: Mesh dependency study

the bearing capacities within acceptable limits as a difference of 4.9 % is obtained in the vertical capacity compared to the theoretical bearing capacity factor for square footings [16]. Increasing refinement of the mesh resulted in 392528 elements and 535757. In order to run the models with this mesh configuration would drastically increase the computation time and therefore this mesh configuration is disregarded from the mesh dependency study.

Table 5.2: Mesh dependency of the ultimate vertical and horizontal capacities

Number of elements	Number of nodes	V_{ult}/As_u	H_{ult}/As_u
3866	6659	6.91	1.0
11790	18806	6.59	1.0
35169	53068	6.34	1.0
95064	138825	6.20	1.0

Table 5.2 shows the convergence of the ultimate vertical capacity with increasing elements to the theoretical bearing capacity factor of a square footing, $V/As_u = 5.91$ [16]. The horizontal capacity equals the theoretical solution of 1.0 for every mesh configuration due to the incorporating of the interface between the soil and the footing.

The decrease in ultimate vertical capacity with increasing amount of elements can be explained with its failure mechanism. During pure vertical loading, a Prandtl failure mechanism is generated which is felt quite deep. Sliding results only in straining and thus soil mobilisation near the subsurface. The extent in which vertical loading causes strains in the soil is larger as well compared to horizontal loading. During pure vertical loading, plastic strains are generated up to 0.4 times the width of the foundation. With pure horizontal loading, soil direct beneath the footing is mobilised up to 0.15B. By increasing number of elements, the area with smaller and finer elements is able to capture the failure mechanism more smoothly resulting in the convergence of the numerical bearing capacity factor.

Displacement controlled

Constant displacement controlled probe tests are carried out to analyse the limit states of combined loading on the pre-piling template. Using displacement controlled probes rather than load controlled enables one to

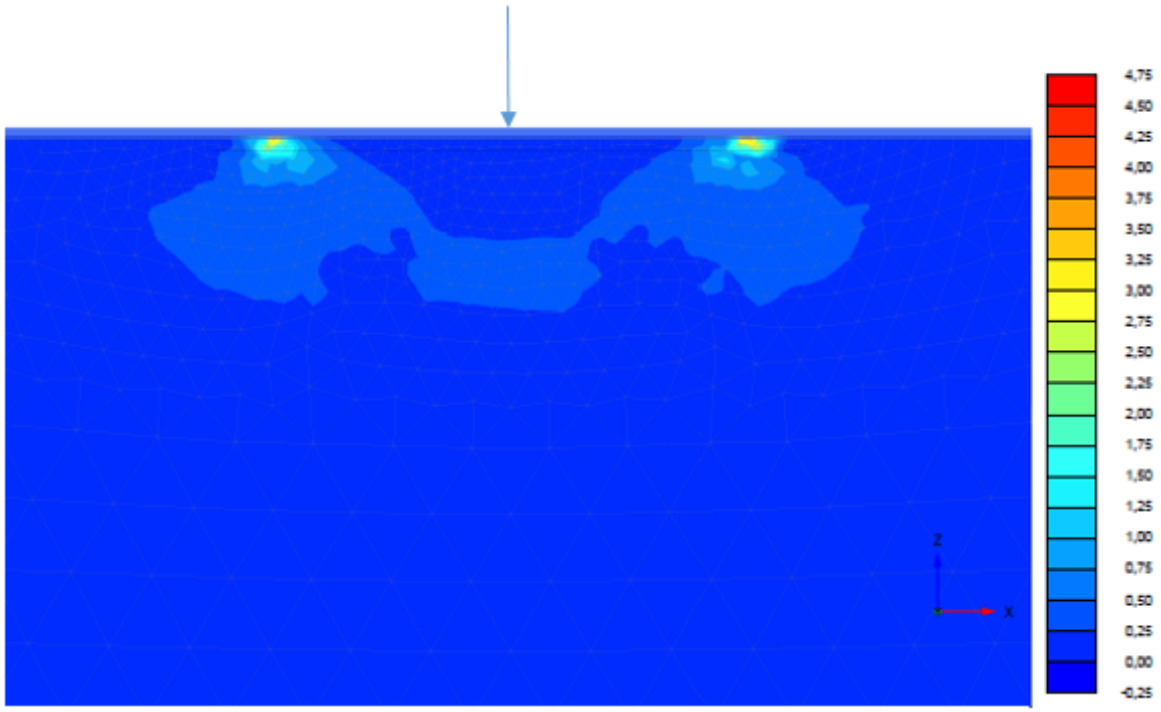

(a) Plastic strains during pure vertical loading [-]

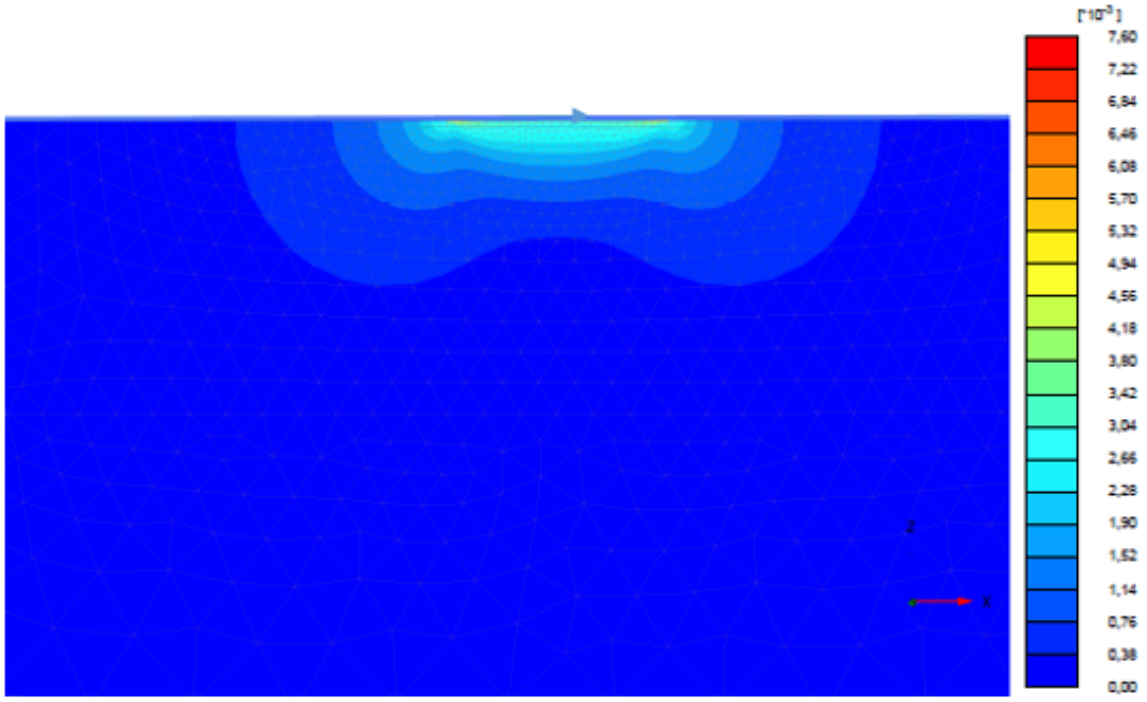

(b) Plastic strains during pure horizontal loading [-]

Figure 5.10: Plastic strains after failure during pure vertical and horizontal loading

observe post-failure conditions. This method is implemented successfully by Gourvenec (2007).

To derive the failure envelopes, many individual calculations are required. Different load combinations are considered within the analysis. In the V-H loading space, 8 different combinations of normalised dis-

placements (u/w) are considered besides pure horizontal and vertical displacements. For the V-H-M loading space, 13 different probes (u/θ) are carried out under constant vertical load, which are used to construct the envelope initially in the three-dimensional loading space in a two-dimensional graph.

5.6. V-H capacity diagram

Many expressions are provided in literature to approximate the ultimate limit states of footings. Guidelines such as ISO 19901-4 provides different papers to be used for the failure envelope approach. As these hold for certain limited conditions, studies are carried out to expand the range of possible solutions by investigating a specific, still not established, aspect.

This section provides a comparison between the V-H interaction diagrams derived according to ISO 19901-4 and this study. In the comparison is assessed whether ISO 19901-4 provides proper estimations for square mud mats on soft soils. Envelopes derived by Feng et al. (2014) are included as well. Figure 5.11 presents the failure envelopes for a square footing placed on surface of soft clay with uniform strength over depth according to ISO 19901-4, Plaxis 3D and Feng et al. Data points obtained from Plaxis 3D are used to fit a curve with Eq. (2.28) through these points providing the failure envelope.

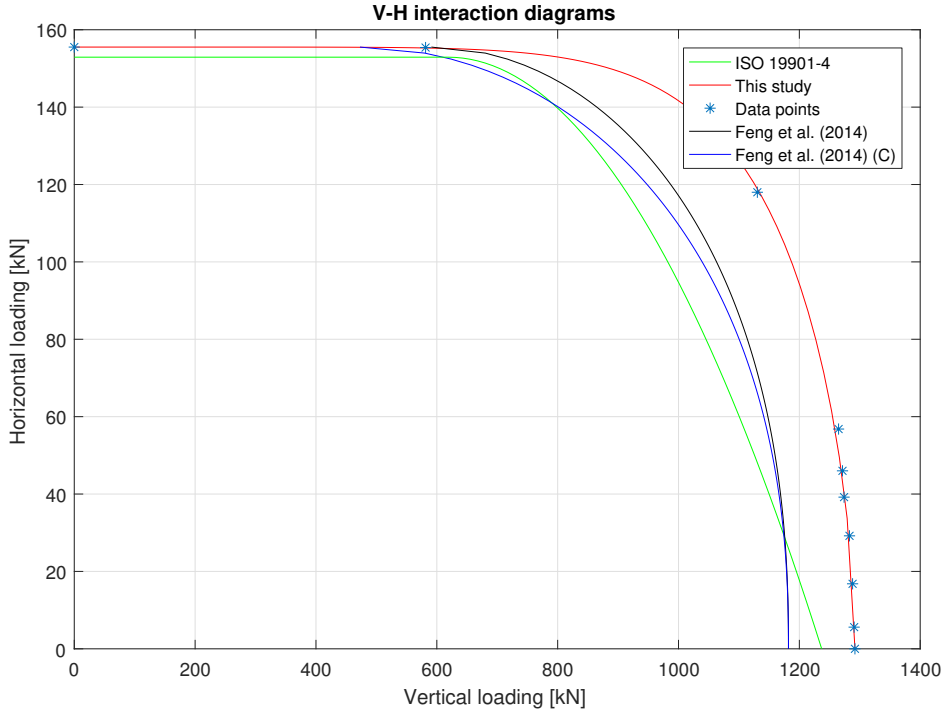

Figure 5.11: Comparison of V-H interaction diagrams derived according to literature and this study

The envelopes show good agreement on the ultimate horizontal capacity with a difference of only 1.5 % between ISO 19901-4 and Plaxis 3D. The horizontal capacity is found exactly the same as the numerical results presented by Feng et al. The ultimate vertical capacities provide a larger difference for the different methods. ISO underestimates the capacity with 4.5 % compared to Plaxis, which can be contributed to the inaccuracy of the finite element model due to the mesh configuration. The difference with Feng et al. is even greater with a difference of approximately 10 %. This difference seems to be preserved during combined vertical and horizontal loading until the sliding failure mechanism starts to be dominant. The variation compared to ISO keeps increasing and is largest during combined loading. To investigate the actual difference in the shape, the discrepancies in the ultimate capacities are matched out by normalising the envelopes with respect to its ultimate capacities as shown in Figure 5.12.

The curves in normalised space show a smaller difference in shape. However, there is still a significant difference in the shape recommended by ISO. Figure 5.12 shows that this recommendation is underestimating the capacities in V-H loading plane since the expression suggested by Gourvenec (2007) is a parabola shaped

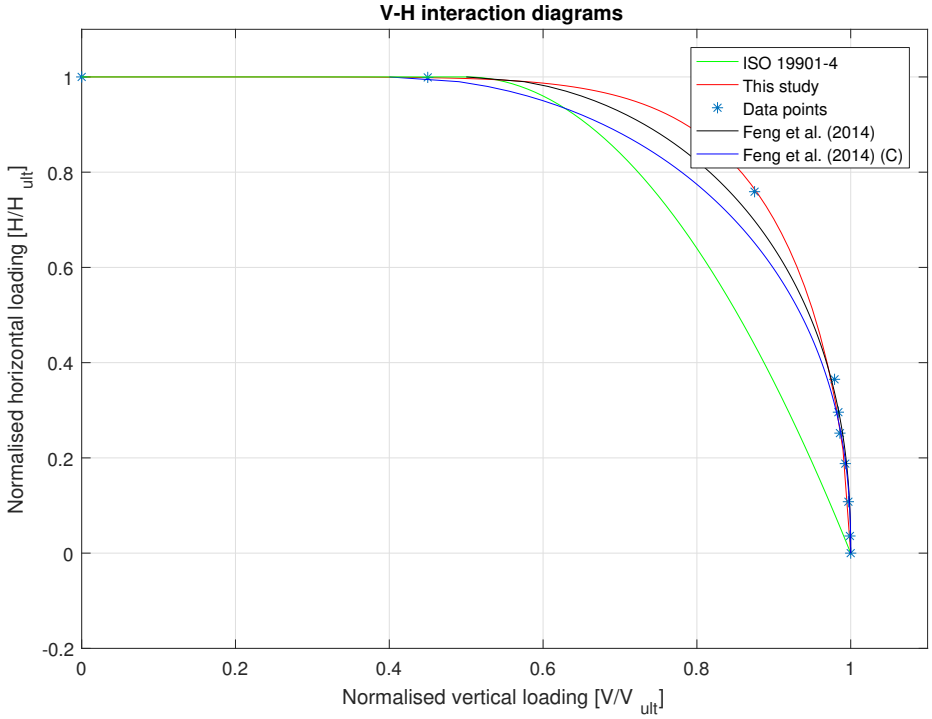

Figure 5.12: V-H interaction diagrams presented in normalised loading space

equation. In the numerical calculation, a ellipse shaped equation is found to suit the data output properly providing the large difference between both methods.

The normalised envelope found in this study seems to be more similar to the envelopes derived by Feng et al., especially to the expression which was originally derived, Eq. (2.33). Sliding starts to become important for $V/V_{ult} < 0.5$ for all shapes except for the compensated fit at which sliding occurs for all vertical loads smaller than $V/V_{ult} < 0.4$. During combined vertical and horizontal loading a small underestimation in capacity is observed, which might arise since the expressions were originally presented for rectangular footings. A sensitivity study is performed showing that the expressions might be applicable to square footings as well. Feng et al. modelled the footing as a rigid body, rough in shear and fully bonded to the soil. The side walls of the mud mat were considered as frictionless and detachment with the soil was allowed by assigning a zero-tension interface. The footing modelled in this study was a rigid body and rough in shear as well. However, the bottom interface was also assigned a zero-tension condition. The differences in the way of modelling may caused the slight difference between both shapes. Overall seen, good agreement between both expressions is found and therefore Eq. (5.1) may be used to describe the capacities of a square footing in the conditions considered in this study.

$$\left(\frac{H}{H_{ult}}\right)^{1.719} + \left(\frac{V}{V_{ult}}\right)^{7.449} = 1 \tag{5.1}$$

To see the difference in allowable operational limits, the loads for the critical peak periods causing settlements are plot in Figures 5.13 and 5.14 with the capacities derived by both ISO 19901-4 and this study for the horizontal and diagonal load case.

Figure 5.13 provides that the peak periods 4 and 7 seconds remain critical in the horizontal loading case. Compared to ISO 19901-4, there is sufficient capacity for 0.25 m up to 0.50 m higher waves, while for other peak periods, the soil is able to deal with the waves up to 2.25 m. Translating this to the occurrence of waves in the field shows that up to 8 % more waves are covered of the total data set. In the diagonal load case, the soil may cope with significant higher waves as well. For peak periods of 3 and 4 seconds, wave heights up to 2.0 m can be sustained while for $T_p = 5$ s waves up to 1.50 m can be dealt with. This results in up to 16 % more coverage of the waves measured in the field.

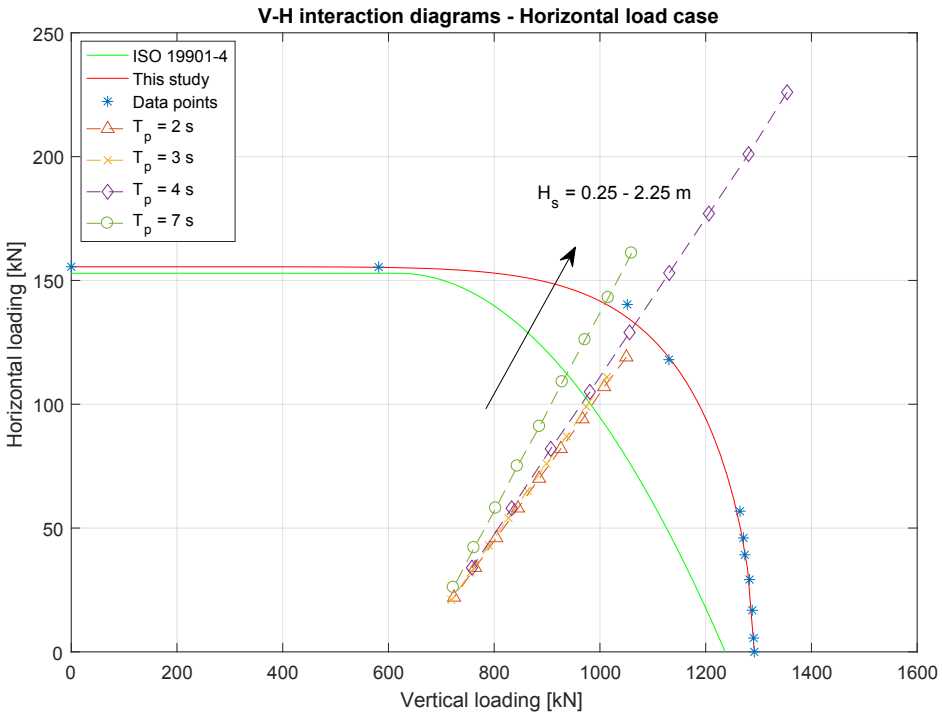

Figure 5.13: V-H interaction diagrams with the critical loads in the horizontal loading case

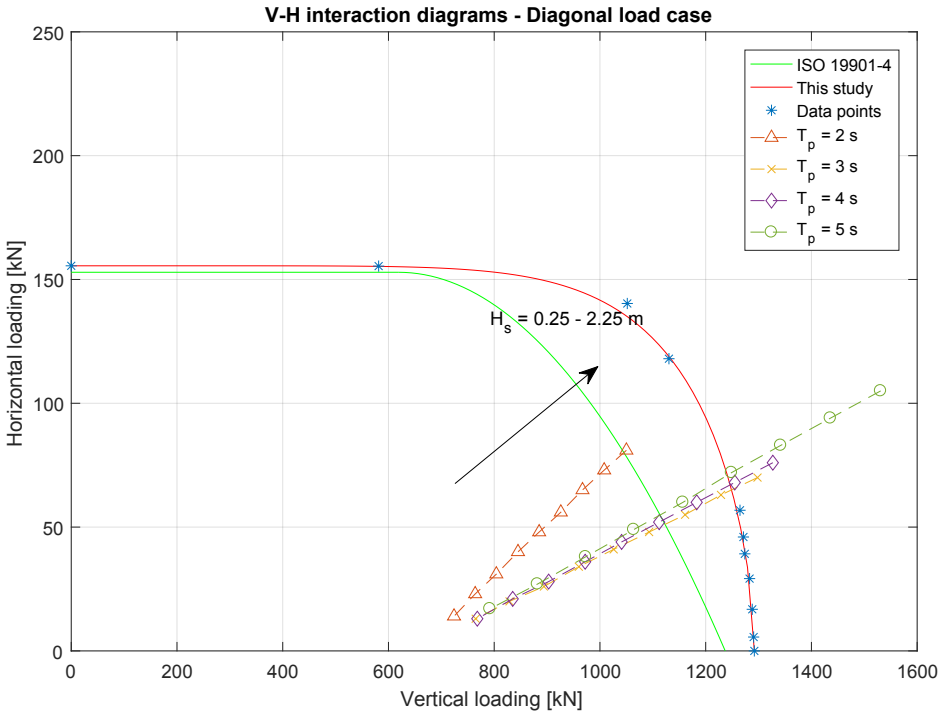

Figure 5.14: V-H interaction diagrams with the critical loads in the diagonal loading case

5.7. Summary and discussion

This chapter provides an assessment of the bearing capacity of a single clay layer with uniform strength. The capacities are given in V-H loading space according the recommendations of ISO 19901-4. ISO provides a shape to approximate the capacities of a square footing containing a zero-tension interface at the base. A comparison is made with the shape for strip footings given by Green (1954). Subsequently, the capacities are given for the surface footing and after preloading resulting in an increase in both vertical and horizontal capacities. The increase of capacities is fully attributable to boundary effects (depth effects, surcharge) as uniform strength over depth is chosen rather than linearly increasing strength and as adhesion becomes less influential at depth.

Loads are plot together with the failure envelopes for different pile combinations for the assessment of the preload. It is shown that for the horizontal load case, the level of preload seems not to be sufficient as sea states are present causing settlements. The increase in capacity, shown as an expansion of the diagram, covers up to 8 % more waves of the total data set. For the diagonal loading pile combination 1 and 3 provides the largest loads as the loads are in phase exceeding the preload as well causing almost a critical situation. Failure may occur for sea states, which are hardly observed in the 14 years data set. However, it is interesting to investigate the probability of occurrence of the considered load cases. Stochastic analysis such as Monte-Carlo simulations are required in which the probability of each individual parameters can be assessed.

Finite element analysis is used to derive capacities in V-H loading space numerically. The diagrams showed similarity with results found by Feng et al. (2014). The shapes presented by ISO 19901-4 underestimate the capacities for a square footing on a soft clay layer. An expression is provided which can be used to approximate the failure envelope. The failure envelopes are assuming the loads to be uniformly distributed over the mud mats, while the diagonal loading case provides a triangular stress distribution. In this study all loads are assumed to act uniformly distributed over the mud mats to compare the loads and capacities. The comparison of the interaction diagrams by ISO 19901-4 and this study showed an increase up to 8 % of more covered waves during horizontal loading, while for diagonal loading an increase up to 16 % is observed.

6

Assessment of the bearing capacity of two layered system

Chapter 5 provided the assessment of the bearing capacities in V-H loading space for footings at a soft clay layer. In this chapter, the bearing capacities are presented in three-dimensional loading space since the horizontal loads acting on the piles will provide moment loading, which is experienced by the soil. The envelopes are presented for two mud mats rigidly connected to each other as symmetry is taken at the y-axis. Double symmetry is not considered since the failure mechanism during combined loading is not symmetric. Assuming double symmetry would therefore lead to an incorrect assessment of the stability.

This chapter describes first a technique which is used to model the penetration of the mud mats as the total system is loaded to failure. A mathematical description of the technique is provided whereupon the load - penetration diagrams are presented. Next, the resulting interaction diagrams are presented in V-H-M loading space for a single clay layer at surface and in case of embedment. Load - penetration curves are derived for a soft soil layer on top of a stronger glacial till layer whereupon the interaction diagrams are presented for the double layered case finishing with the comparison between the single and double layer system.

6.1. Press-Replace technique

Actual combined loading consists not only of vertical and horizontal loading but also involves moment loading. It is more appropriate to present the capacities not in V-H loading space but in the in H-M loading space at a constant vertical load. If the resultant loads exceed the load carrying capacity of the soil, the mud mats will settle until an equilibrium between load and capacity has been found. Capacities of a penetrating footing is usually calculated with the analytical 'wished-in-place' method incorporating traditional bearing capacity equations. However, the penetration process is continuously on-going and to capture this process right, large deformation analysis is required.

Since this kind of analysis is beyond the scope of this study, the process is captured by implementing the so-called Press-Replace technique (PR Technique) introduced by Engin (2013). This technique, tested with a simple soil constitutive model, is based on a sequence of small deformation analysis incorporating a 'wished-in-place' footing. The initial mesh is preserved meaning that no mesh update is required after a calculation step and therefore computation time is saved. The PR Technique incorporates a step wise application of prescribed displacement followed by an update of the geometry. With the update is meant that the soft soil, which is displaced, is replaced by the material properties of the footing. A visualisation of the technique is provided in Figure 6.1 showing the progress of the pile penetration. The dark colour material presents the pile extending in depth after each loading phase, whilst the replacement of the soil by the pile material is shown as well. This technique is initially developed for 2D applications, but there is no limitation that it could not be used on 3D applications.

In order to model the penetration of the footing, the geometry is updated resulting in an update of the global stiffness matrix, denoted with K^{ph}, at the beginning of each phase. Subsequently, vertical displace-

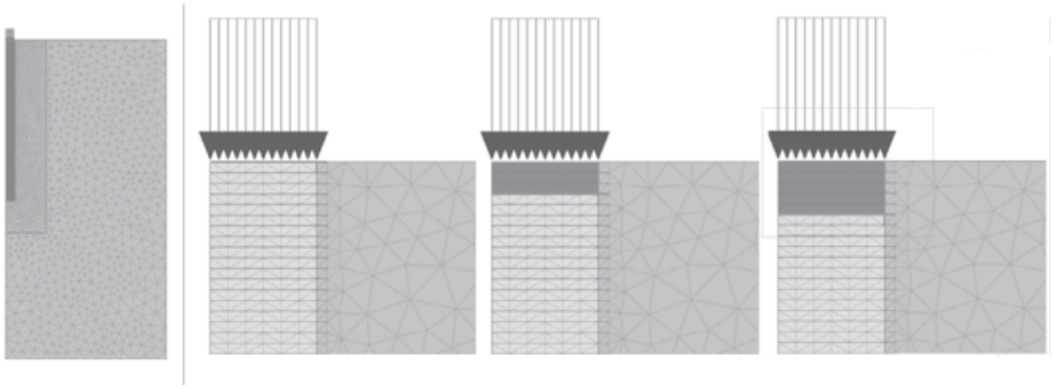

Figure 6.1: Visualisation of the Press-Replace technique and progress of penetration of the pile[6]

ments are applied such that the footing penetrates into the soil. The mathematical description of the update of the stiffness is given in below.

$$K^{ph} \triangle u = \triangle f^{ph} \tag{6.1}$$

in which the load increment equals the total unbalance $\triangle f^{ph}$ at the beginning of the phase. This term is defined as:

$$\triangle f^{ph} = f_{ex}^{ph} - f_{in}^{ph,0} \tag{6.2}$$

where f_{ex}^{ph} is the external load vector at phase ph. $f_{in}^{ph,0}$ is the internal reaction vector at the beginning of phase ph and can be calculated as:

$$f_{in}^{ph,0} = \int B^T \sigma^{ph,0} dV \tag{6.3}$$

B^T is the matrix containing the derivatives of the shape functions and $\sigma^{ph,0}$ is the stress state at the beginning of the phase, i.e. the present stresses at the end of the previous phase. For a more accurate and converged solution, the total unbalance is solved in multiple steps, denoted with i. After each solved step, the global system is updated and is given with Eqs. (6.4) and (6.5).

$$K^{ph} \triangle u^{ph,i} = \triangle f^{ph,i} \tag{6.4}$$

$$\triangle f^{ph,i} = f_{ex}^{ph,i} - \int B^T \sigma^{ph,i-1} dV \tag{6.5}$$

After the global system is updated, the predefined displacements are used with the updated system to determine all the reaction forces. The procedures of deriving the forces are described in Potts and Zdravković (1999) [26].

The total force equilibrium within each step, i, during solving the total unbalance is also checked. A certain tolerance is set, in case that the unbalance meets this limitation, the displacement can be updated. This procedure is applied until the desired, predefined, penetration depth has been reached.

$$u^{ph,i} = u^{ph,i-1} + \triangle u^{ph,i} \tag{6.6}$$

How is it applied?

To apply the PR Technique small slices are defined in the initial mesh configuration, directly beneath the footings. The use of coarse mesh in combination with higher order elements rather than finer mesh with lower order elements is preferable since smoother distributions of the stresses are obtained together with the improvement of the numerical performance [6].

In the first calculation stage, the pore pressures are generated. Subsequently, the footing is inserted, which is in full contact with the soil whereupon the PR technique is applied. The penetration process is simulated by the application of prescribed displacements which are equal to the step size considered in this study, i.e. $u_z = t_s$.

Interface elements at the base and next to the side walls are defined for mesh improvement and proper modelling of the soil-footing interaction. Interface extensions are added to avoid stress concentrations in the corners of the mud mats. Engin (2015) proved that the extension length had no notable influence on the stress distributions and computation time. For practical reasons, the extension length is chosen to be equal to the slice thickness. Figure 6.2 shows a visualisation of the footings with defined interface elements in which the slices are defined a thickness t_s. The darker boxes represent the footings of the template with the load acting in the load reference point. The interface elements in green are for the proper modelling of the soil-foundation interaction. The extensions in black are added to prevent premature failure next to the footings, while the interface elements represented by the orange line have no strength. To make a proper comparison with the analytical solution, side wall friction is neglected.

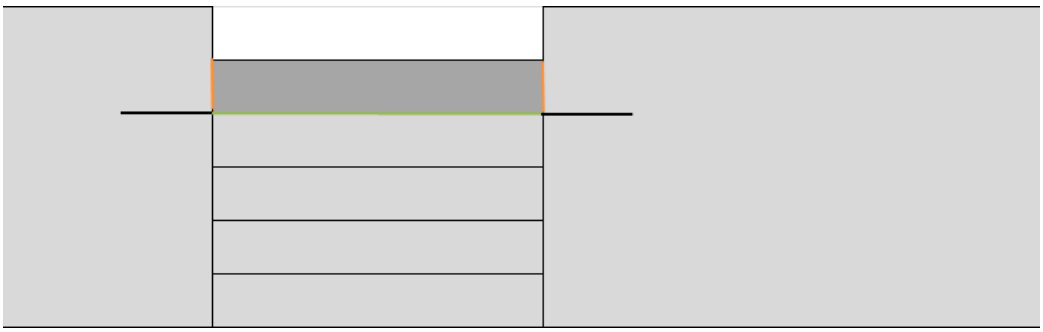

Figure 6.2: The Press-Release technique applied in clay with the defined interface elements

Appropriate interface stiffness and strength have to be assigned to the interface extension elements. If a Mohr-Coulomb soil model is used, strength properties of the neighbouring soil should be assigned to the interface elements. Defining peak or residual strength parameters results in either unrealistic high peak stresses beneath the footing or in numerical difficulties [6]. To overcome this issue, Engin (2013) suggests to assign high strength and stiffness values to the interface extensions and equal properties as the adjacent soil to the interface at the footing base. This way, the soil-footing interaction is not affected and the extensions will not fail nor deform resulting in improved load - penetration curves. Therefore, the interface extensions are assigned 10 times stronger and stiffer material properties than the adjacent soil.

Finite element model

In the finite element model for the V-H-M interaction diagrams, symmetry is taken around the y-axis meaning that two mud mats are modelled as rigid bodies which are solely able to translate or rotate. The Mohr-Coulomb constitutive soil model is still used to obtain a first approximation of the bearing capacities. The boundaries of the model are determined to be 4B from the coordinate system and normally fixed at the x- and y-axes while the bottom of the model is fully fixed. The interface elements described in Section 6.1 are incorporated for proper modelling of the interfaces.

The pre-piling template is assumed to react as a single rigid body on the environmental loading acting in the center of the structure. In the finite element model, the load reference point is defined in the center between the two mud mats since taking the point in the center results in an additional moment around the x-axis due to the self-weight which is not present with the assumption of considering the template as a single rigid body. Since a double-footing system is modelled, a new mesh dependency study is performed.

A coarse mesh with 55063 elements and 79309 nodes is chosen providing N_{cV} = 6.65 and N_{cH} = 1.0 instead of finer, medium, mesh containing almost three times as much elements and nodes with an improvement of only 2 % in vertical capacity. The incorporation of a coarse mesh with high order elements is more preferable as smoother stress distributions are obtained [6].

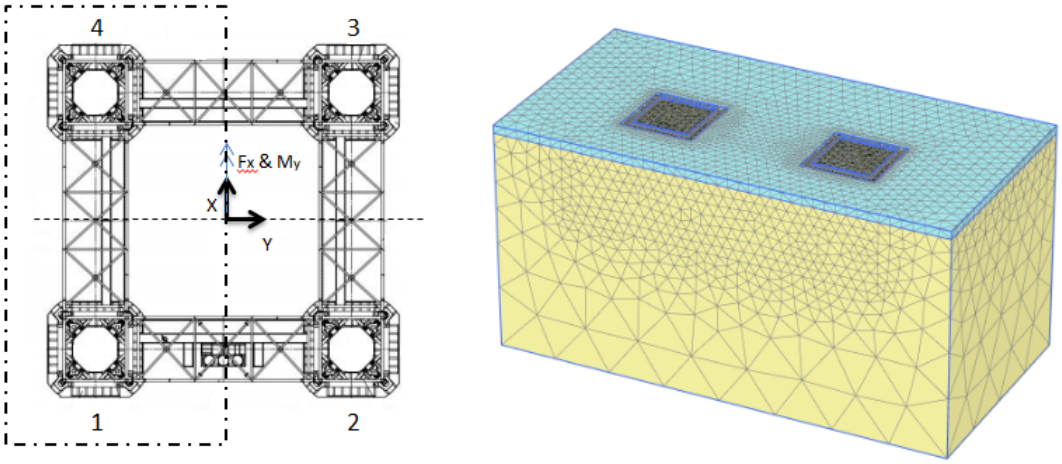

Figure 6.3: Wikinger pre-piling template with taken symmetry at the y-axis and finite element model with incorporated mesh configuration

Table 6.1: Mesh dependency study for the PR technique with two mud mats

Number of elements	Number of nodes	V_{ult}/As_u	H_{ult}/As_u
13211	21393	7.22	1.0
23635	35964	6.80	1.0
34326	56664	6.76	1.0
55063	79309	6.65	1.0
61469	94693	6.57	1.0
139415	201431	6.53	1.0

6.2. Continuous process of penetration

The continuous process of penetration is modelled using the PR technique and presented in load-penetration curves for two square footings positioned on surface of soft clay. Figure 6.4 shows the curves for a single clay layer in which the influence of the step size is given as well.

A maximum difference of 6 % is observed for the step sizes t_s = 0.1 and 0.3 at a normalised depth of 0.17. Using smaller steps results in smoother stress distributions and subsequently smoother load - displacement responses. When a structure has to penetrate to large depths, larger step sizes can be taken to speed up to calculations. However, this will be at the expense of the accuracy of the calculation. In this study, a step size of 0.1 m is chosen as it is assumed to present the curves accurately with this small step-size interval. By considering small step sizes, smoother curves will be obtained. However, an increase in computation time is inevitable and therefore is chosen for t_s = 0.1. To compare analytical and numerical methods, the load - penetration curve derived according to ISO 19901-5 is included as well.

Figure 6.4 shows the capacity increasing over depth, which basically can be attributed to boundary effects as the soil strength is constant over depth. Increasing penetration enhances the depth factor and the surcharge terms. The curves by both methods increase with different slopes. ISO 19901-5 provides a bearing capacity factor for strip footings, which is initially not derived for taking the effect of increasing depth into account. Application of the PR technique results in the continuous change of the problem rather than solving the problem in small steps, resulting in the convergence of the solution. This may also cause the curves to increase with different slopes.

The curve determined according to ISO 19901-5 provides capacities taking into account solely plastic deformation. It does not take into account the elastic deformations which occur during settlements. The curves derived with Plaxis 3D include both elastic and plastic deformations. In this study is assumed that all deformations are plastic and therefore the elastic part is neglected. While ISO 19901-5 considers purely plastic deformation, Plaxis provides both elastic and plastic deformations.

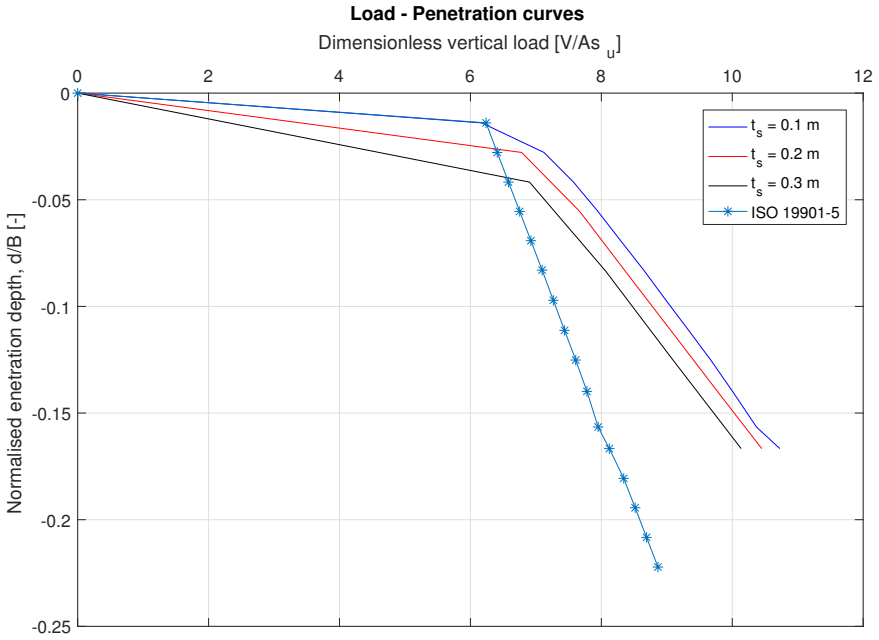

Figure 6.4: Penetration of clay incorporating different step sizes

The capacity after preloading, i.e. at d = 0.20 m, is crosschecked by using the curves of both methods. According to ISO 19901 - 5, the vertical capacity for two mud mats after preloading equals 2658 kN. Considering a step size t_s of 0.1 m provides a bearing capacity factor of 7.12 resulting in a vertical capacity of 2954 kN. This gives a difference of 11 %, mainly due to the numerical inaccuracy during determining the mesh configuration. A small part can be contributed to the conservatism in the semi-empirical parameters used in the wished-in-place method.

6.3. Resulting V-H-M interaction diagrams - single clay layer

Horizontal loads acting on the piles provide a moment loading experienced by the soil when shifted to the soil. Hence, the failure envelopes are presented in three-dimensional loading space. To prevent complex shaped figures, the envelopes are presented in H-M loading space for constant vertical load. This section provides the envelopes for two mud mats on soft clay placed at the seabed.

Three vertical load ratios V/V_{ult} = 0.25, 0.50 and 0.75 are considered providing slices of the complex graph. With the slices at the start, at the center and approach the maximum vertical capacity, the effect of the vertical load is seen on the H-M capacity diagrams. Figure 6.5 provides the interaction diagrams for the different vertical load ratios for two mud mats at surface of a soft clay layer.

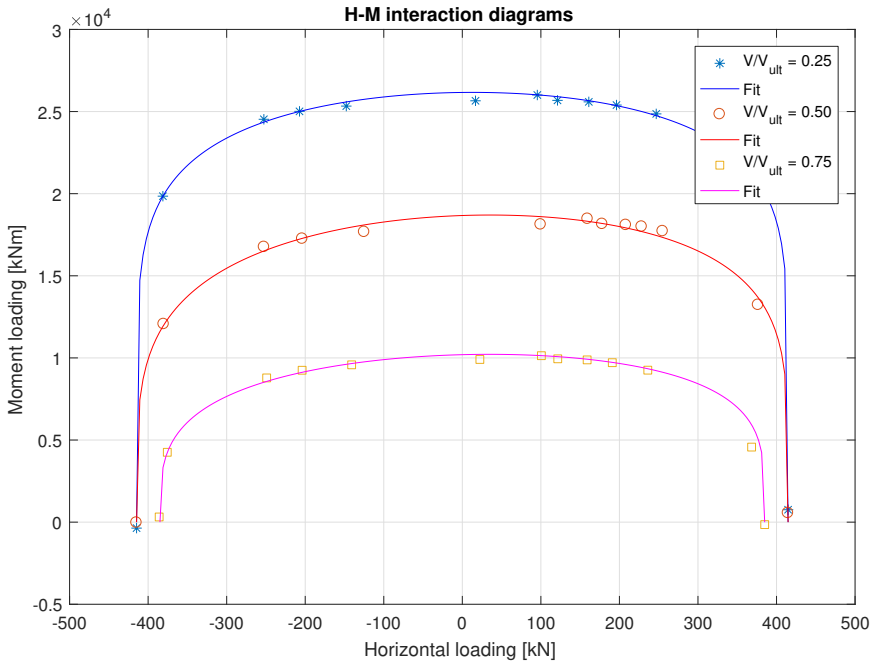

Figure 6.5: H-M interaction diagrams for surface square footings for different quasi-constant vertical load ratios

The failure envelope for V/V_{ult} = 0.25 is almost symmetrical around the y-axis. The proposed line fits the data points well in both -H+M and +H+M planes. The maximum horizontal and moment capacities equals the ultimate capacities. However, the ultimate moment capacity is obtained in combination with positive horizontal loads varying from 100 to 200 kN depending on the level of vertical load. Inclination of the graphs are not observed since tension is not able to developed due to the perforated mud mats and the footings are positioned at seabed. For V/V_{ult} = 0.50, the graph starts to oblique. An expression is used to fit the data points which is able to capture this asymmetric behaviour. The horizontal capacities match nicely the horizontal capacities calculated according to ISO 19901-4. Until V/V_{ult} = 0.5, the horizontal load acts independently of the vertical load. With increasing vertical load, the horizontal capacities start to decline.

A distinction can be made between two failure mechanisms. The vertical sections of the failure envelope, where dH/dM = 0, provide that no plastic deformations occur due to rotations but due to sliding. The second failure mechanism is a combination of rotation and sliding, which is dominant for moments larger than 15000 and 9000 kNm for V/V_{ult} = 0.25 and V/V_{ult} = 0.50, respectively. For V/V_{ult} = 0.75, sliding occurs with moments less than approximately 4000 kNm. The overall behaviour is the larger the horizontal force becomes, the smaller the moment becomes the soil can bear resulting in global failure of the pre-piling template.

Figure 6.6 shows the displacement vectors for square footings positioned on surface for different loading states for V/V_{ult} = 0.5 showing the failure mechanisms for different loading combinations. The applied vertical load causes the footings to be pushed into the soil whereupon the purely horizontal displacement is applied. This results in inclined vectors rather than purely horizontal in the sliding mechanism. During slid-

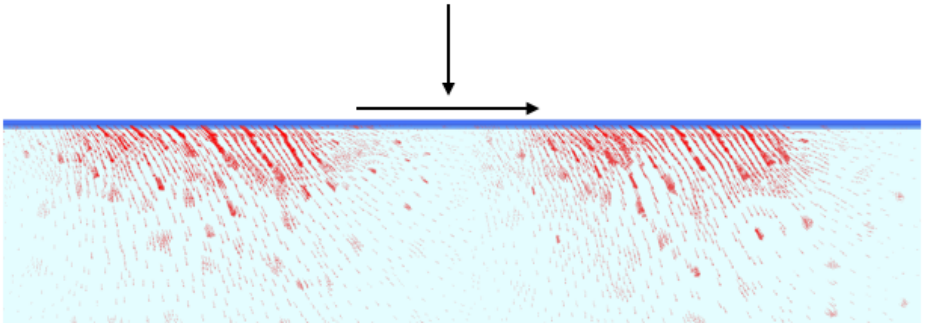

(a) Displacement vectors for pure horizontal loading with constant vertical load

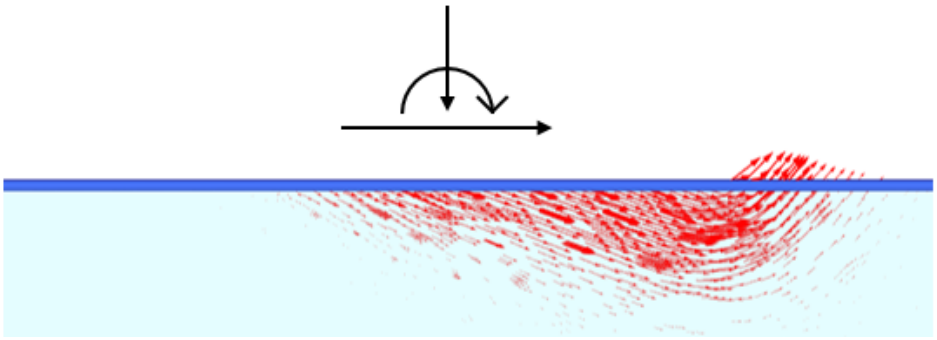

(b) Displacement vectors for combined moment and large horizontal loading with constant vertical load

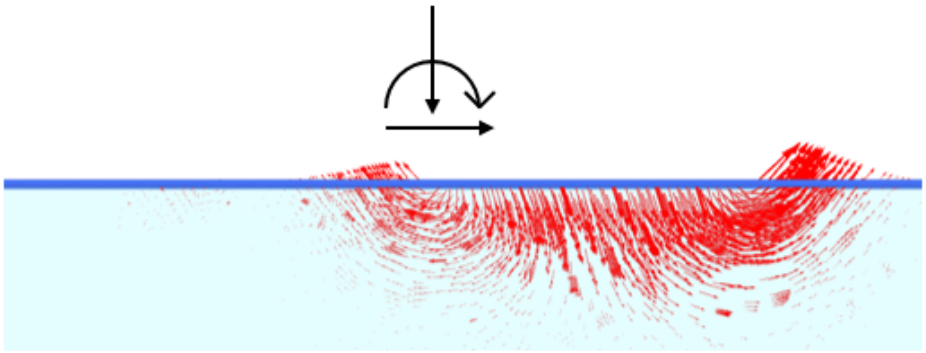

(c) Displacement vectors for combined moment and small horizontal loading with constant vertical load

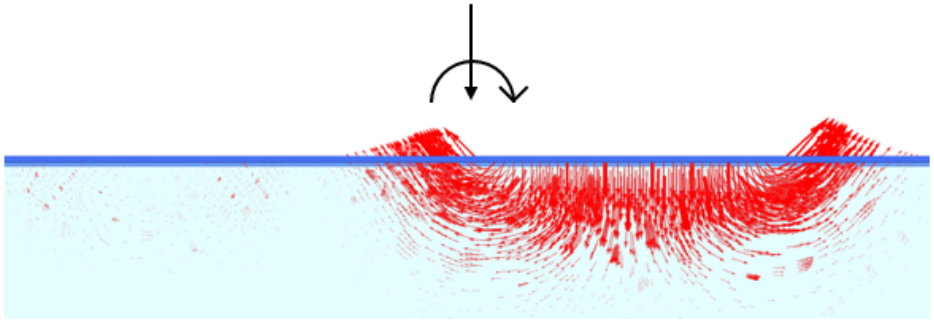

(d) Displacement vectors for pure moment loading with constant vertical load

Figure 6.6: Displacement vectors for the single layer case with $V/V_{ult} = 0.5$ for pure horizontal loading, $h/B/\theta = 10$, $h/B/\theta = 1$ and pure moment loading

ing, the soil is uniformly mobilised directly beneath the mud mats if it were not for the fact that the vectors are scaled showing the mechanism extending to larger depths. During combined moment and horizontal loading with a large horizontal load component, a scoop failure mechanism is observed consisting of sliding and rotation. The failure is emphasised at the right footing as the moment loading presses the mud mat in the soil. The right part of the footing is compressed while the other side seems to pull up. With decreasing horizontal load, the failure mechanism transitions towards a combination of compression and sliding with rotational failure. Two independent failure mechanisms occur in which the right footing is in compression due to the moment loading in combination with the slight horizontal load. The left footing starts to rotate with a slight soil heave next to the footing. These two mechanisms are even more emphasises during purely moment loading.

The mud mats will start to settle if the loads exceed the capacities resulting in enhancement of depth effects with the present overburden soil. Soil attached to the sidewalls is mobilised during sliding resulting in the development of passive soil pressures. The sidewall friction developed during embedment is disregarded providing conservative results. However, to capture the embedment properly, the footings are brought to the required depth using the PR technique whereupon the different displacement probes are applied to derive the data points for the failure envelopes. Figure 6.7 presents the interaction diagrams for two square footings at surface and embedded for V/V_{ult} = 0.50.

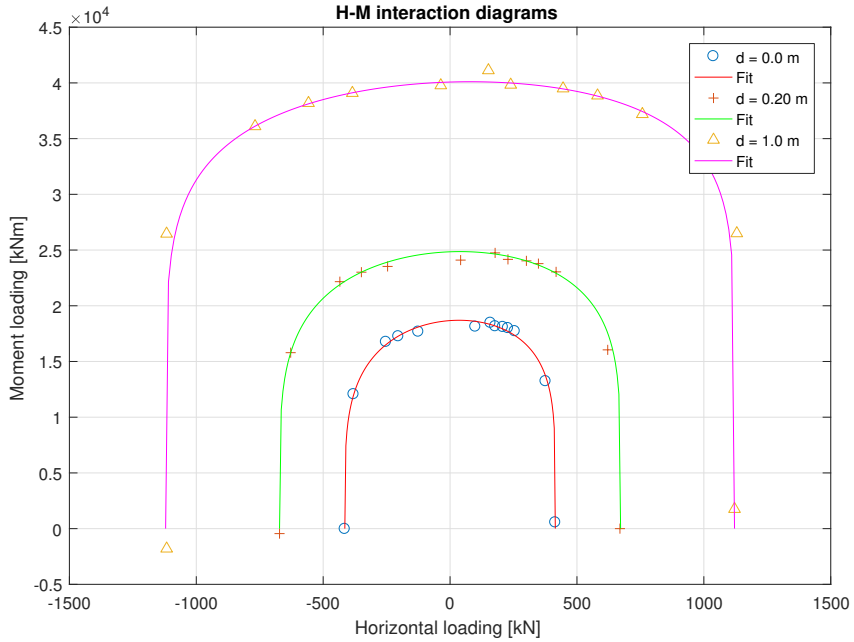

Figure 6.7: H-M interaction diagrams for surface and embedded square footings for different quasi-constant vertical load ratios

Two different embedment depths, d = 0.20 m and d = 1.0 m, are considered with the vertical load ratio V/V_{ult} = 0.50. This level is chosen since the vertical load comes most close to half the mass of the template, 133 t. The embedment of 0.20 m is considered as this equals the analytically determined penetration depth after application of the preload. For 1.0 m is chosen to see the effect at greater depths and when the footings rest on the stronger bottom layer as shown later on in the report. The asymmetrical character of the envelopes seems to be preserved in case of embedment. This can be explained as the horizontal load in positive direction prevents the rotational motion of the footing due to the moment loading. In other words, the rotational failure mechanism encounters resistance due to the horizontal load resulting in the increase of moment capacity with a positive horizontal load.

To observe the improvement in capacity, the capacities are provided in terms of bearing capacity factors in Figure 6.8.

An expansion of the failure envelopes is observed for embedded footing implying the increase in capacities. An increase of 60 % and 34 % is obtained for sliding and moment capacity, respectively, at d = 0.20

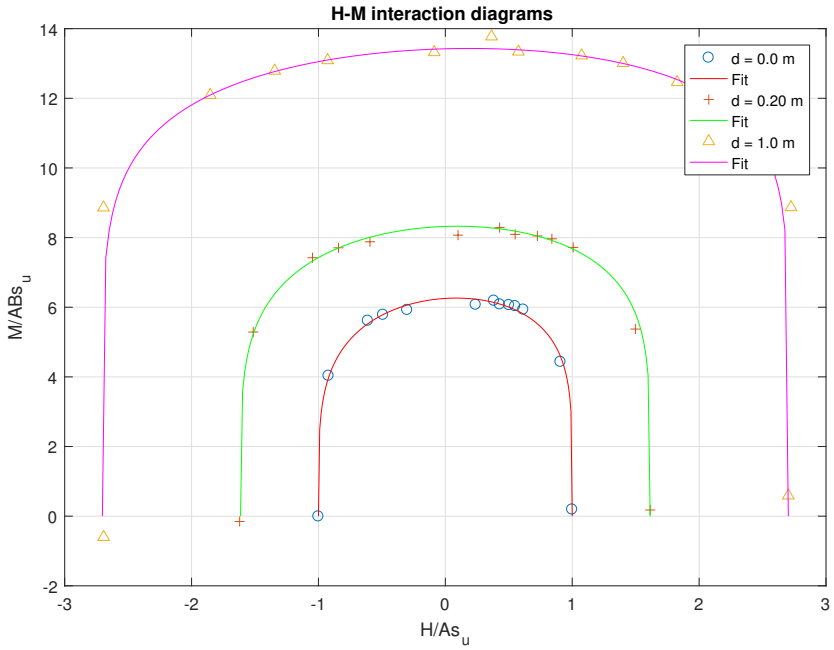

Figure 6.8: Dimensionless H-M interaction diagrams for surface and embedded square footings

m. At 1.0 m depth, the soil can bear drastically higher loads compared to footings positioned at the seabed. The expansions show to be beneficial for the global stability of the pre-piling template. For footings at 1.0 m depth, the envelope starts to incline since the maximum horizontal capacity does not coincide anymore with the ultimate horizontal capacity. The presence of moment loading allows for a slightly higher horizontal load. The fit used to describe the envelopes is not able to capture the inclination. However, the effect is rather small and therefore neglected. To investigate the uniqueness of the shapes, the envelopes are presented in normalised for different vertical load ratios in Figure 6.9.

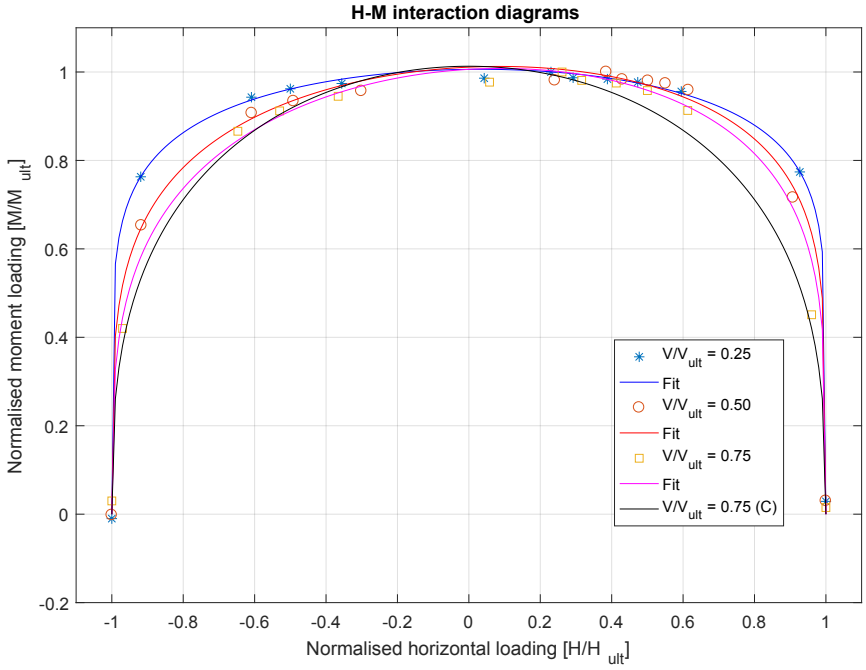

Figure 6.9: Normalised H-M interaction diagrams for square footings placed at surface

By assessing the shapes, a single expression can be proposed to approximate the capacities for a range of specific conditions which is the second step in constructing the failure envelopes. Multiplying the shape by the ultimate capacities, provides the envelope. The shapes for V/V_{ult} = 0.50 and 0.75 at surface do match each other well. For V/V_{ult} = 0.75, the expression is surrounded within the envelope for V/V_{ult} = 0.50. The envelope for V/V_{ult} = 0.25 includes more asymmetry compared to the other envelopes, especially in the -H+M plane. The differences get significant when the failure mechanism converges to a sliding mechanism. Towards a pure rotational failure, the envelopes match very well. Asymmetry of the shape is known to be influenced by the level of vertical load and embedment. Since the load fluctuates and the asymmetry in +H+M and -H+M plane is rather questionable, a compensated, conservative, fit is proposed of the expression for V/V_{ult} = 0.75 in which the lower part of the envelope is mirrored around the y-axis. Eq. (6.7) will provide proper approximations V/V_{ult} of 0.5 well but would definitely underestimate the capacities for V/V_{ult} = 0.25. However, in this study the load ratio of V/V_{ult} = 0.25 is not considered important. This load ratio may start to become important at larger depths as the ratio of self weight over ultimate capacity will decrease.

$$\frac{M}{M_{ult}} = 1.013 \cdot \left(1 - \frac{H}{H_{ult}}\right)^{0.3459} \left(1 + \frac{H}{H_{ult}}\right)^{0.3459} \tag{6.7}$$

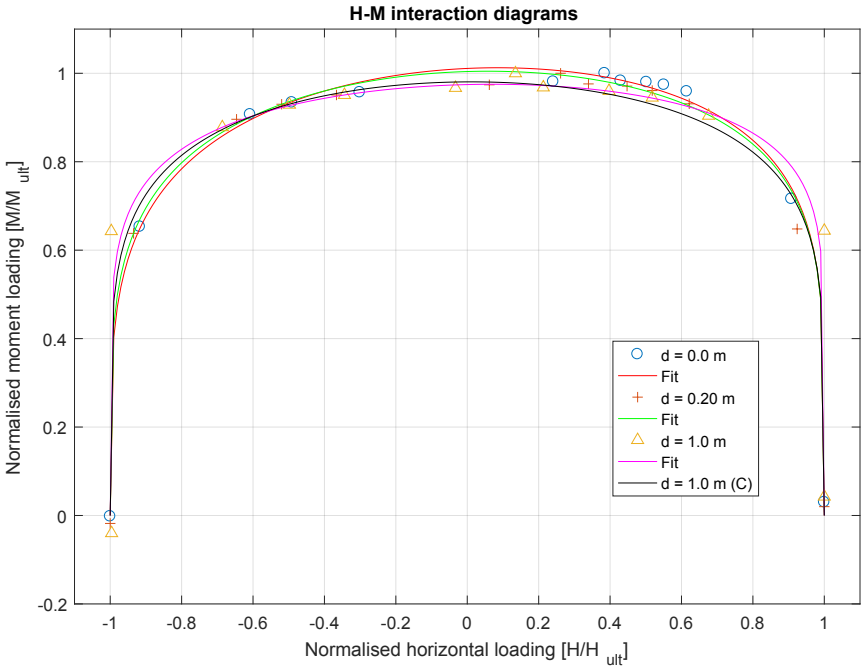

Figure 6.10: Normalised H-M interaction diagrams for embedded square footings with V/V_{ult} = 0.5

Figure 6.10 shows the normalised failure envelopes with a vertical load ratio of 0.5 at surface and at depths of 0.20 and 1.0 m. Increasing asymmetry is observed with increasing embedment as the envelope gets flattened during pure moment loading. The moment capacity is less affected by the horizontal loads for d = 1.0 m compared to the other cases. The fit determined to derive the capacities for a surface square footing may be used until a depth of 0.20 m. With more embedment, this fit would not provide adequate capacities and may therefore not be used. A conservative expression is proposed with the lower part mirrored around the y-axis to be used for the square footings at 1.0 m depth. The equation is given as Eq. (6.8).

$$\frac{M}{M_{ult}} = 0.9806 \cdot \left(1 - \frac{H}{H_{ult}}\right)^{0.1754} \left(1 + \frac{H}{H_{ult}}\right)^{0.1794} \tag{6.8}$$

6.4. Penetration in two-layer system

Reality shows the soil to be multi-layered as shown in Chapter 3 for Wikinger in which a three-layered system is found consisting of different properties. This section provides the penetration process of the mud mats incorporating a double-layered system. The soil is simplified to a double-layered system in which soft clay is resting on top of a stronger glacial till layer. Load penetration curves are provided derived with Plaxis 3D and are finally compared to analytical expressions recommended by ISO 19901-5.

A soft clay layer is modelled resting on a much stiffer and stronger glacial till layer. Both are assumed to have uniform strength over depth and to have undrained characteristics as the loading is instantly transferred from the piles to the soil. The water will not have the possibility to drain and therefore the loads are transferred to the pore water. The strength of the bottom layer is obtained from the soil characterisation presented in Chapter 3. Its stiffness is estimated as E_u/s_u = 400 [19] and the effective unit weight is taken from the tests from the offshore campaign. The top layer thickness is assumed to be 1.0 m since varying thicknesses are faced within the field. The boundaries of the model and mesh are kept equal as in the model for the single layer case. Table 6.2 provides an overview of the soil parameters used for the simulations.

Figure 6.11 shows the load required to let two mud mats penetrate to a certain depth. The PR technique models step wise the continuous process of penetration, while ISO 19901-5 recommends the traditional wished-in-place method.

Table 6.2: Input parameters of soft clay and glacial till for Plaxis 3D

Soft clay	
E/s_u	400
s_u [kPa]	4
$\gamma'[kN/m^3]$	6
v [-]	0.495
Glacial till	
E/s_u	400
s_u [kPa]	35
$\gamma'[kN/m^3]$	11.6
v [-]	0.495

The wished-in-place method provides a constant increase followed by a rapid increase in capacity until a depth of 1.0 m whereupon the capacity increases linearly. After a depth of 0.7 m, squeezing of clay is observed which becomes harder when the bottom of the top layer is approached since more load is required to squeeze the little remaining part resulting in the rapid increase of the capacity. When the top layer is fully penetrated, the capacity of the bottom layer starts to become governing. The failure mechanism will transition from squeezing to general shear failure in the till layer.

A similar shaped curve is obtained in this study with a higher rate of increase in the first half meter. Towards the bottom of the top layer, the curves are converging towards each other whereupon the capacity of the bottom layer starts becoming governing as observed at 1.2 m depth. The curve obtained in this study shows a fluent transition from the top to the bottom layer, which is expected rather than a sharp transition as observed in the wished-in-place method. The transition point in the curve is found to be in the bottom layer which might be due to the small step sizes incorporated in the analysis providing the data points. By refining the step size, a smoother transition will be obtained. The larger rate of increase over depth found in this study will result in increasing difference between both methods.

To observe the difference in capacities, the capacities are presented in dimensionless values while the penetration depth is normalised with the breadth of a single footing. The curves for a single layer of Holocene deposits and Glacial till are added as well such that the effect of a second, stronger, layer emerges. Both methods show that the capacities are nicely between lower and upper bound.

Comparing the single layer and double-layered systems show that for a bottom layer starting at 1.0 m

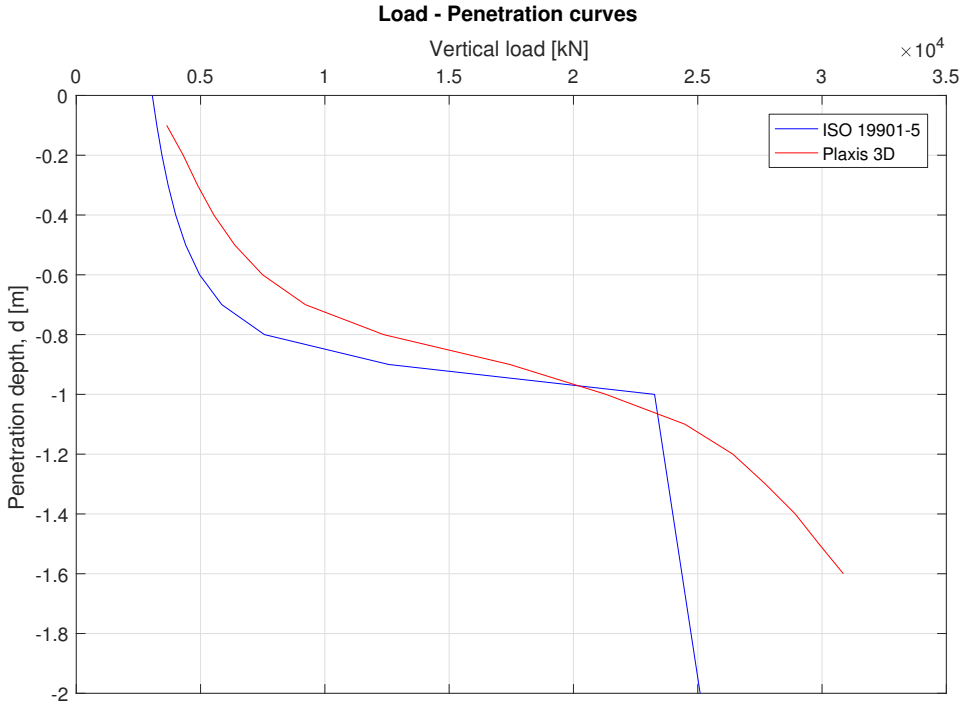

Figure 6.11: Load-penetration curves derived according to ISO19905-1 and this study

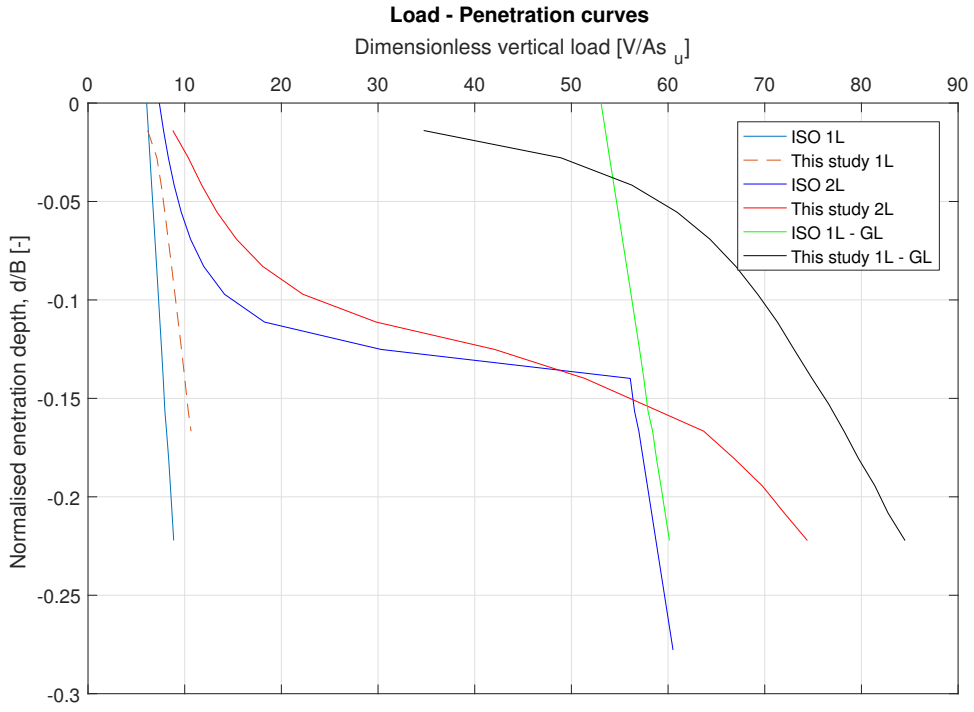

Figure 6.12: Dimensionless load-penetration curves in case of a single and two layered system

depth, the bearing capacity at the seabed is already enhanced. The capacities near seabed are similar but diverge with increasing depth. Especially at d/B = -0.1, there is a large difference but this becomes smaller towards the bottom of the top layer, d/B = 0.14. The difference in capacities arises mainly due to the inaccuracy of the mesh. Another reasons for the difference might be that ISO 19901-5 incorporates a bearing capacity factor for strip footings not derived to take possible depth effects into account and the wished-in-place method considers solely plastic deformations while Plaxis 3D provides both elastic and plastic deformations.

6.5. Resulting V-H-M interaction diagrams - two layer system

Section 6.4 showed already the significant influence of a second, stronger bottom layer on the vertical capacity during purely vertical penetration. As layered soils are present, the operability of the pre-piling template is assessed on soft soil resting on top of stronger soil layer. This analysis will provide whether the incorporation of a second layer is beneficial for the global stability of the template.

Figure 6.13 shows the interaction diagrams in H-M loading space for three vertical load ratios V/V_{ult}, 0.25, 0.50 and 0.75.

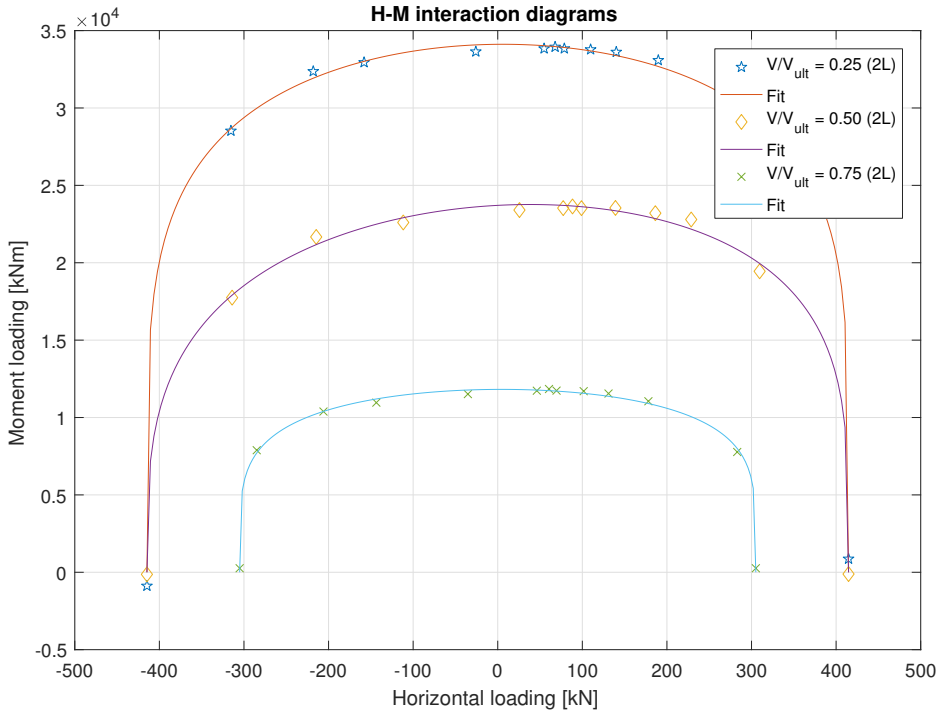

Figure 6.13: H-M interaction diagrams of square footings at the seabed for different quasi-constant vertical load ratios with a soft clay layer resting on a glacial till layer.

The horizontal capacities of the footings are not affected up to a vertical load ratio of 0.50. For V/V_{ult} = 0.75, a significant reduction is observed in the horizontal capacities are reduced due to the presence of a high vertical load. Interaction diagrams in dimensionless space are presented for both the single layer and double layer case allowing for a comparison between both cases. Figure 6.14 presents the envelopes for both situations.

A great increase in moment capacities is observed for all vertical load ratios while the horizontal capacities are not affected. Only the horizontal capacities for V/V_{ult} = 0.75 showed a reduction which is due to the presence of the vertical load. For V/V_{ult} = 0.25, the pure moment capacity increased with 30 % as for V/V_{ult} = 0.50 an increase of 28 % is observed. For the higher vertical load ratio, the influence of the bottom layer seems to decrease as a gain of 16 % and a reduction of 20 % is obtained in moment and horizontal capacity, respectively, compared to the single layer case. The reduction compared to the unaffected horizontal capacities is greater as well with 26 % for the double-layered case and only 7 % for the single layer case.

Displacement vectors are presented for different loading states to show how the loading displaced the soil. Given the visualisation is tried to explain the mechanism which causes the increase in capacities. Vectors are provided for purely horizontal loading, combined horizontal and moment loading and purely moment loading in the H-M interaction for V/V_{ult} = 0.5.

Similar failure mechanisms are observed compared to the single layer case where sliding occurs due to horizontal loading and a scoop failure mechanism is observed with a moment and large horizontal load. The sliding and rotational mechanism transitions towards two independent failure mechanism with decreasing

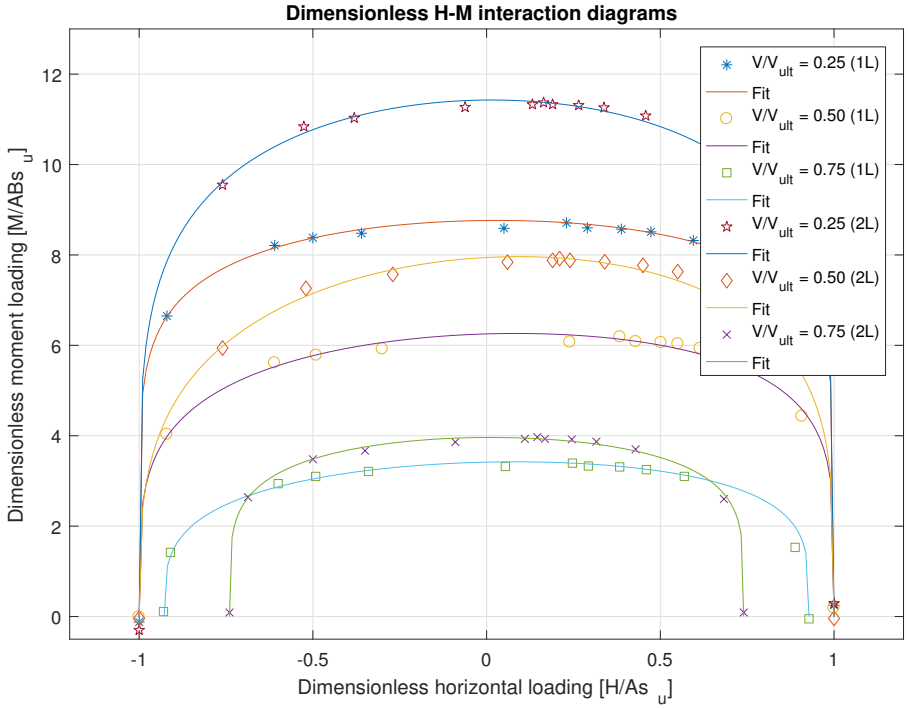

Figure 6.14: Dimensionless H-M interaction diagrams for square footings on the seabed in case of a single and double layered system

horizontal loading. During pure moment loading, at the left footing a rotation is excited which is hardly visible due to the small size of the vectors. The vectors show that settlements were hardly able to penetrate in the bottom layer but are forced to expand to the width. As the soil is pushed towards the breadth, more soil mobilisation is realised resulting in the increase of moment capacity. As sliding does not mobilise deeper soils, no increase in horizontal capacity is observed. To investigate the effect on the shapes, the envelopes are presented in normalised space whereupon a comparison is made between the single and double-layered system. Figure 6.16 shows the failure envelopes in normalised space.

The shapes of the envelopes show perfectly agreement in the +H+M plane. The maximum moment capacity occurs at a normalised moment of 0.1 whereupon the envelope for $V/V_{ult} = 0.50$ starts to diverge during the transition towards a combined sliding-rotation mechanism. Shapes for $V/V_{ult} = 0.25$ and 0.75 show good agreement in both -H+M and +H+M loading plane as the envelope for $V/V_{ult} = 0.75$ falls slightly within the envelope for 0.75. The expression for $V/V_{ult} = 0.50$ is able to approximate the capacities for all loading cases in which the capacities in -H+M are underestimated. As the environmental loading is fluctuating, a conservative, symmetrical, expression is proposed. Since the difference in asymmetry in -H+M and +H+M loading planes are questionable, the lower part of the envelope is mirrored around the y-axis resulting in Eq. (6.9).

$$\frac{M}{M_{ult}} = 1.01 \cdot \left(1 - \frac{H}{H_{ult}}\right)^{0.3295} \left(1 + \frac{H}{H_{ult}}\right)^{0.3413} \tag{6.9}$$

In order to provide a single expression taking into account both the single and double-layered systems, the normalised envelopes are presented in Figure 6.17.

Figure 6.17 shows a close similarity in the shapes of all failure envelopes except for $V/V_{ult} = 0.25$ and 0.50. The expressions for $V/V_{ult} = 0.25$ in both cases and for 0.50 in the single layer case show increasing asymmetry during combined horizontal and moment loading. The shape for $V/V_{ult} = 0.50$ in a double layer system is therefore a good, conservative, approximation for the failure envelopes of two square footings rigidly connected considering the present conditions. Since the asymmetry is disregarded, the exceptional cases given above will be underestimated even more.

The interaction diagrams are also provided for the embedded footings. The presence of the bottom layer increased the capacity of the top layer at surface and caused an even greater enhancement for embedded

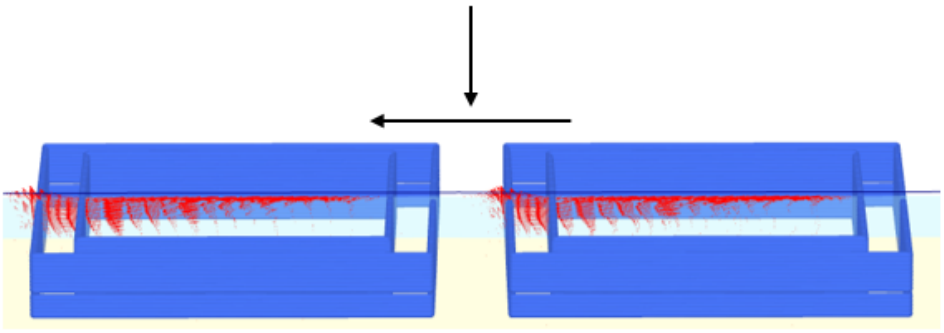

(a) Displacement vectors for pure horizontal loading with constant vertical load

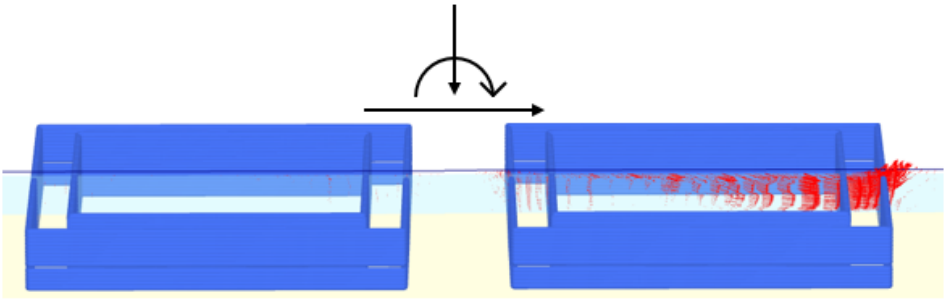

(b) Displacement vectors for combined moment and large horizontal loading with constant vertical load

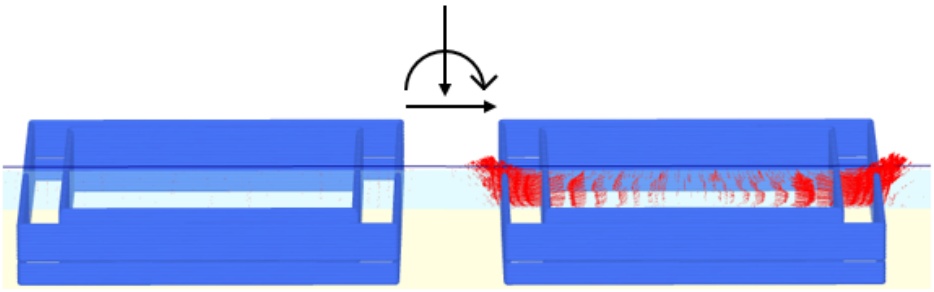

(c) Displacement vectors for combined moment and small horizontal loading with constant vertical load

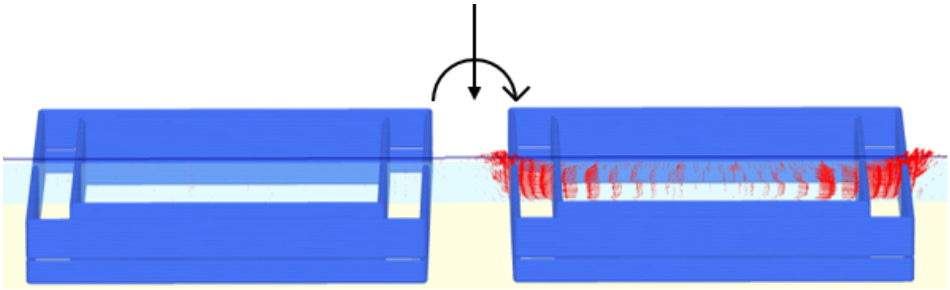

(d) Displacement vectors for pure moment loading with constant vertical load

Figure 6.15: Displacement vectors for the double-layered system with V/V_{ult} = 0.5 for pure horizontal loading, $h/B/\theta$ = 10, $h/B/\theta$ = 0.1 and pure moment loading

mud mats. The envelopes are presented in terms of absolute capacities for embedment of 0.20 m and 1.0 and are given in Figure 6.18.

Great enhancement is observed for embedded mud mats as shown by the expansion of the envelopes. For an embedment of 0.20 m, an increase of 40 % is obtained which is little compared to the case in which footings are settled to 1.0 m depth where an enhancement of 10 times is observed. Moment capacities are

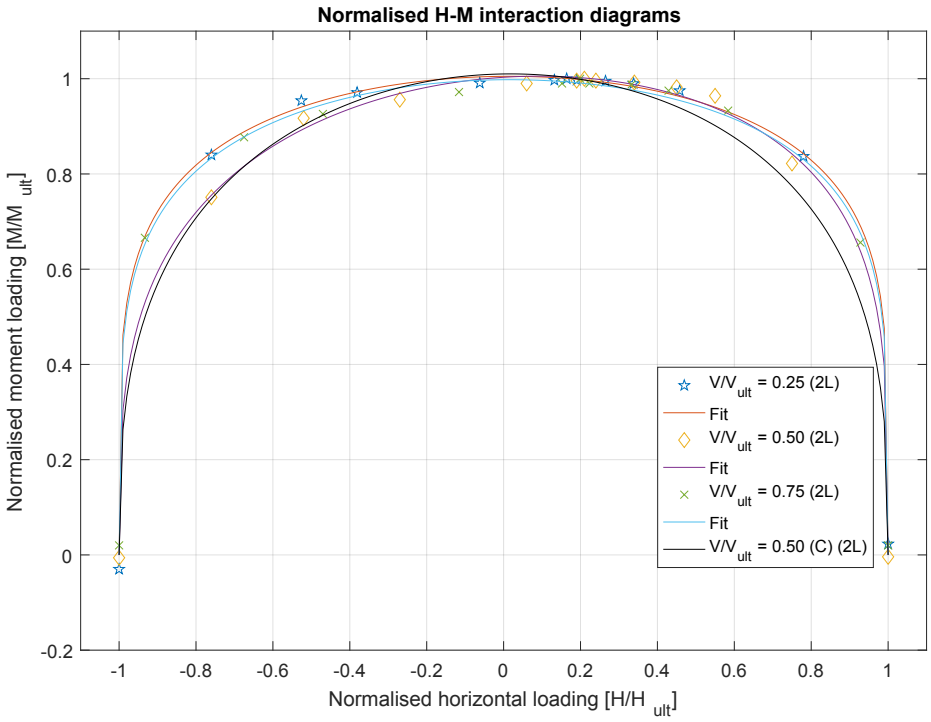

Figure 6.16: Normalised H-M interaction diagrams for surface square footings resting on a soft clay layer on top of a till layer

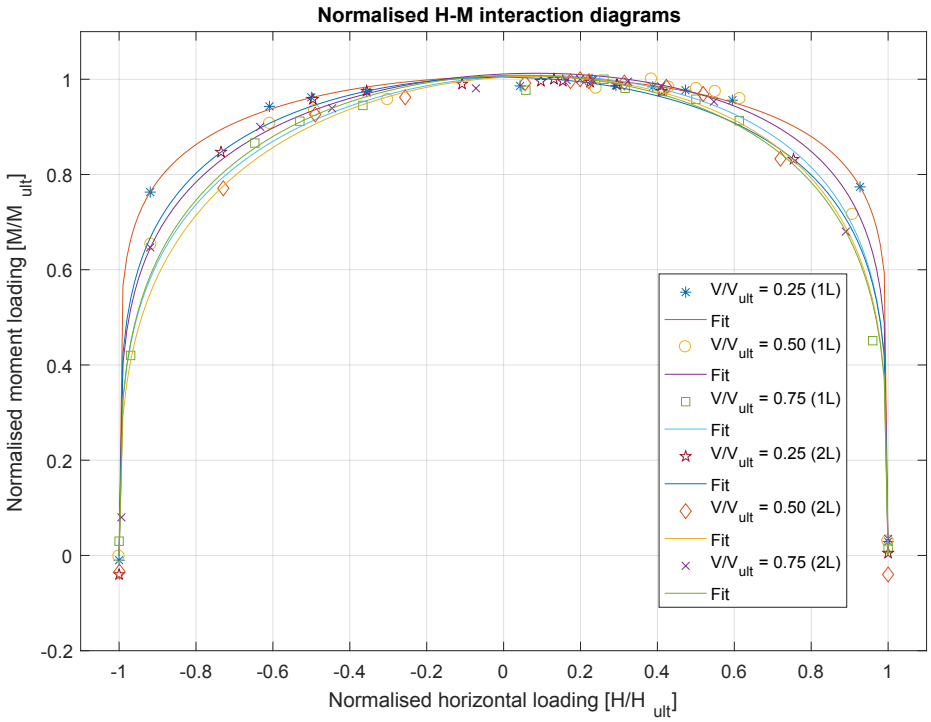

Figure 6.17: Normalised H-M interaction diagrams for surface square footings for a single layer and two layered system

increased with approximately 60 % and 10 times for d = 0.20 m and d = 1.0 m, respectively. A settlement of 0.20 m already caused a great increase which is beneficial for the global stability.

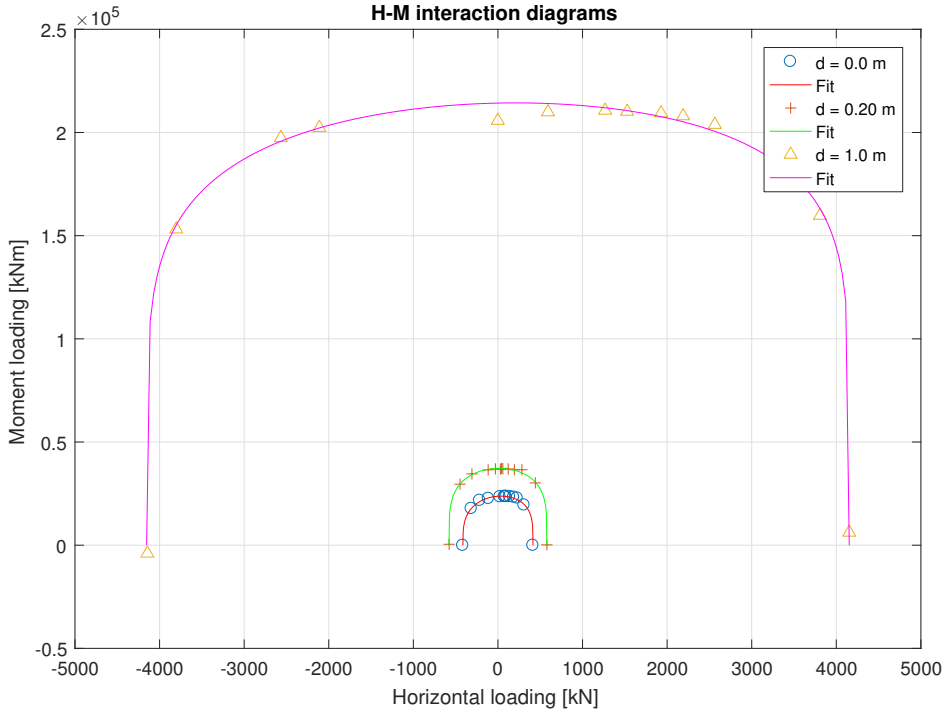

Figure 6.18: H-M interaction diagrams for surface and embedded square footings resting on a two layered system

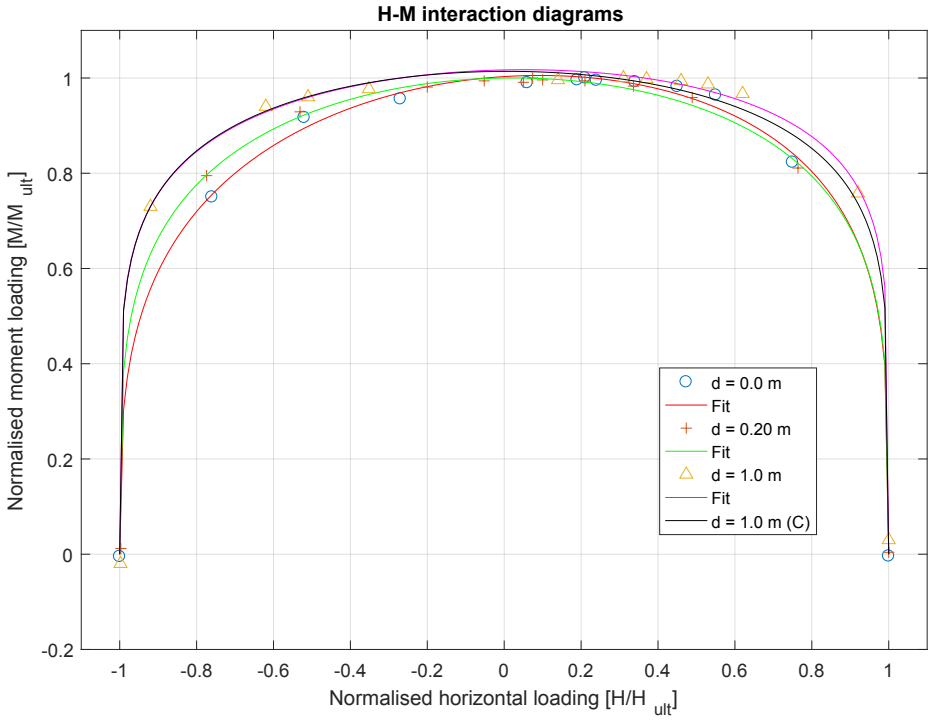

Figure 6.19: Normalised H-M interaction diagrams for surface and embedded square footings resting on a two layered system

The uniqueness of the shape of the envelopes for embedded footings is assessed. The expression proposed for the surface footing is applicable up to 0.20 m depth with a slight underestimation in the -H+M plane. Increasing embedment involves increasing asymmetry and therefore a new equation is proposed. The equation disregards the asymmetry in the envelope by taking symmetry of the lower part of the envelope and

is therefore conservative. Capacities for square footings in the current conditions can be approximated with Eq. (6.10).

$$\frac{M}{M_{ult}} = 1.014 \cdot \left(1 - \frac{H}{H_{ult}}\right)^{0.1718} \left(1 + \frac{H}{H_{ult}}\right)^{0.1745} \tag{6.10}$$

6.6. Effect of changing operational limits

In Chapter 5 the effect of changing the operational limits on the bottom stability is assessed for a single square footing on top of a soft clay layer in V-H loading space. This section provides an assessment of the effect of changing the operational limits in VHM loading space for two footings on soft clay resting on top of a glacial till layer. Loads for varying design waves are compared with the capacities whereupon is concluded whether the incorporation of a second soil layer might be beneficial for the bottom stability check. Design waves are varied in significant wave height from 0.25 m to 2.25 and in peak periods between 2 s and 7 s.

In the horizontal load case the situation in which all piles are stabbed is found as most critical providing the largest loads. Figure 6.20 provides the capacities at surface and at 0.20 m depth with the compressive loads experienced by two mud mats.

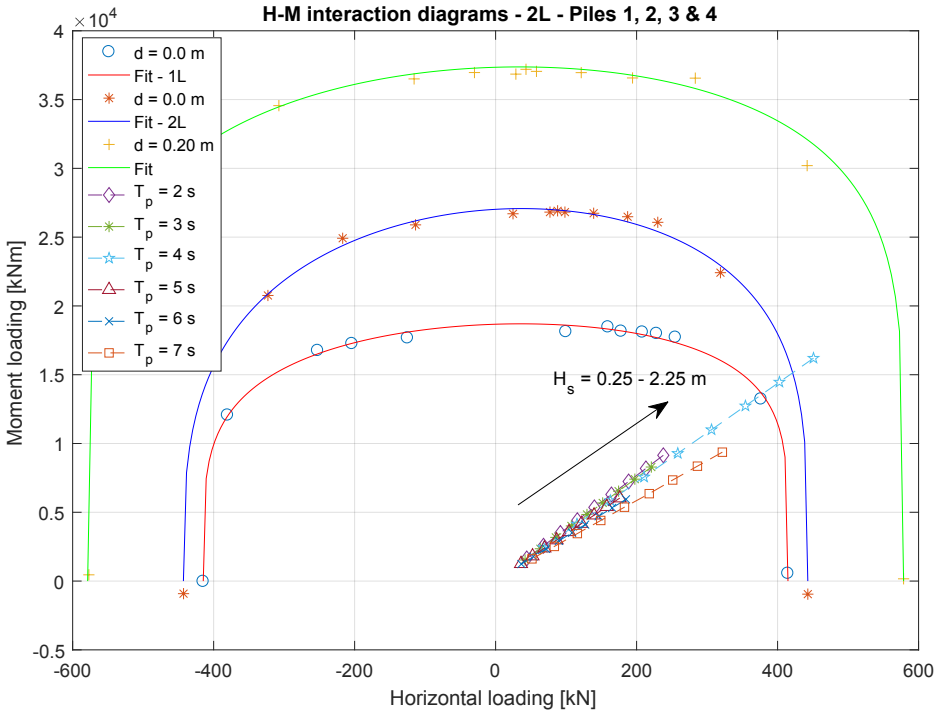

Figure 6.20: H-M interaction diagrams for surface and embedded square footings with the loads in case when all piles are in the pre-piling template for the horizontal load case

This case shows that sufficient capacity is present at surface to bear most of the loading. As the pre-piling template is preloaded, additional capacities are created which can bear the loads of the design waves for H_s = 0.25 - 2.25 m and T_p = 2 - 7 s. The incorporation of the second layer is indeed beneficial for the global stability check. As loads are transferred to the soil, the stability beneath the footings is assessed as well. For the local stability check, the loads are distributed to the mud mats and the mud mat being most in compression is examined on failure. The moment loading is decoupled as it contributes to the vertical load experienced by a single mud mat. The operational limits found most critical for a surface footing causing local failure are given together with the V-H interaction diagrams for the single and double layered system.

The V-H interaction diagram for a double-layered system is described with Eq. (6.11). An enhancement in vertical capacity is observed as soils at depth are mobilised. The horizontal capacity is exactly the same since

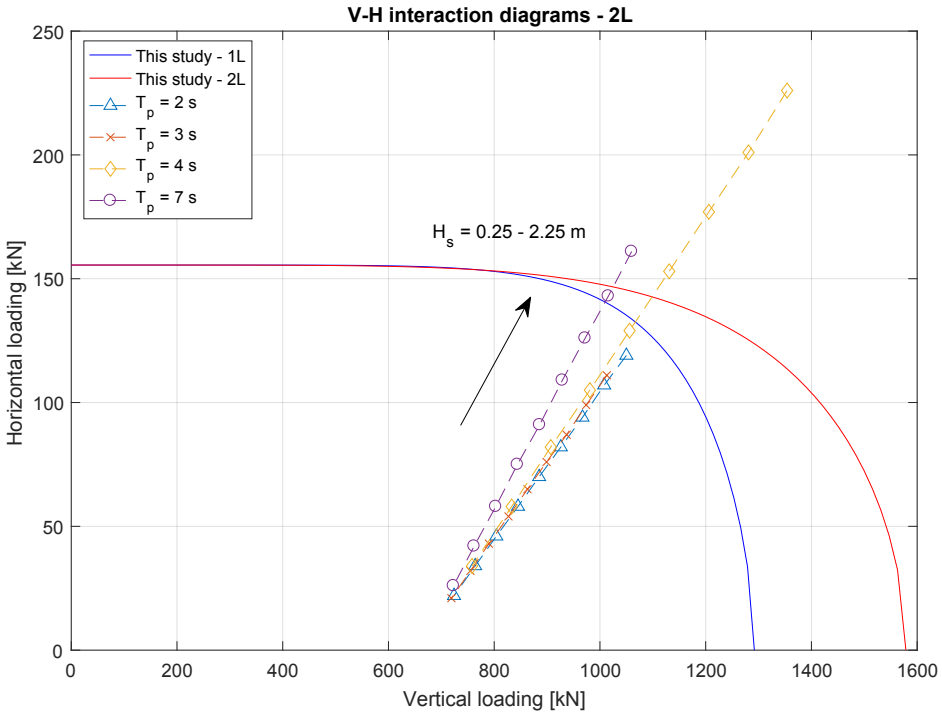

Figure 6.21: Local stability check for the horizontal load case given the failure envelopes for a single and double layer system

soil strength at seabed matters. Considering the critical loads show that hardly higher waves can be sustained which results in hardly more waves covered of the 14 years data set.

$$\left(\frac{H}{H_{ult}}\right)^{1.895} + \left(\frac{V}{V_{ult}}\right)^{5.221} = 1 \tag{6.11}$$

The diagonal load case shows that local failure is more critical than global failure as a single mud mat has to carry all the compression loads since the intermediate mud mats hardly contribute to the load transfer. Figure 6.23 provides the interaction diagrams with the moment and horizontal loading on two mud mats showing the global stability of the pre-piling template not to be an issue. The global stability checks for the other pile combinations are given in Appendix D.

In the diagonal loading case is shown for all pile combinations that global failure will not be an issue as all loads for the different design waves fall within the envelopes causing solely elastic deformations. As all compressive loads are taken by a single mud mat, the local instability of the most critical mud mat is checked. Given the V-H interaction diagram for a single layer, waves up to approximately 1.50 m can be sustained regardless of the peak period in the diagonal loading case. Figure 6.23 shows the V-H interaction diagrams for a single and double layer with the loads found to be critical arising from design waves heights varying from 0.25 - 2.25 m.

The incorporation of the second layer allows for waves up to 2.0 m for all peak periods between 2 and 7 s, which is a substantial increase compared to the single layer case. However, only 6 % more waves are covered of the data set. The presence of the bottom layer becomes beneficial for cases with high vertical loads as the diagonal loading case. Since only the vertical and moment capacities are increased, the second layer seems not per se to be beneficial. Considering the global stability of the pre-piling template, the addition of the second layer is indeed valuable. For the local stability check, the benefit of the stronger layer starts to diminish with increasing horizontal loads. If operational limits are considered for both loading cases separately, the presence of the bottom layer may be beneficial.

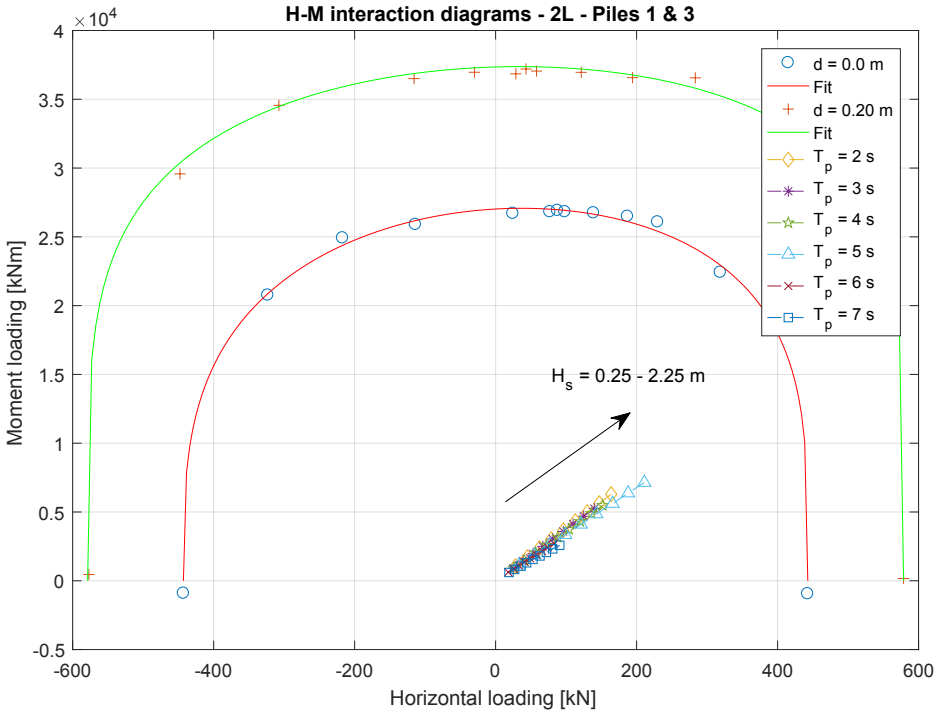

Figure 6.22: H-M interaction diagrams for a single surface and embedded square footing with the loads corresponding to piles 1 and 3 for the diagonal load case

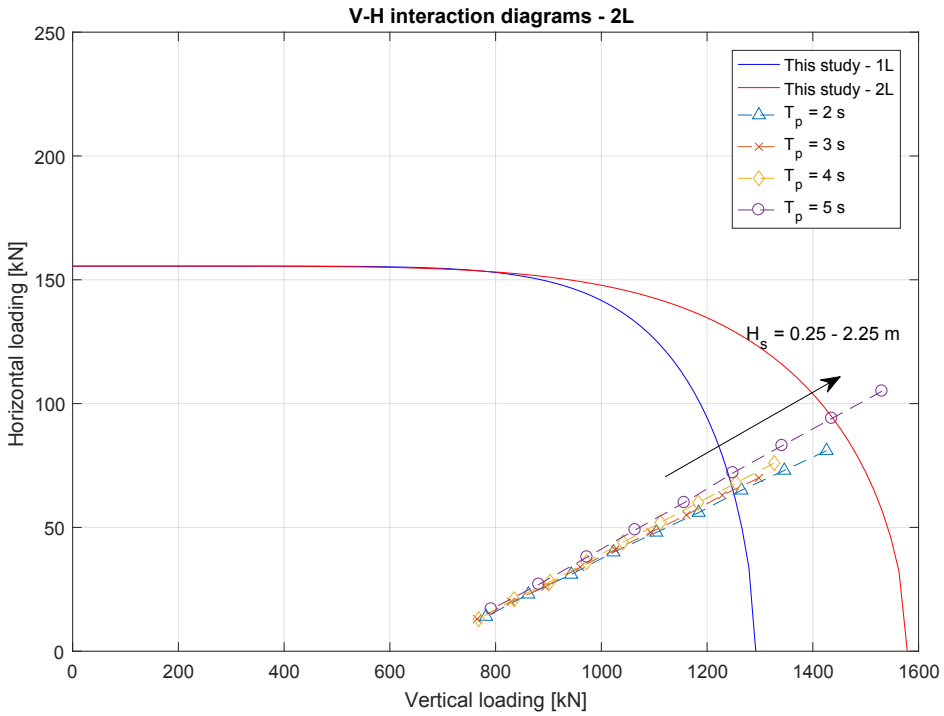

Figure 6.23: Local stability check for the diagonal load case given the failure envelopes for a single and double layer system

6.7. Effect of upper layer thickness on vertical capacity

Important parameters in determining the bearing capacity for double-layered soils are the undrained shear strengths and upper layer thickness of the soils. This study assumes a constant strength over depth for both soil layers while the upper layer thickness is varied. This section shows the effect of the top layer thickness on the vertical bearing capacity.

This study aims to investigate the thickness at which soil failure occurs fully in the upper layer which is called the critical depth. In case of failure in the top layer, the bottom layer does not influence the capacities of the top layer anymore. As thicknesses less than the critical depth occur, enhancement of the capacities at depth or even near the surface might occur allowing for higher operational waves.

Figure 6.24 shows the load-penetration curves derived according to the recommendations of ISO 19901-5 for different upper layer thicknesses varying from 1.0 to 5.0 m. In order to make the comparison, the curve for a single clay layer is included as well.

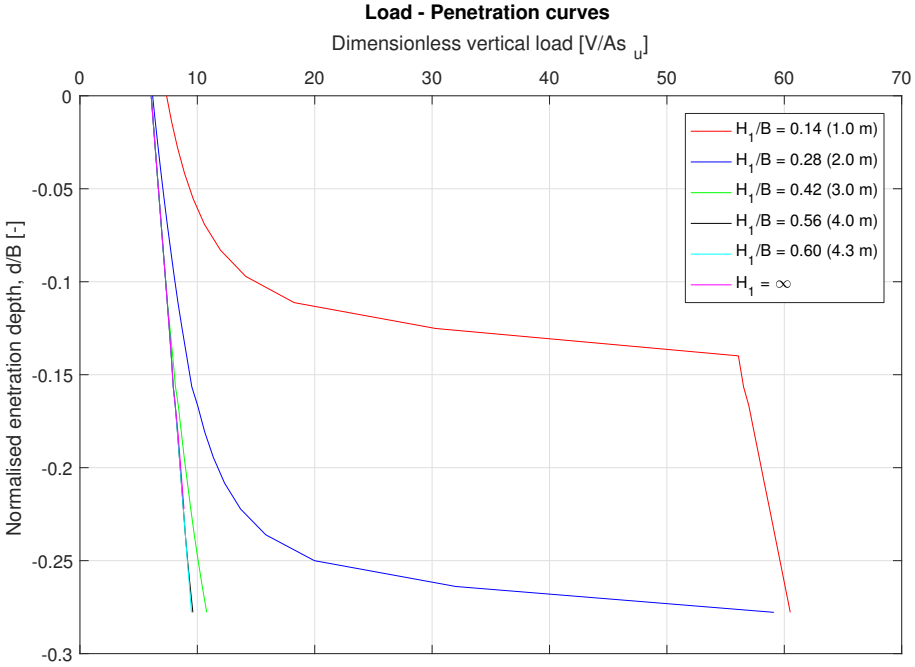

Figure 6.24: Effect of varying the upper layer thickness H_1 on the vertical bearing capacity determined according to ISO 19901-5

Figure 6.24 shows the rapid increase in capacity when approaching the bottom of the top layer as shown for H_1 = 1.0 m. Squeezing of clay is observed for a thickness of 2.0 m as well. For thicknesses larger than 3.0 m, the capacities seem not to be enhanced anymore. With H_1 between 4.0 and 4.3 m, failure occurs fully in the soft soil layer. For H_1 = 1.0 m, an increase of 22 % in capacity near seabed is observed implying that for small top layer thicknesses, capacities near surface may increase as well due to the presence of a bottom layer with sufficient strength.

As the use of the bearing capacity factor in ISO 19901-5 is rather questionable, the critical depth for a double-layered system is investigated with Plaxis 3D as well. The load - penetration curves for varying H_1 from 1.0 to 5.0 m are provided in Figure 6.25.

The results show an enhancement in line with the results from literature for H_1 is 1.0 or 2.0 m. The numerical calculations show that for H_1 = 3.0 m an increase in capacity due to squeezing is obtained as well. The effect of the bottom layer starts to become negligible for thicknesses larger than 3.0 m. An increase in capacity near the seabed is only obtained for H_1 = 1.0 m, which in line with the results from ISO 19901-5. However, there is a significant difference in the amount of increase which is as twice as high.

Concluding, modelling the soil as a single clay layer provides conservative results. The incorporation of a

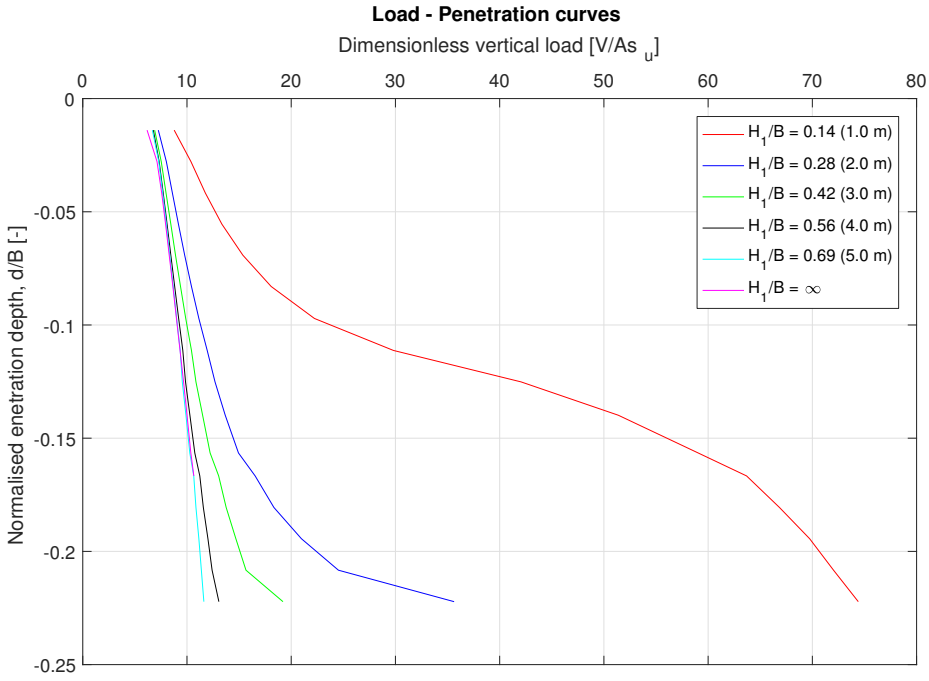

Figure 6.25: Effect of varying the upper layer thickness H_1 on the vertical bearing capacity determined with this study

second stronger layer beneath, if present, is therefore preferable. Higher capacities are not only obtained at depth. Figures 6.24 and 6.25 show the increase in capacities near the seabed with approximately 40 %. The critical depth for the double-layered system with two square footings is found in this study as $H_1/B = 0.69$. In case the upper soil layer is thicker than this critical depth, failure of soil occurs and stays fully in the upper layer. Therefore, the soil can be simplified to a single homogeneous soil layer.

6.8. Summary and discussion

Chapter 6 provides an assessment on the bearing capacity of a double-layered system. The penetration process of the mud mats is modelled with the PR technique based on small deformation analysis rather than large deformation analysis. A Mohr-Coulomb constitutive model is used with coarse mesh to obtain smoother stress distributions and improvement on the calculation time. Additional interface extensions are added to prevent premature failure next to the footing. The coarse mesh increases the discrepancy between the theoretical and numerical bearing capacity factor. The technique consists of step wise application of prescribed displacement and update of the material properties. The problem is continuously changed rather than solving the problem in small steps and did therefore not result in a convergence of the solution.

Load-penetration curves for a single clay layer derived by ISO 19901-5 and the PR technique are compared showing a difference in rate of increase. ISO 19901-5 incorporates the solution for strip footings at surface and provides the capacities for solely plastic failure. Plaxis 3D provides capacities taking into account both the elastic and plastic part. Comparing both methods after preload provided a difference of 11 % which equals almost the numerical inaccuracy of the mesh.

VHM interaction diagrams are derived for square footings at surface for three vertical load ratios showing that the horizontal capacities are not effected until $V/V_{ult} = 0.5$. The failure mechanisms transitions from a scoop failure towards two independent failure mechanisms with rotation and vertical bearing failure with decreasing horizontal loading. The diagrams are also derived for embedded footings showing the significant enhancement for the moment and horizontal capacity. The envelopes for $V/V_{ult} = 0.50$ and 0.75 showed good agreement in normalised space. The envelope for the lower vertical load showed increasing asymmetry, especially in the -H+M plane. A conservative expression is proposed to approximate the capacities in H-M loading plane at surface taking symmetry of the lower part of the failure envelope of $V/V_{ult} = 0.75$ since the load fluctuates in both loading planes. This expression is useful up to 0.20 m depth. For d = 1.0 m, a new symmetrical equation is proposed.

Load-penetration curves are derived for the double-layered system showing to be nicely bounded by the capacities for a single soft clay and glacial till layer. The presence of a stronger bottom layer may influence the capacity at the seabed. Great enhancement is observed for the moment capacity while the horizontal capacities are not affected since sliding mobilises solely soil near the subsurface. More soil mobilisation resulted in the increase of the moment capacity since displacements were not able to enter the bottom layer. Good agreement is found in normalised space for vertical load ratios of 0.25 and 0.75 as the shape for V/V_{ult} = 0.50 starts to deviate in the -H+M loading plane. A conservative expression is proposed taking symmetry of the lower part of the expression for V/V_{ult} = 0.50, which can be used as shape for square mud mats on soft clay resting on top of a stronger till layer. This expression can be used as a conservative approach towards the single layer case. For embedded footings, a new equation is proposed.

The presence of a stronger bottom layer shows to be beneficial for the global stability. The increase in only vertical and moment capacities shows that the presence of the bottom layer is not per se beneficial for the local stability. During high vertical loads on a single mud mat it is indeed of value. However, its benefit diminishes with increasing horizontal load resulting showing that for the horizontal loading case hardly higher waves can be allowed. In the diagonal load case, higher waves can be sustained resulting in a coverage of 6 % of additional waves of the total data set. Since all analyses have been performed under the assumption of quasi-static loading, suggested future should cover the effect of soil strength degradation due to cyclic loading.

Furthermore, the effect of varying the upper layer thickness is investigated. For H_1/B = 0.14, a significant increase is obtained near surface showing the increase of vertical and moment capacity. Up to H_1/B = 0.42 considerable additional capacities are obtained over depth since squeezing is still present. With thicker layers, this effect diminishes whereupon the soil can be modelled as single layer consisting of the upper layer material after H_1/B = 0.69.

7

Conclusions and further research

This study is focused on the investigation of the operability of the Wikinger pre-piling template on soft soil strata. An assessment is made on the main variables involved in this procedure. Raw data is analysed to provide a soil characterisation consisting of a three-layer system. Scarce data was available in order to derive the strength properties of the soft clay layer. Two load cases are defined to determine the environmental loading acting on the piles and template assuming the hydrodynamic loads to be quasi-static. A dynamic analysis is performed to justify this assumption taking into account the frequency dependence of the stiffnesses. The analysis showed the excitation periods not to be close to the natural periods of the system and therefore not resulting in resonance. A parametric study is performed showing that considering a small shear modulus for the spring stiffnesses results in a reduction of shear wave velocity causing the natural periods to increase.

An introduction is given on the failure envelopes, which is a locus describing all load combinations resulting in plastic deformation. Capacities in V-H loading space according to ISO 19901-4 and this study are compared. As combined loading is three-dimensional, capacities are given in H-M loading space with a quasi-constant vertical load. The penetration process of the pre-piling template is modelled using the PR technique. By varying the design waves, the effect of changing the operational limits on the operability of the pre-piling template in terms of on-bottom stability is investigated. The main findings of this work are listed below.

7.1. Assessment of the bearing capacity of a single clay layer

Bearing capacities are presented according to the recommendations by ISO 19901-4 showing that the level of applied preload was not sufficient to deal with the loads of the two load cases resulting in local failure beneath the mud mats. The capacities at surface allowed for waves slightly less than 1.0 m in the horizontal load case and 0.75 m during diagonal irrespective of the peak periods and amount of piles placed. The application of preload created a safe working platform for waves slightly higher than 1.25 m irrespective of the period for the horizontal loading case while waves of almost 1.0 m can be sustained irrespective of the peak period and piles for the diagonal load case. For certain periods up to 0.50 m higher waves can be allowed.

This study showed a significant underestimation in the V-H capacities for square footings with a ZTI on homogeneous soils recommended by ISO 19901-4. Good agreement in ultimate capacities is obtained as well as a sliding mechanism for $V/V_{ult} < 0.5$ in both methods. Deviation starts during combined V-H loading as different envelope shapes are incorporated. The guideline provides a parabola shaped equation, while an ellipse shaped failure envelope is found within this study comparable to [9]. The capacity in V-H loading space of a surface square footing, limited for the conditions considered in this study, can be approximated with Eq. (5.1). Considering the shape found in this study allows for up to 0.50 m higher waves than initially considered. In case of horizontal loading 8 % more waves of the 14 year time series is covered, while during diagonal loading up to 16 % more waves may be covered compared to ISO 19901-4.

7.2. Assessment of the bearing capacity of two clay layers

The interaction diagrams are presented in two-dimensional H-M loading space with a quasi-constant vertical load for a single clay layer showing that the horizontal capacities are not influenced up to V/V_{ult} = 0.5. Asymmetry is observed since the maximum moment capacity occurs with a positive horizontal load. Displacement vectors show that a scoop, combined sliding-rotational, failure mechanism transitions towards two independent mechanisms will decreasing horizontal loading. Capacity diagrams are presented in dimensionless space showing the significant increase in capacity with embedment and preserved within the diagrams. With larger embedment, the maximum horizontal capacity does not coincide anymore with the ultimate horizontal capacity which can be explained since the horizontal load provides resistance to the development of the rotational failure mechanism resulting in the additional capacity. The shapes for V/V_{ult} = 0.50 and 0.75 showed good agreement in normalised space. The shape for V/V_{ult} = 0.25 includes more asymmetry, especially with a negative horizontal load. A conservative fit is proposed for the capacities for all vertical load cases by disregarding the asymmetrical character of the shapes. A new expression is proposed for the largely embedded footings since the embedment influences the shape of the envelope.

The penetration process is modelled using the PR Technique showing an overestimation in the vertical capacity for both the single and double-layered case compared to ISO 19901-5. The difference might arise since the wished-in-place method incorporates the solution for strip footings at surface, which is not derived to take the embedment into account. The curves for the double-layered system show to be nicely bounded by the capacities for a single soft clay and glacial till layer. A parametric study on the top layer thickness showed an increase in capacity near the seabed for thicknesses up to 1.0 m. Squeezing of clay is observed for thicknesses up to 3.0 m resulting in the great increase over depth. The influence of the bottom layer on the capacity of the top layer diminishes for thicknesses larger than 5.0 m whereupon the soil can be modelled as a single layer with the properties of the top layer. This study incorporates the PR technique, which is initially derived for 2D applications with preferring a coarse mesh. The technique changes step wise the problem rather than solving the problem in small steps as large deformation analysis is required for proper modelling of the penetration process. As the wished-in-place method provides capacities for solely plastic deformation and this study for both elastic and plastic deformations, this might explain the differences in the load-penetration curves obtained for both methods.

The presence of the bottom soil layer provides solely an increase in vertical and moment capacities. The horizontal capacity is not enhanced since the strength at the seabed is of importance. Failure mechanisms showed that displacements were not able to enter the bottom layer. By expansion of the mechanisms to the breadth, more soil mobilisation is realised resulting in the increase of vertical and moment capacities. The shapes of the envelopes fall together in the +H+M plane but the envelope for V/V_{ult} = 0.5 start diverging in the -H+M plane. By neglecting the asymmetry in the shapes since loading is fluctuating in both loading plane, a conservative fit is proposed, which can be used to construct the failure envelopes for square footings on surface resting on a double-layered system for the conditions assumed in this study. This expression is shown to be a conservative approach towards the single layer case as well. A new conservative expression is derived for square footings at larger depths.

The increase in vertical and moment capacities are found beneficial for the global stability of the pre-piling template. When large vertical loads are involved as in case of the diagonal load case, the presence of the bottom layer might be beneficial as well since up to 0.50 m higher operational waves can be allowed. This resulted in a coverage of only 6 % of additional waves in the data set. However, with increasing horizontal loads, the benefit of the bottom layer starts to decline as no additional horizontal capacities are obtained. The presence of the bottom layer may therefore be beneficial for the local stability if operational limits are considered separately for the different loading cases. All analyses have been performed under the assumption of quasi-static loading. Suggested future should cover the effect of soil strength degradation due to cyclic loading.

7.3. Recommendations for further research

In order to extend the assessment of the variables for the operability of the pre-piling template in soft soil strata, the following is recommended:

- Analyses have been performed with a Mohr-Coulomb constitutive model known for its simplicity and

its ability to provide a first approximation. A more advanced constitutive soil model can be incorporated to consider the effect of unloading and reloading on the capacities.

- In the study, all the analyses have been performed assuming the hydrodynamic load to be of quasi-static character. Reality shows that wave loading is of cyclic character resulting in the degradation of the soil strength over time. Suggested future work should cover the effect of strength degradation on the allowable operational limits.
- Performing stochastic analysis for the investigation of the probability of occurrence of the individual parameters.
- During the execution of a project, the settlements of the structure used has to be logged properly with the present metocean conditions (H_s, T_p). This way, results of a study may be verified and tuned with data from the field.
- The interaction diagrams are applicable for the geometry and conditions used in this study. Parametric study might be carried out to obtain interaction diagrams for different soil profiles, strength profiles and geometries, which are of interest.

Appendices

A

Metocean data

H_{m0} [m]	dir^{o} [Deg] 345−15	15−45	45−75	75−105	105−135	135−165	165−195	195−225	225−255	255−285	285−315	315−345	Total [%]
0−0.25	0.85%	0.90%	2.60%	2.06%	0.70%	0.54%	0.54%	0.49%	0.67%	2.23%	1.35%	0.65%	13.58%
0.25−0.5	0.71%	1.16%	2.48%	2.46%	2.04%	1.73%	1.86%	1.45%	2.10%	3.56%	2.21%	0.98%	22.75%
0.5−0.75	0.70%	1.03%	1.87%	2.53%	1.62%	1.61%	1.71%	1.42%	2.13%	3.85%	2.01%	0.88%	21.36%
0.75−1	0.42%	0.68%	1.24%	1.41%	1.03%	0.83%	1.23%	0.88%	1.64%	3.04%	1.39%	0.44%	14.25%
1−1.25	0.22%	0.50%	0.87%	0.96%	0.63%	0.56%	0.63%	0.66%	1.37%	2.33%	0.92%	0.32%	9.96%
1.25−1.5	0.14%	0.31%	0.58%	0.60%	0.32%	0.33%	0.32%	0.41%	1.05%	1.77%	0.58%	0.15%	6.57%
1.5−1.75	0.10%	0.21%	0.43%	0.28%	0.24%	0.21%	0.16%	0.26%	0.71%	1.34%	0.44%	0.08%	4.46%
1.75−2	0.03%	0.09%	0.17%	0.16%	0.07%	0.08%	0.08%	0.17%	0.47%	0.98%	0.24%	0.05%	2.58%
2−2.25	0.02%	0.06%	0.06%	0.09%	0.07%	0.07%	0.06%	0.09%	0.33%	0.69%	0.18%	0.02%	1.73%
2.25−2.5	0.00%	0.04%	0.03%	0.02%	0.04%	0.02%	0.02%	0.04%	0.20%	0.49%	0.12%	0.01%	1.05%
2.5−2.75	0.01%	0.03%	0.02%	0.00%	0.02%	0.01%	0.01%	0.01%	0.12%	0.32%	0.09%	0.01%	0.67%
2.75−3	0.00%	0.04%	0.02%	0.00%	0.01%	0.00%	0.01%	0.01%	0.08%	0.21%	0.05%	0.00%	0.43%
3−3.25	0%	0.00%	0.01%	0.00%	0%	0.00%	0.01%	0.01%	0.04%	0.14%	0.03%	0%	0.24%
3.25−3.5	0%	0.01%	0.01%	0%	0%	0%	0.00%	0.01%	0.03%	0.09%	0.03%	0%	0.17%
3.5−3.75	0%	0.00%	0%	0%	0%	0%	0.00%	0.00%	0.01%	0.06%	0.01%	0%	0.08%
3.75−4	0%	0.00%	0%	0%	0%	0%	0.00%	0%	0.01%	0.04%	0.01%	0%	0.05%
4−4.25	0%	0.00%	0%	0%	0%	0%	0%	0.00%	0.00%	0.02%	0.00%	0%	0.03%
4.25−4.5	0%	0.00%	0%	0%	0%	0%	0%	0.00%	0.00%	0.01%	0.00%	0%	0.02%
4.5−4.75	0%	0%	0%	0%	0%	0%	0%	0%	0.00%	0.01%	0.00%	0%	0.01%
4.75−5	0%	0%	0%	0%	0%	0%	0%	0%	0.00%	0.01%	0.00%	0%	0.01%
5−5.25	0%	0%	0%	0%	0%	0%	0%	0%	0%	0.01%	0%	0%	0.01%
5.25−5.5	0%	0%	0%	0%	0%	0%	0%	0%	0%	0%	0.00%	0%	0.00%
5.5−5.75	0%	0%	0%	0%	0%	0%	0%	0%	0%	0%	0%	0%	0.00%
5.75−6	0%	0%	0%	0%	0%	0%	0%	0%	0%	0%	0%	0%	0.00%
>6	0%	0%	0%	0%	0%	0%	0%	0%	0%	0%	0%	0%	0.00%
Total [%]	3.19%	5.06%	10.37%	10.59%	6.79%	5.99%	6.65%	5.93%	10.96%	21.18%	9.68%	3.60%	100.0%

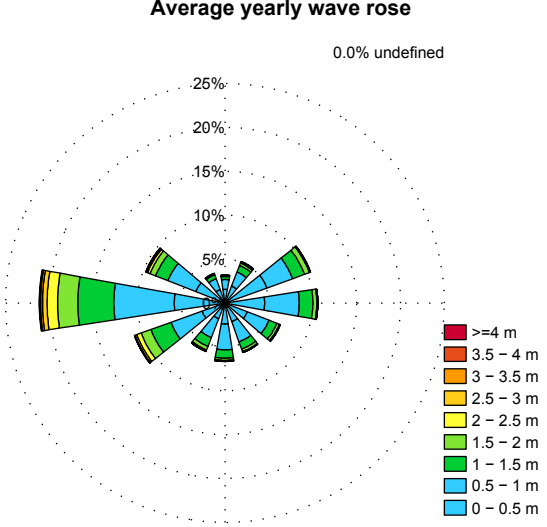

Offshore wave data

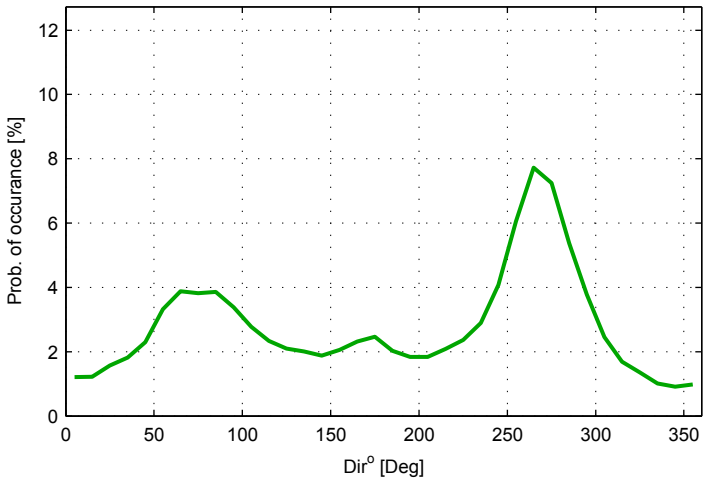

Data over a Year

	T_p [Sec]											
H_{m0} [m]	0−1	1−2	2−3	3−4	4−5	5−6	6−7	7−8	8−9	9−10	>10	Total [%]
0−0.25	0.34%	0.76%	6.11%	4.44%	1.32%	0.41%	0.15%	0.03%	0.01%	0.00%	0%	13.58%
0.25−0.5	0%	0.04%	4.95%	14.49%	1.96%	0.81%	0.43%	0.07%	0.00%	0%	0%	22.75%
0.5−0.75	0%	0%	0.11%	14.65%	5.57%	0.55%	0.36%	0.10%	0.01%	0.00%	0%	21.36%
0.75−1	0%	0%	0%	2.05%	11.08%	0.83%	0.20%	0.07%	0.01%	0.00%	0%	14.25%
1−1.25	0%	0%	0%	0.02%	7.65%	2.16%	0.10%	0.02%	0.00%	0.00%	0%	9.96%
1.25−1.5	0%	0%	0%	0%	1.60%	4.84%	0.11%	0.01%	0.00%	0%	0%	6.57%
1.5−1.75	0%	0%	0%	0%	0.07%	4.09%	0.29%	0.01%	0.00%	0%	0%	4.46%
1.75−2	0%	0%	0%	0%	0.00%	1.94%	0.64%	0.01%	0.00%	0%	0%	2.58%
2−2.25	0%	0%	0%	0%	0%	0.55%	1.16%	0.02%	0.00%	0%	0%	1.73%
2.25−2.5	0%	0%	0%	0%	0%	0.04%	0.98%	0.02%	0.00%	0%	0%	1.05%
2.5−2.75	0%	0%	0%	0%	0%	0.00%	0.61%	0.05%	0%	0%	0%	0.67%
2.75−3	0%	0%	0%	0%	0%	0.00%	0.33%	0.10%	0.00%	0%	0%	0.43%
3−3.25	0%	0%	0%	0%	0%	0.00%	0.10%	0.14%	0%	0%	0%	0.24%
3.25−3.5	0%	0%	0%	0%	0%	0%	0.02%	0.15%	0%	0%	0%	0.17%
3.5−3.75	0%	0%	0%	0%	0%	0%	0.00%	0.08%	0%	0%	0%	0.08%
3.75−4	0%	0%	0%	0%	0%	0%	0.00%	0.05%	0.00%	0%	0%	0.05%
4−4.25	0%	0%	0%	0%	0%	0%	0%	0.02%	0.01%	0%	0%	0.03%
4.25−4.5	0%	0%	0%	0%	0%	0%	0%	0.01%	0.01%	0%	0%	0.02%
4.5−4.75	0%	0%	0%	0%	0%	0%	0%	0.00%	0.01%	0%	0%	0.01%
4.75−5	0%	0%	0%	0%	0%	0%	0%	0%	0.01%	0%	0%	0.01%
5−5.25	0%	0%	0%	0%	0%	0%	0%	0%	0.01%	0%	0%	0.01%
5.25−5.5	0%	0%	0%	0%	0%	0%	0%	0%	0.00%	0%	0%	0.00%
5.5−5.75	0%	0%	0%	0%	0%	0%	0%	0%	0%	0%	0%	0%
5.75−6	0%	0%	0%	0%	0%	0%	0%	0%	0%	0%	0%	0%
>6	0%	0%	0%	0%	0%	0%	0%	0%	0%	0%	0%	0%
Total [%]	0.34%	0.81%	11.18%	35.65%	29.24%	16.23%	5.50%	0.95%	0.09%	0.01%	0%	100.0%

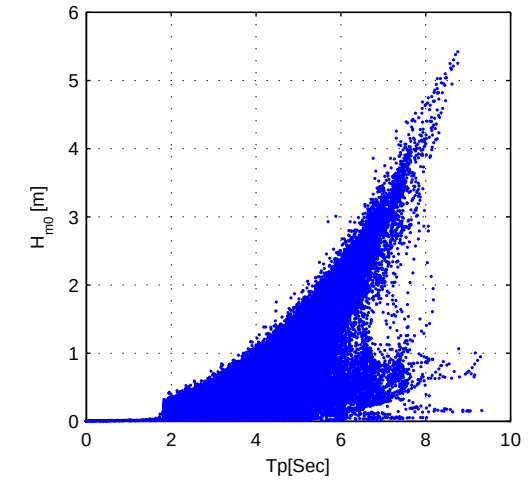

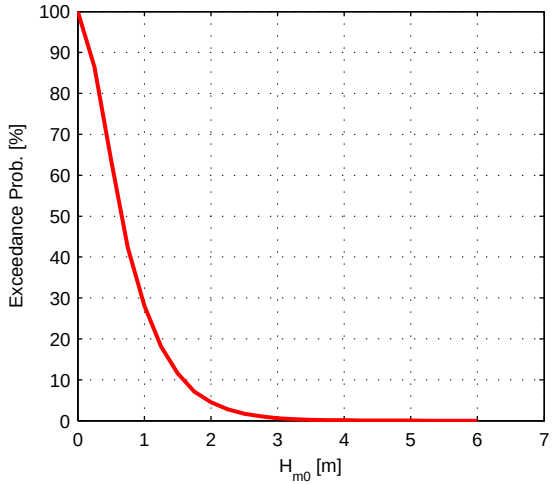

Data over a Year

	Wind speed [m/s]																			
H_{m0} [m]	0−1	1−2	2−3	3−4	4−5	5−6	6−7	7−8	8−9	9−10	10−11	11−12	12−13	13−14	14−15	15−16	16−17	17−18	>18	Total [%]
0−0.25	0.81%	2.24%	3.26%	2.84%	1.65%	0.94%	0.54%	0.39%	0.28%	0.21%	0.15%	0.11%	0.06%	0.04%	0.03%	0.01%	0.01%	0.01%	0.01%	13.58%
0.25−0.5	0.27%	1.07%	2.41%	4.47%	5.98%	4.85%	2.15%	0.69%	0.32%	0.18%	0.13%	0.10%	0.05%	0.05%	0.02%	0.01%	0.00%	0.00%	0.01%	22.75%
0.5−0.75	0.04%	0.13%	0.33%	0.79%	2.00%	4.68%	7.13%	4.67%	1.08%	0.25%	0.09%	0.07%	0.04%	0.03%	0.02%	0.00%	0%	0.00%	0.00%	21.36%
0.75−1	0.01%	0.05%	0.05%	0.10%	0.22%	0.58%	1.73%	4.67%	4.81%	1.63%	0.29%	0.06%	0.02%	0.01%	0.00%	0%	0.00%	0.00%	0%	14.25%
1−1.25	0.00%	0.01%	0.01%	0.02%	0.03%	0.07%	0.22%	0.81%	2.68%	4.03%	1.74%	0.29%	0.04%	0.01%	0.00%	0.00%	0.00%	0%	0.00%	9.96%
1.25−1.5	0%	0.00%	0.00%	0.01%	0.01%	0.02%	0.02%	0.09%	0.41%	1.53%	2.83%	1.33%	0.25%	0.05%	0.01%	0.00%	0.00%	0%	0%	6.57%
1.5−1.75	0%	0.00%	0.00%	0%	0.00%	0.01%	0.01%	0.01%	0.04%	0.22%	0.99%	1.96%	1.01%	0.18%	0.02%	0.01%	0.00%	0.00%	0.00%	4.46%
1.75−2	0%	0%	0%	0%	0.00%	0.00%	0.00%	0.00%	0.00%	0.02%	0.11%	0.53%	1.14%	0.63%	0.12%	0.02%	0.00%	0.00%	0%	2.58%
2−2.25	0%	0%	0%	0%	0%	0%	0%	0%	0%	0.00%	0.01%	0.08%	0.37%	0.76%	0.44%	0.06%	0.01%	0.00%	0.00%	1.73%
2.25−2.5	0%	0%	0%	0%	0%	0%	0%	0%	0%	0%	0.00%	0.00%	0.04%	0.26%	0.48%	0.21%	0.04%	0.00%	0.00%	1.05%
2.5−2.75	0%	0%	0%	0%	0%	0%	0%	0%	0%	0%	0%	0.00%	0.00%	0.04%	0.20%	0.29%	0.11%	0.02%	0.00%	0.67%
2.75−3	0%	0%	0%	0%	0%	0%	0%	0%	0%	0%	0%	0%	0%	0.01%	0.04%	0.14%	0.19%	0.05%	0.01%	0.43%
3−3.25	0%	0%	0%	0%	0%	0%	0%	0%	0%	0%	0%	0%	0%	0.00%	0.00%	0.02%	0.10%	0.09%	0.02%	0.24%
3.25−3.5	0%	0%	0%	0%	0%	0%	0%	0%	0%	0%	0%	0%	0%	0%	0%	0.01%	0.02%	0.08%	0.06%	0.17%
3.5−3.75	0%	0%	0%	0%	0%	0%	0%	0%	0%	0%	0%	0%	0%	0%	0%	0%	0.00%	0.02%	0.06%	0.08%
3.75−4	0%	0%	0%	0%	0%	0%	0%	0%	0%	0%	0%	0%	0%	0%	0%	0%	0%	0.00%	0.05%	0.05%
4−4.25	0%	0%	0%	0%	0%	0%	0%	0%	0%	0%	0%	0%	0%	0%	0%	0%	0%	0%	0.03%	0.03%
4.25−4.5	0%	0%	0%	0%	0%	0%	0%	0%	0%	0%	0%	0%	0%	0%	0%	0%	0%	0%	0.02%	0.02%
4.5−4.75	0%	0%	0%	0%	0%	0%	0%	0%	0%	0%	0%	0%	0%	0%	0%	0%	0%	0%	0.01%	0.01%
4.75−5	0%	0%	0%	0%	0%	0%	0%	0%	0%	0%	0%	0%	0%	0%	0%	0%	0%	0%	0.01%	0.01%
5−5.25	0%	0%	0%	0%	0%	0%	0%	0%	0%	0%	0%	0%	0%	0%	0%	0%	0%	0%	0.01%	0.01%
5.25−5.5	0%	0%	0%	0%	0%	0%	0%	0%	0%	0%	0%	0%	0%	0%	0%	0%	0%	0%	0.00%	0.00%
5.5−5.75	0%	0%	0%	0%	0%	0%	0%	0%	0%	0%	0%	0%	0%	0%	0%	0%	0%	0%	0%	0%
5.75−6	0%	0%	0%	0%	0%	0%	0%	0%	0%	0%	0%	0%	0%	0%	0%	0%	0%	0%	0%	0%
>6	0%	0%	0%	0%	0%	0%	0%	0%	0%	0%	0%	0%	0%	0%	0%	0%	0%	0%	0%	0%
Total [%]	1.13%	3.50%	6.08%	8.22%	9.89%	11.15%	11.79%	11.34%	9.61%	8.07%	6.35%	4.54%	3.03%	2.04%	1.40%	0.78%	0.49%	0.27%	0.31%	100.0%

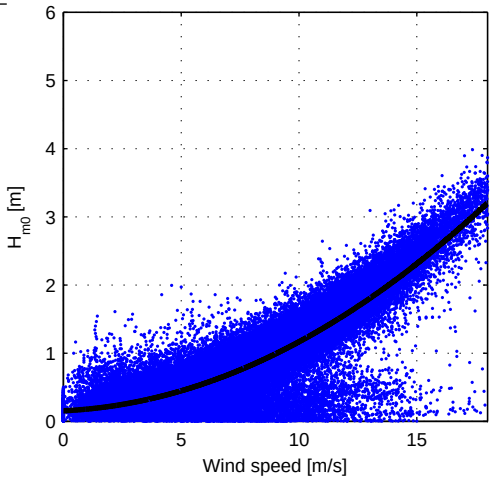

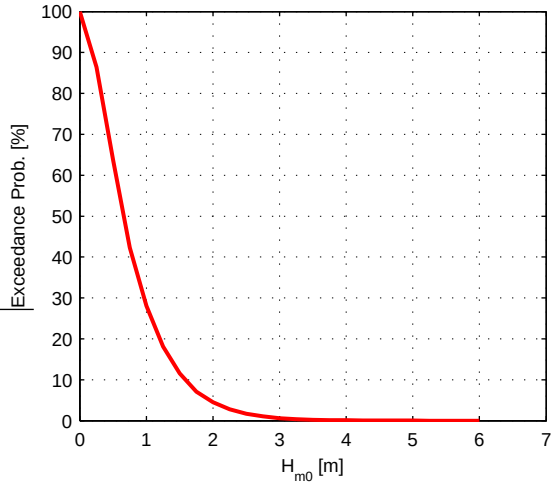

Data over a Year

	Wind speed [m/s]																			
T_p [Sec]	0−1	1−2	2−3	3−4	4−5	5−6	6−7	7−8	8−9	9−10	10−11	11−12	12−13	13−14	14−15	15−16	16−17	17−18	>18	Total [%]
0−1	0.10%	0.01%	0.01%	0.02%	0.02%	0.03%	0.03%	0.02%	0.03%	0.03%	0.01%	0.01%	0.01%	0.01%	0.00%	0.00%	0%	0%	0%	0.34%
1−2	0.03%	0.04%	0.07%	0.11%	0.14%	0.15%	0.09%	0.06%	0.03%	0.03%	0.03%	0.01%	0.01%	0.00%	0.00%	0%	0%	0%	0%	0.81%
2−3	0.30%	0.92%	1.54%	1.96%	2.21%	1.76%	1.07%	0.60%	0.31%	0.19%	0.14%	0.09%	0.05%	0.03%	0.01%	0.01%	0.00%	0.00%	0.01%	11.18%
3−4	0.40%	1.55%	2.77%	4.03%	5.31%	6.55%	6.66%	4.77%	2.09%	0.76%	0.33%	0.19%	0.08%	0.07%	0.04%	0.01%	0.01%	0.01%	0.01%	35.65%
4−5	0.14%	0.56%	0.99%	1.31%	1.49%	2.01%	3.24%	5.06%	5.78%	4.84%	2.56%	0.86%	0.27%	0.08%	0.03%	0.01%	0.01%	0.00%	0.00%	29.24%
5−6	0.09%	0.24%	0.39%	0.47%	0.43%	0.44%	0.55%	0.72%	1.28%	2.08%	3.04%	3.00%	2.01%	0.97%	0.38%	0.10%	0.03%	0.01%	0.00%	16.23%
6−7	0.05%	0.14%	0.25%	0.25%	0.22%	0.16%	0.13%	0.08%	0.08%	0.13%	0.25%	0.37%	0.58%	0.84%	0.87%	0.58%	0.34%	0.12%	0.05%	5.50%
7−8	0.02%	0.05%	0.05%	0.04%	0.05%	0.05%	0.03%	0.01%	0.01%	0.01%	0.01%	0.01%	0.02%	0.04%	0.06%	0.08%	0.11%	0.14%	0.18%	0.95%
8−9	0%	0.00%	0.01%	0.01%	0.01%	0.01%	0.00%	0.00%	0.00%	0.00%	0%	0.00%	0.00%	0.00%	0.00%	0%	0%	0.00%	0.05%	0.09%
9−10	0%	0%	0.00%	0.00%	0.00%	0.00%	0.00%	0.00%	0%	0%	0%	0%	0%	0%	0%	0%	0%	0%	0%	0.01%
>10	0%	0%	0%	0%	0%	0%	0%	0%	0%	0%	0%	0%	0%	0%	0%	0%	0%	0%	0%	0%
Total [%]	1.13%	3.50%	6.08%	8.22%	9.89%	11.15%	11.79%	11.34%	9.61%	8.07%	6.35%	4.54%	3.03%	2.04%	1.40%	0.78%	0.49%	0.27%	0.31%	100.0%

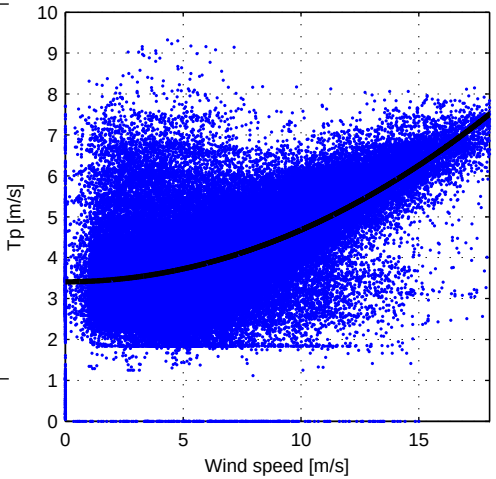

Data over a Year

B

Pre-Piling Template structural drawings

FABRICATION NOTES

1. THE FOLLOWING NOTES APPLY EXCEPT WHERE OTHERWISE DETAILED ON THE DRAWING.
2. MATERIAL U.O.S: ALL HOLLOW SECTION TO A MINIMUM OF EN10210 S355J2H AND ALL PLATE TO EN 10025:S355J2+N.
3. FOR TOLERANCES SEE STANDARD BORDER NOTES U.O.S.
4. PLATES ARE DETAILED ON SEPERATE DRAWINGS.
5. WELDS ARE TO BE FULLY SEALED WITH WELDS
6. U.O.S. ALL WELDS ARE SINGLE PASS FILLET WELDS, MINIMUM THROAT THICKNESS (a) 6mm.
7. NO WEAVING PERMITTED. WELDS GREATER THAN 6mm THROAT ARE TO BE BUILT UP WITH STRINGER BEADS.
8. WELDERS ARE TO BE CODED AS A MINIMUM TO BS EN 287 -1 : 2011.
9. WELDING CONSUMABLE YIELD STRENGTH TO BE A MINIMUM OF 420MPa.
10. WELD DETAIL AND TESTING TO BE IN ACCORDANCE WITH EN10901-2:2008A1:2011, EXECUTION CLASS 3 AND ISO 3834-2:2006 AND VSF NDT PLAN- DOCUMENT NO. W15-027-80.4
    - 10.1. VISUAL CHECK 100%.
    - 10.2. PRIMARY FULL PEN WELDS TO BE 100% UT TESTED.
    - 10.3. SECONDARY FULL PEN WELDS TO BE 100% UT TESTED.
    - 10.4. LIFT POINT WELDS TO BE 100% UT TESTED OR IF FILLET WELDS TO BE100% MT TESTED.
    - 10.5. FILLET WELDS TO BE 100% MT (MPI) TESTED.
11. LIFT POINTS AND PAD EYES.
    - 11.1. LIFT POINTS ARE CLEARLY INDICATED WITH A SWL.
    - 11.2. SWL TO BE HARD STAMPED ADJACENT TO THE EYE, 10mm HIGH TEXT MIN.
12. FABRICATION TO BE IN ACCORDANCE WITH DNV REQUIREMENTS FOR CERTIFICATION
13. TO BE SET UP IN CONJUNCTION WITH THE TOWERS IN ORDER TO ENSURE DOWEL LOCATION, FABRICATION ALIGNMENT AND OVERALL TOWER CENTRE TO CENTRE TOLERANCE IN LINE WITH DRAWING A1000-0173

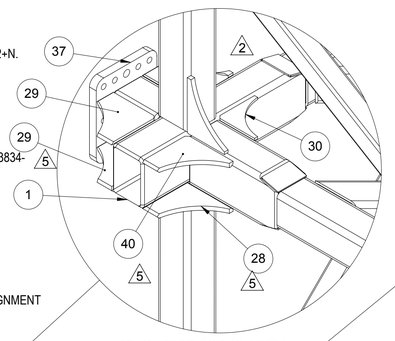

37 OMITTED FOR CLARITY

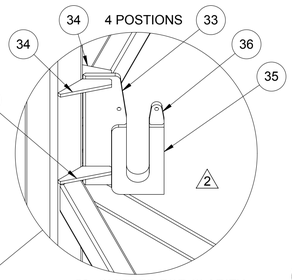

20 OMITTED FOR CLARITY

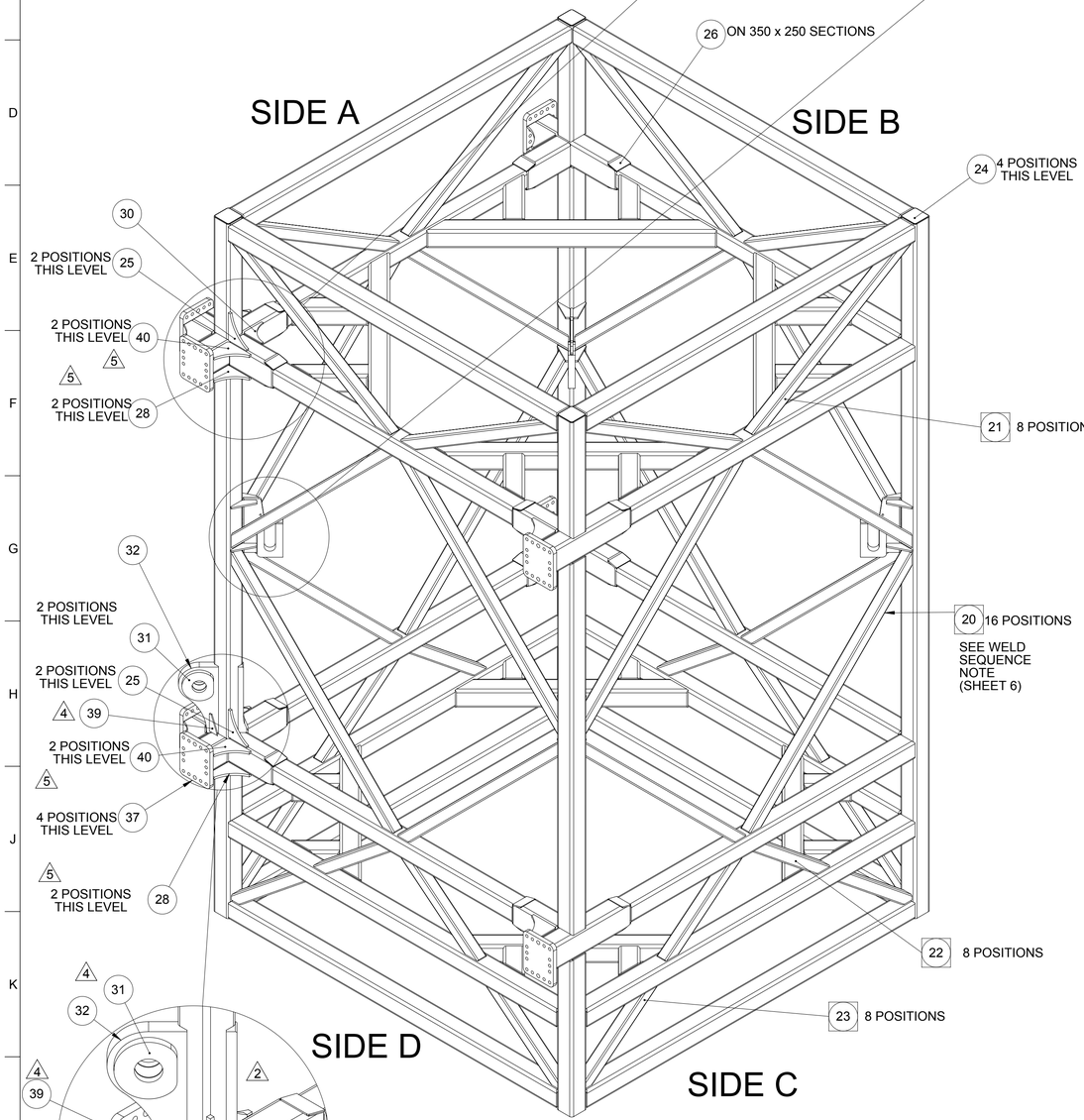

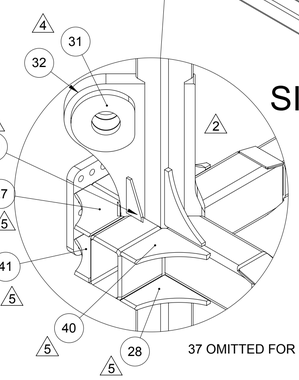

37 OMITTED FOR CLARITY

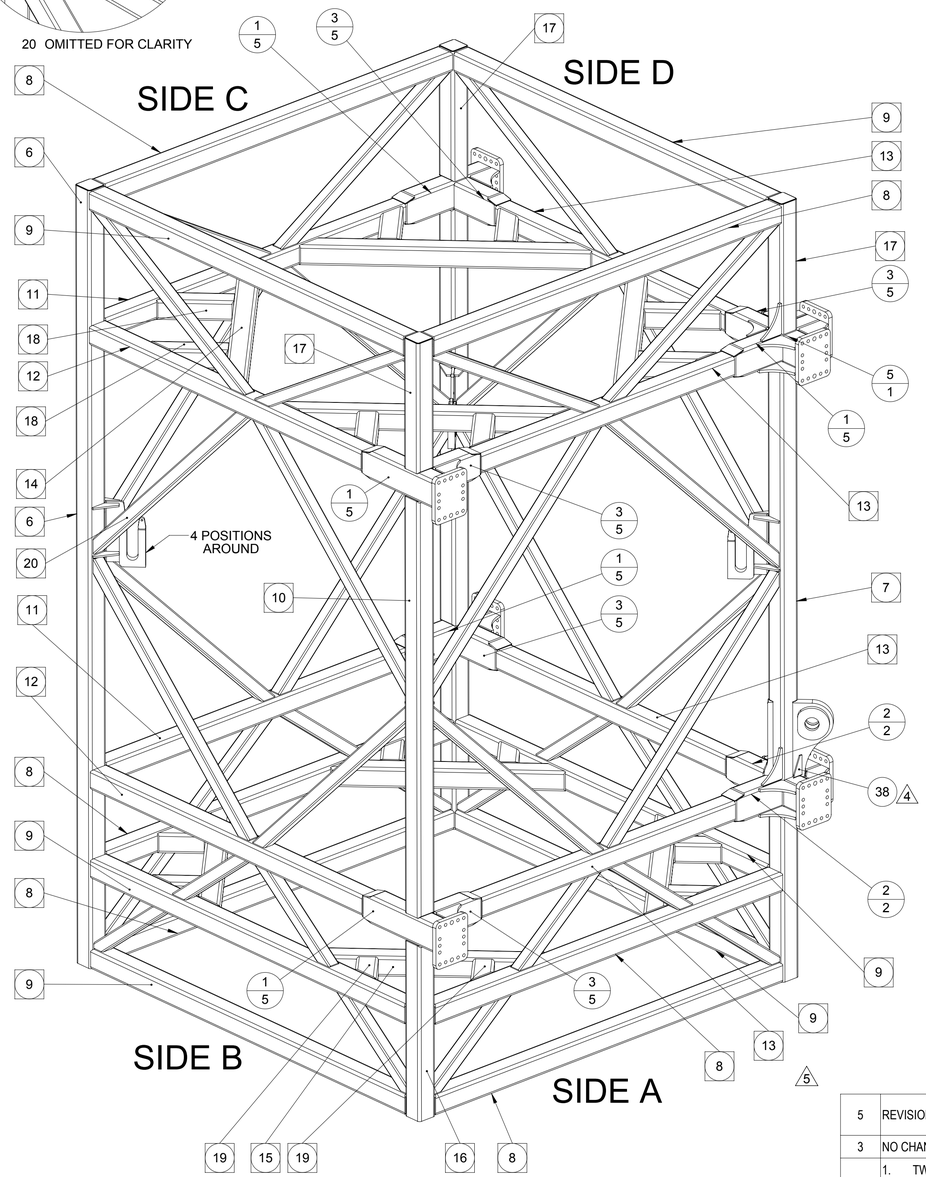

PART NO.	ITEM NO.	QTY.	DESCRIPTION	LENGTH PER ITEM	
A1000-00185-1	1	5	350 x 250 x 16.0	1332	
A1000-00185-2	2	2	350 x 250 x 16.0	717	
A1000-00185-3	3	5	350 x 250 x 16.0	717	
A1000-00185-4	4	2	350 x 250 x 16.0	357	
A1000-00185-5	5	1	350 x 250 x 16.0	357	
A1000-00185-6	6	1	250 x 250 x 16.0	9800	
A1000-00185-7	7	1	250 x 250 x 16.0	7810	
A1000-00185-8	8	6	250 x 250 x 16.0	5350	
A1000-00185-9	9	6	250 x 250 x 16.0	5350	
A1000-00185-10	10	2	250 x 250 x 16.0	5250	
A1000-00185-11	11	2	250 x 250 x 16.0	4625	
A1000-00185-12	12	2	250 x 250 x 16.0	4625	
A1000-00185-13	13	4	250 x 250 x 16.0	3900	
A1000-00185-14	14	4	250 x 250 x 16.0	3346	
A1000-00185-15	15	4	250 x 250 x 16.0	2686	
A1000-00185-16	16	2	250 x 250 x 16.0	2210	
A1000-00185-17	17	3	250 x 250 x 16.0	1640	
A1000-00185-18	18	8	250 x 250 x 16.0	883	
A1000-00185-19	19	8	250 x 250 x 16.0	553	
A1000-00185-20	20	16	150 x 150 x 8.0	3739	
A1000-00185-21	21	8	150 x 150 x 8.0	2968	
A1000-00185-22	22	8	150 x 150 x 8.0	1552	
A1000-00185-23	23	8	150 x 150 x 8.0	1524	
A1000-00185-24	24	4	6mm PLATE		
A1000-00185-25	25	4	30mm PLATE		
A1000-00185-26	26	24	8mm PLATE		
A1000-00185-27	27	1	30mm PLATE		
A1000-00185-28	28	8	30mm PLATE		
A1000-00185-29	29	2	30mm PLATE		
A1000-00185-30	30	1	15mm PLATE		
A1000-00185-31	31	2	50mm PLATE		
A1000-00185-32	32	1	100mm PLATE		
A1000-00185-33	33	4	30mm PLATE		
A1000-00185-34	34	16	20mm PLATE		
A1000-00185-35	35	4	80mm PLATE		
A1000-00185-36	36	4	30mm PLATE		
A1000-00185-37	37	8	60MM PLATE		
A1000-00185-38	38	1	15mm PLATE		4
A1000-00185-39	39	1	15mm PLATE		4
A1000-00185-40	40	8	30mm PLATE		5
A1000-00185-41	41	1	30mm PLATE		5

REV.	DESCRIPTION	DATE	INITIALS
5	REVISION ACCORDING TO VSF ENGINEERING	23/09/2015	AF
3	NO CHANGE	18/09/2015	ML
2	1. TWO SHEETS ADDED AND SHEETS RE-ORDERED. 2. WELD SYMBOLS CHANGED ON SHEET4-5 3. ITEM 31 THICKNESS INCREASED TO 50mm 4. ITEMS 32 TO 35 ADDED. SEE ADDITIONAL SHEETS 6 AND 7 FOR DETAILS. SEE NOTE ON SHEET 6 REGARDING THE FABRICATION SEQUENCE 5. TOLERANCE CHANGED ON BOLTING PLATES	25/08/2015	DW
1	FIRST RELEASE		

REVISIONS

3rd ANGLE PROJECTION

STEEL DETAILS NOT DIMENSIONED OR TOLERANCED ON DRAWING TO BE IN ACCORDANCE WITH BS EN 1090-2:2008+A1:2011

ALL DIMS IN mm U.O.S | DO NOT SCALE

GENERAL FABRICATION TOLERANCE IN ACCORDANCE WITH TABLE D2.7 ANNEX D OF EN1090-2
REMOVE ALL BURS AND SHARP EDGES P1

GENERAL MACHINING TOLERANCES
0 ±2.0 0.00 +0.3
0.0 ±1.0 ANGULAR ±0.5°
SURFACE FINISH 3.2µm Ra MIN
REMOVE ALL BURS AND SHARP EDGES 0.3 MAX
UNSPECIFIED TOOL RADS R0.8

MATERIAL TYPE	SEE DRAWING	EST MASS 26292.81kg	DATE 10/08/2015
MATERIAL SPEC	SEE DRAWING	SHEET 1 OF 10	DRAWN RM
FINISH	SEE DRAWING	A1 SHEET	CHECKED DJ

LARGE DIAMETER DRILLING LTD.
KERREK HOUSE
TOLVADDON BUSINESS PARK
CAMBORNE, CORNWALL
TR14 0HZ
TEL: 01209 861930
FAX: 01209 861110

DESCRIPTION: TOWER STAGE 1 PRIMARY WELDMENT

DRAWING NUMBER: A1000-00185

REV: 05

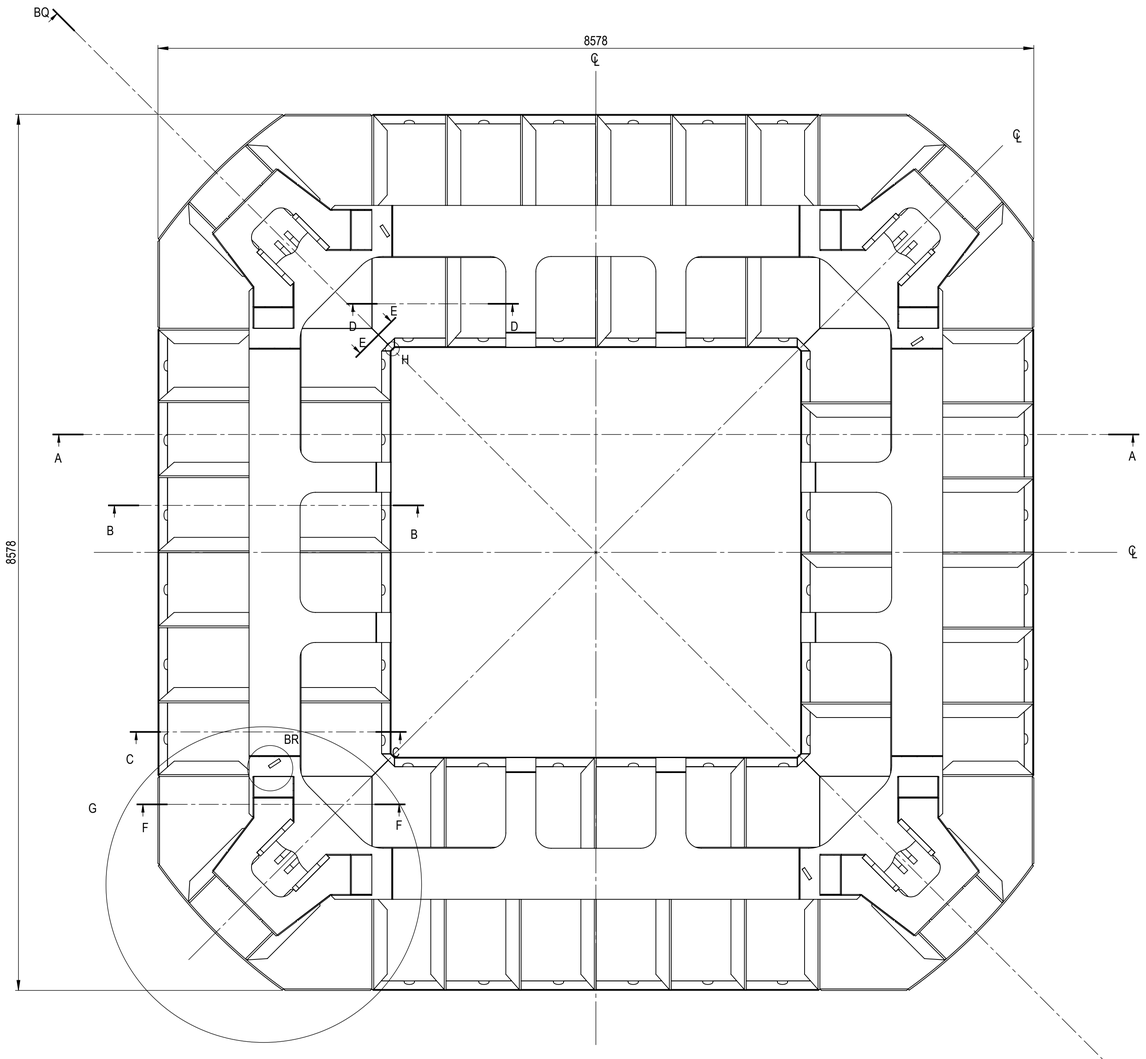

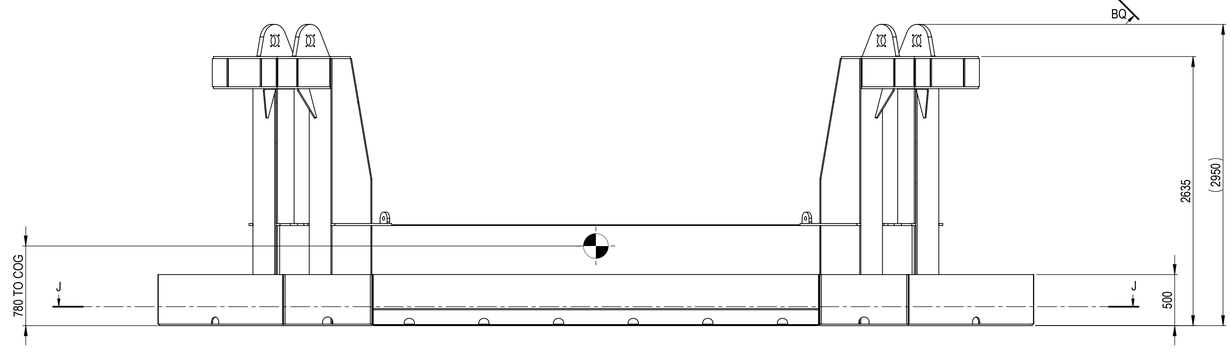

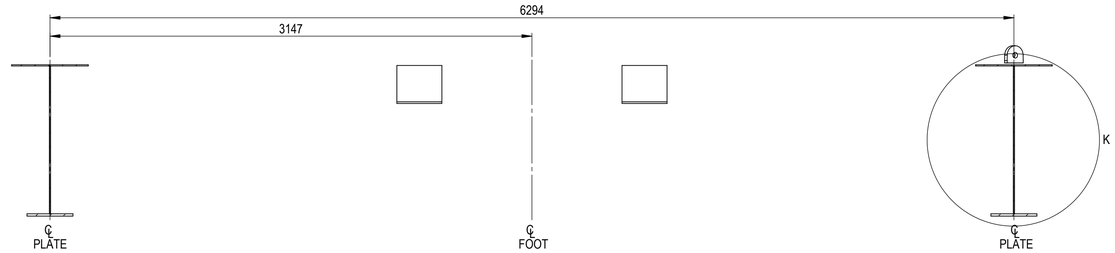

SECTION A-A
SHOWING SET OUT OF MAIN BEAMS
@D1 SHT 1

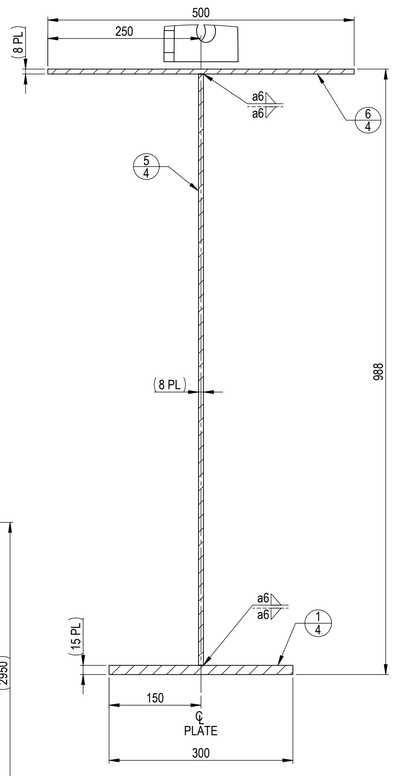

DETAIL K
@C15 SHT1

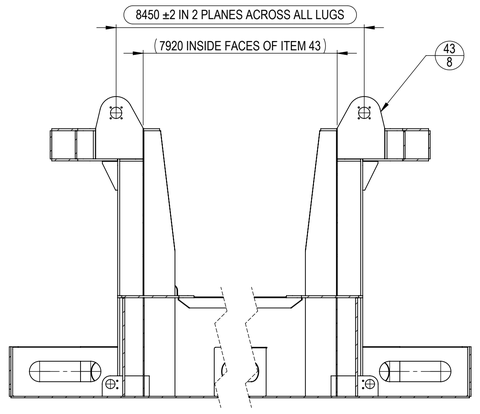

SECTION BQ-BQ

REV.	DESCRIPTION	DATE	INITIALS
1	FIRST RELEASE	N/A	N/A

REVISIONS

3rd ANGLE PROJECTION

STEEL DETAILS NOT DIMENSIONED OR TOLERANCED ON DRAWING TO BE IN ACCORDANCE WITH BS EN 1090-2:2008+A1:2011

ALL DIMS IN mm U.O.S | DO NOT SCALE

GENERAL FABRICATION TOLERANCES
UP TO 1000 ±1.0
OVER 1000 UP TO 5000 ±2.0
OVER 5000 ±5.0
ANGULAR ±0.5
REMOVE ALL BURS AND SHARP EDGES 1.0 MAX

GENERAL MACHINING TOLERANCES
0 ±2.0 0.00 ±0.3
0.0 ±1.0 ANGULAR ±0.5°
SURFACE FINISH 3.2µm Ra MIN
REMOVE ALL BURS AND SHARP EDGES 0.3 MAX
UNSPECIFIED TOOL RADS R0.8

MATERIAL TYPE: N/A
MATERIAL SPEC: N/A
FINISH: PAINT IN ACCORDANCE WITH VSF COATING SYSTEM (SEE NOTE)

EST MASS: 16225.23kg
SHEET 1 OF 8
A1 SHEET

DATE: 13/08/2015
DRAWN: DG
CHECKED: ML

LARGE DIAMETER DRILLING LTD.
KERREK HOUSE
TOLVADDON BUSINESS PARK
CAMBORNE, CORNWALL
TR14 0HZ
TEL: 01209 861930
FAX: 01209 861110

DESCRIPTION: MUD FOOT FABRICATION

DRAWING NUMBER: A1000-00193

REV: 01

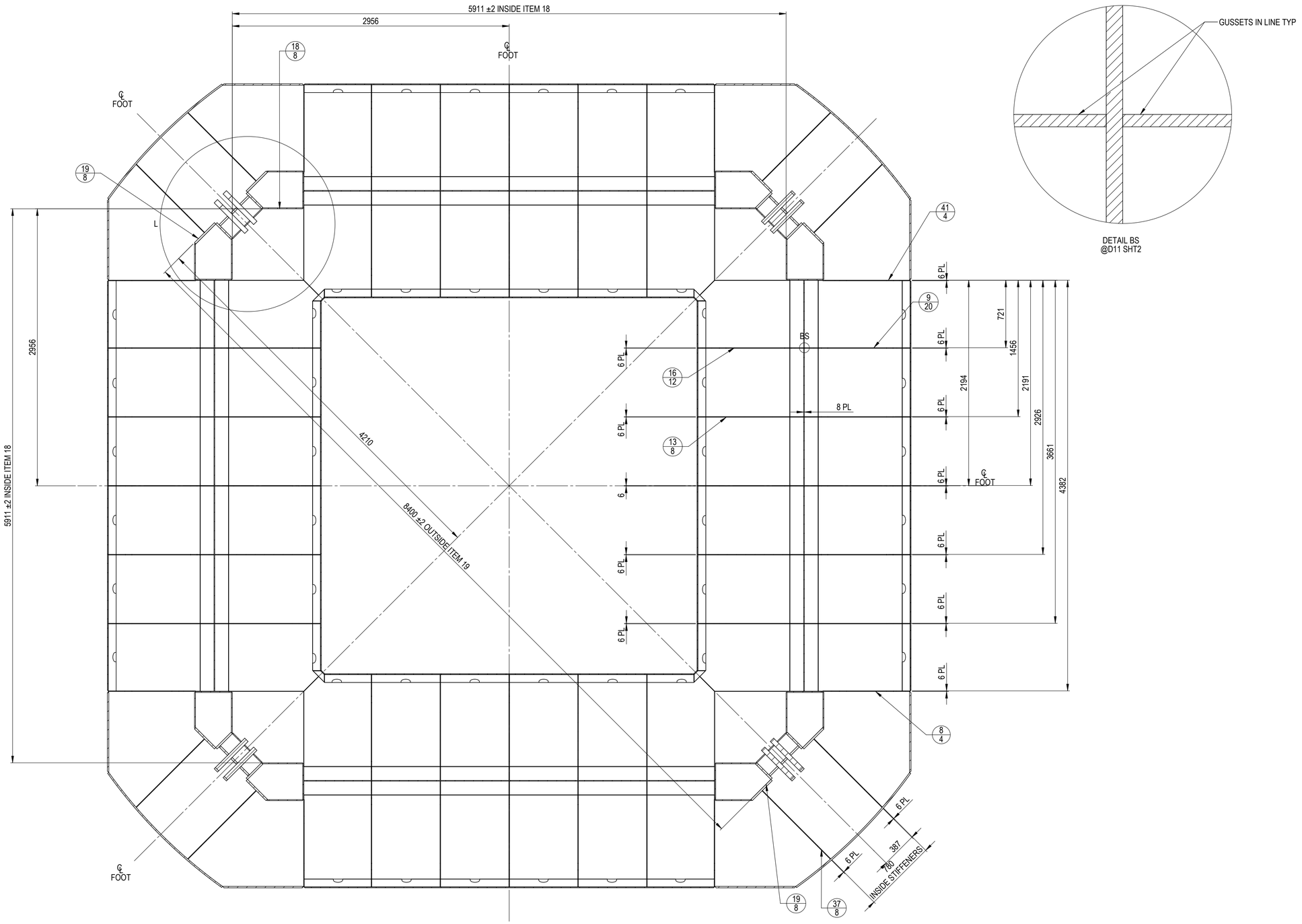

SECTION J-J
SHOWING PLAN SET OUT OF STIFFENERS AND CORNER POSTS

3rd ANGLE PROJECTION

STEEL DETAILS NOT DIMENSIONED OR TOLERANCED ON DRAWING TO BE IN ACCORDANCE WITH BS EN 1090-2:2008+A1:2011

ALL DIMS IN mm U.O.S | DO NOT SCALE

GENERAL FABRICATION TOLERANCES
UP TO 1000 ±1.0
OVER 1000 UP TO 5000 ±2.0
OVER 5000 ±5.0
ANGULAR ±0.5
REMOVE ALL BURS AND SHARP EDGES 1.0 MAX

GENERAL MACHINING TOLERANCES
0 ±2.0 0.00 ±0.3
0.0 ±1.0 ANGULAR ±0.5°
SURFACE FINISH 3.2µm Ra MIN
REMOVE ALL BURS AND SHARP EDGES 0.3 MAX
UNSPECIFIED TOOL RADS R0.8

MATERIAL TYPE: N/A
MATERIAL SPEC: N/A
FINISH: PAINT IN ACCORDANCE WITH VSF COATING SYSTEM (SEE NOTE)

EST MASS: 16225.23kg
SHEET 2 OF 8
A1 SHEET

DATE: 13/08/2015
DRAWN: DG
CHECKED: ML

LARGE DIAMETER DRILLING LTD.
KERREK HOUSE
TOLVADDON BUSINESS PARK
CAMBORNE, CORNWALL
TR14 0HZ
TEL: 01209 861930
FAX: 01209 861110

DESCRIPTION: MUD FOOT FABRICATION

DRAWING NUMBER: A1000-00193

REV: 01

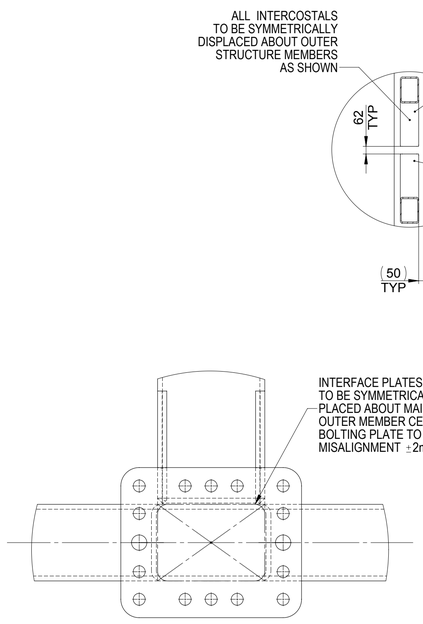

DETAIL DG

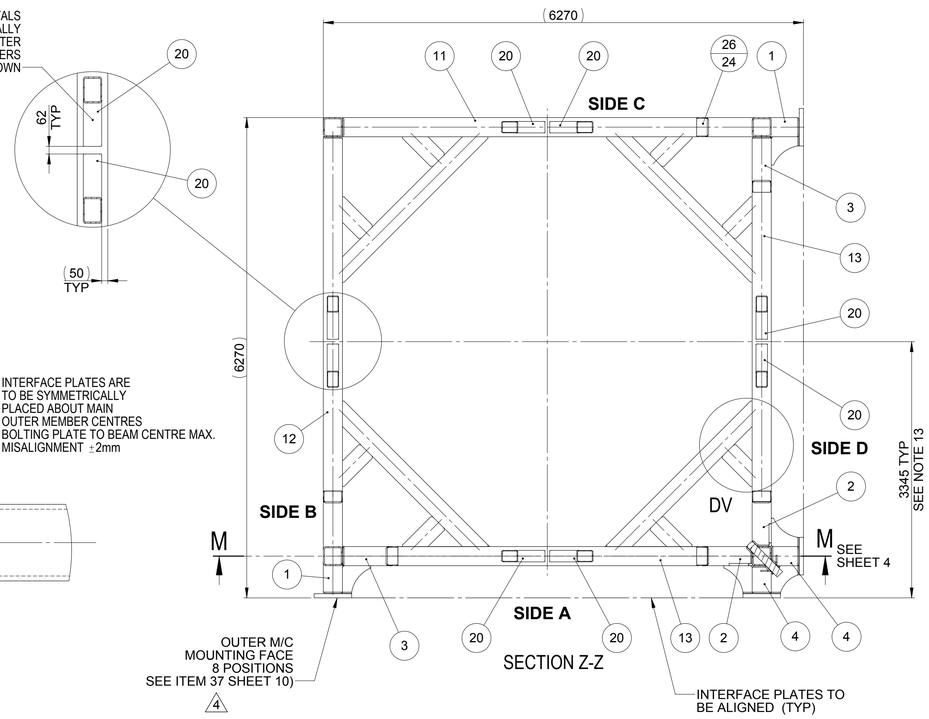

SECTION Z-Z

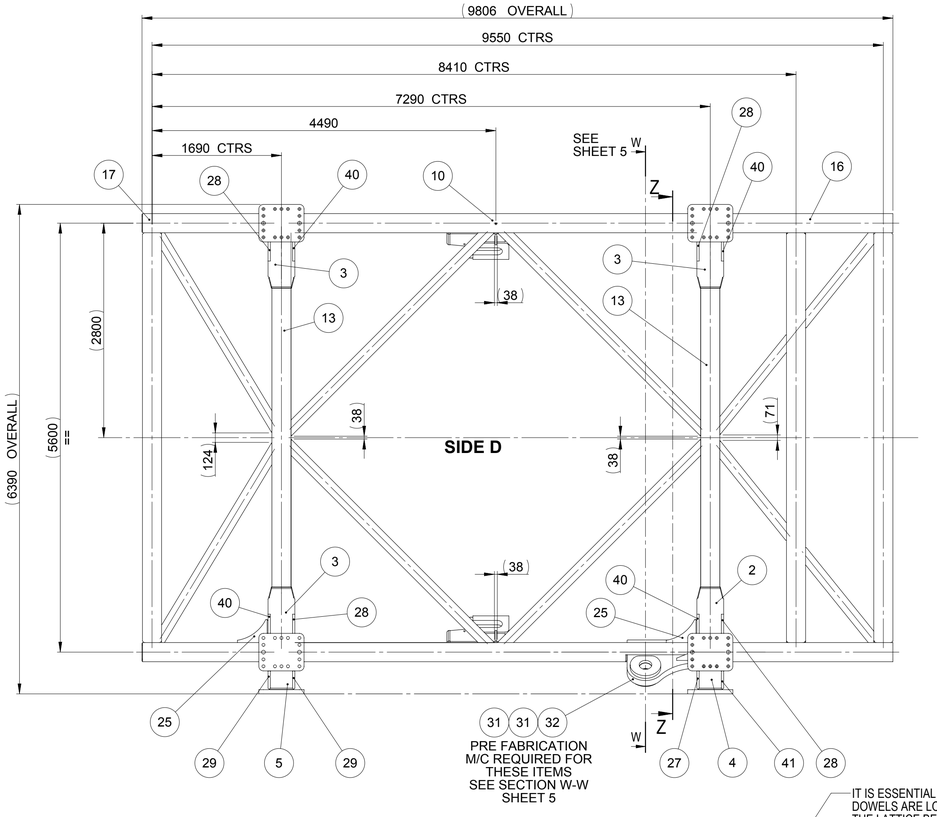

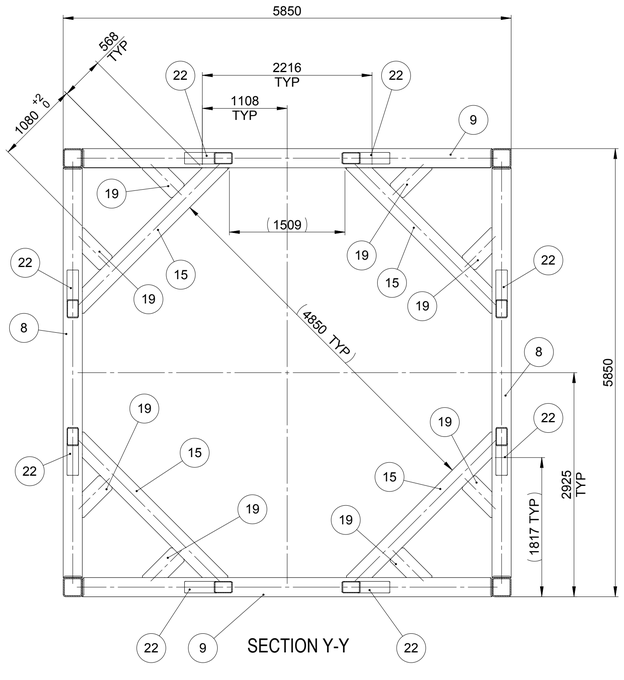

SECTION Y-Y

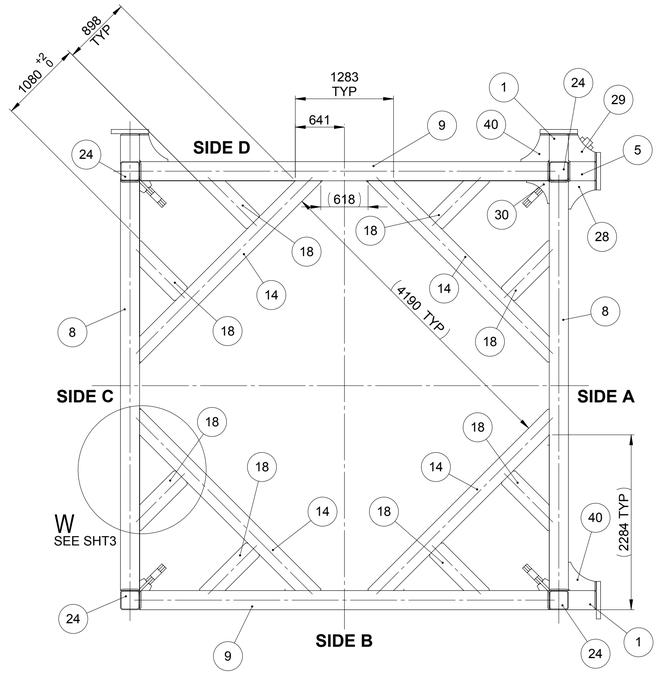

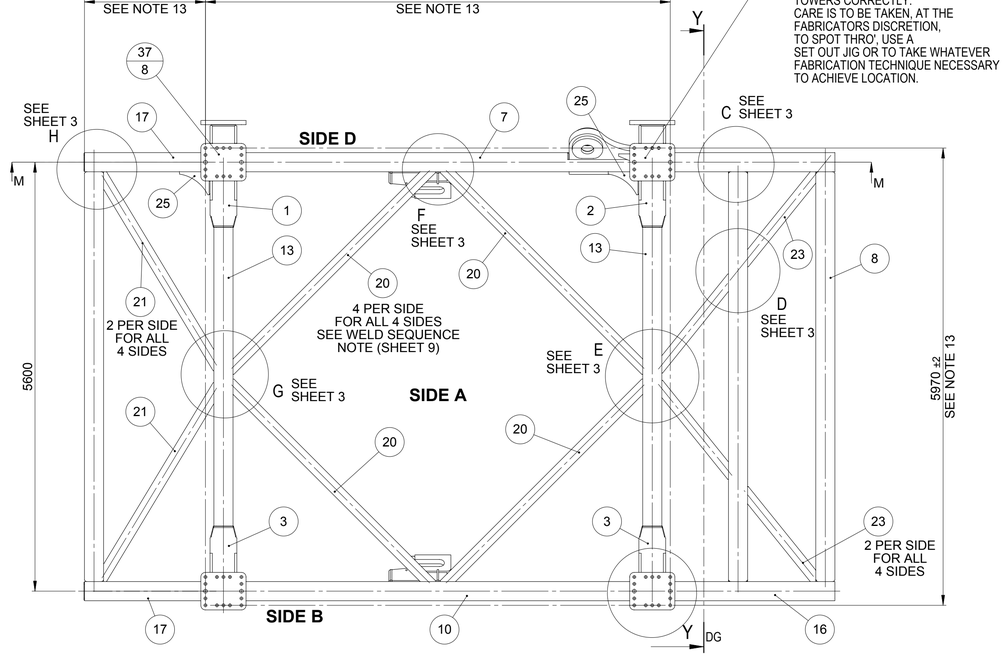

3rd ANGLE PROJECTION	STEEL DETAILS NOT DIMENSIONED OR TOLERANCED ON DRAWING TO BE IN ACCORDANCE WITH BS EN 1090-2:2008+A1:2011	GENERAL FABRICATION TOLERANCE IN ACCORDANCE WITH TABLE D2.7 ANNEX D OF EN1090-2 REMOVE ALL BURS AND SHARP EDGES 1.0 MAX	GENERAL MACHINING TOLERANCES 0 ±2.0 0.00 ±0.3 0.0 ±1.0 ANGULAR ±0.5 ° SURFACE FINISH 3.2µm Ra MIN REMOVE ALL BURS AND SHARP EDGES 0.3 MAX UNSPECIFIED TOOL RADS R0.8	MATERIAL TYPE SEE DRAWING	EST MASS 26292.81kg
	ALL DIMS IN mm U.O.S / DO NOT SCALE			MATERIAL SPEC SEE DRAWING	SHEET 2 OF 10
				FINISH SEE DRAWING	A1 SHEET

LARGE DIAMETER DRILLING LTD.
KERREK HOUSE
TOLVADDON BUSINESS PARK
CAMBORNE, CORNWALL
TR14 0HZ
TEL: 01209 861930
FAX: 01209 861110

DESCRIPTION	DRAWING NUMBER	REV	DATE	DRAWN	CHECKED
TOWER STAGE 1 PRIMARY WELDMENT	A1000-00185	05	10/08/2015	RM	DJ

FABRICATION NOTES

1. THE FOLLOWING NOTES APPLY EXCEPT WHERE OTHERWISE DETAILED ON THE DRAWING.
2. MATERIAL U.O.S: ALL HOLLOW SECTION TO A MINIMUM OF S355J2H AND ALL PLATE TO EN 100025:S355J2+N.
3. FOR TOLERANCES SEE STANDARD BORDER NOTES U.O.S.
4. PLATES ARE DETAILED ON SEPERATE DRAWINGS.
5. THE FABRICATION IS TO BE FULLY SEALED WITH WELDS CAPABLE OF WITHSTANDING 5 BAR PRESSURE SUBMERGED PRESSURE.
6. U.O.S. ALL WELDS ARE SINGLE PASS FILLET WELDS, MINIMUM THROAT THICKNESS (a) 6mm.
7. NO WEAVING PERMITTED. WELDS GREATER THAN 6mm THROAT ARE TO BE BUILT UP WITH STRINGER BEADS.
8. WELDERS ARE TO BE CODED AS A MINIMUM TO BS EN 287 -1 : 2011.
9. WELDING CONSUMABLE YIELD STRENGTH TO BE A MINIMUM OF 420MPa.
10. WELD DETAIL AND TESTING TO BE IN ACCORDANCE WITH EN10901-2:2008A1:2011, EXECUTION CLASS 3 AND ISO 3834-2:2006 AND VSF NDT PLAN- DOCUMENT NO. W15-027-80.4
    - 10.1. VISUAL CHECK 100%.
    - 10.2. PRIMARY FULL PEN WELDS TO BE 100% UT TESTED.
    - 10.3. SECONDARY FULL PEN WELDS TO BE 100% UT TESTED.
    - 10.4. LIFT POINT WELDS TO BE 100% UT TESTED OR IF FILLET WELDS TO BE100% MT TESTED.
    - 10.5. FILLET WELDS TO BE 100% MT (MPI) TESTED.
11. LIFT POINTS AND PAD EYES.
    - 11.1. LIFT POINTS ARE CLEARLY INDICATED WITH A SWL.
    - 11.2. SWL TO BE HARD STAMPED ADJACENT TO THE EYE, 10mm HIGH TEXT MIN.
12. TESTING IN ACCORDANCE WITH DNV STANDARD FOR CERTIFICATION No. 2.22 LIFTING APPLIANCES
13. TO BE SET UP IN CONJUNCTION WITH THE TOWERS IN ORDER TO ENSURE DOWEL LOCATION, FABRICATION ALIGNMENT AND OVERALL TOWER CENTRE TO CENTRE TOLERANCE PROVIDED ON DRAWING A1000-00173

PART NO.	ITEM NO.	QTY.	DESCRIPTION	LENGTH PER ITEM	
A1000-00161-1	1	8	350 x 250 x 16.0	1125	
A1000-00161-2	2	8	350 x 250 x 16.0	573	
A1000-00161-2	3	4	250 x 250 x 16.0	11800	
A1000-00161-4	4	4	250 x 250 x 16.0	5250	
A1000-00161-5	5	4	250 x 250 x 16.0	4200	
A1000-00161-6	6	4	250 x 250 x 16.0	2127	
A1000-00161-7	7	2	150 x 150 x 8.0	7620	
A1000-00161-8	8	2	150 x 150 x 8.0	7495	
A1000-00161-9	9	4	150 x 150 x 8.0	7280	
A1000-00161-10	10	4	150 x 150 x 8.0	7255	
A1000-00161-11	11	4	150 x 150 x 8.0	7218	
A1000-00161-12	12	4	150 x 150 x 8.0	3735	
A1000-00161-13	13	4	150 x 150 x 8.0	3673	
A1000-00161-14	14	16	150 x 150 x 8.0	3572	
A1000-00161-15	15	4	150 x 150 x 8.0	3546	
A1000-00161-16	16	8	150 x 150 x 8.0	5350	
A1000-00161-17	17	4	150 x 150 x 8.0	3509	
A1000-00161-18	18	28	8mm PLATE		
A1000-00161-19	19	4	20mm PLATE		
A1000-00161-20	20	8	20mm PLATE		
A1000-00161-21	21	4	30mm PLATE		
A1000-00161-22	22	32	15mm PLATE		
A1000-00161-23	23	32	15mm PLATE		
A1000-00161-24	24	4	60mm PLATE		
A1000-00161-25	25	4	20mm PLATE		
A1000-00161-26	26	8	20mm PLATE		
A1000-00161-27	27	4	60mm PLATE		
A1000-00161-28	28	4	12mm PLATE		
A1000-00161-29	29	8	10mm PLATE		
A1000-00161-30	30	8	10mm PLATE		
A1000-00161-31	31	16	10mm PLATE		11 ADDED
A1000-00161-32	32	16	10mm PLATE		11 ADDED
A1000-00376	33	2	SUB ASSEMBLY		11 ADDED
A1000-00355	34	2	SUB ASSEMBLY		11 ADDED

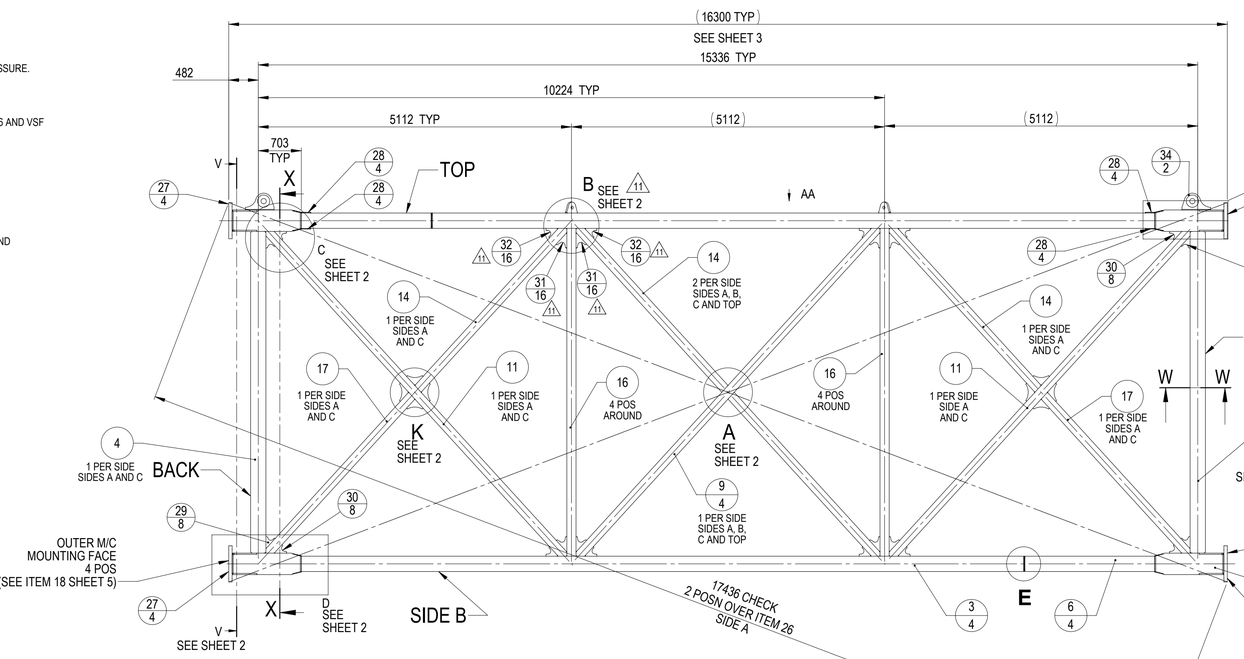

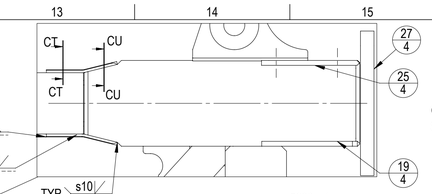

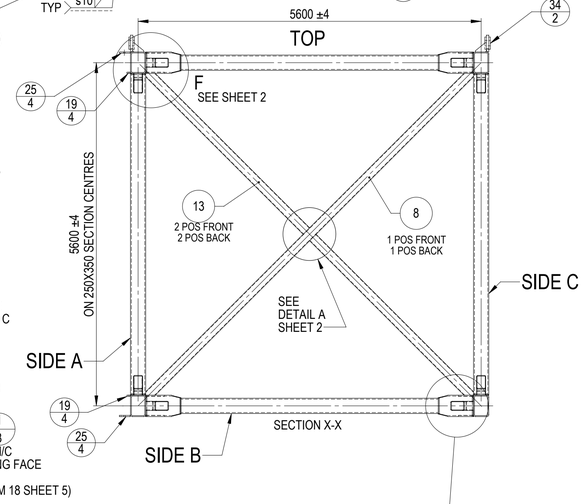

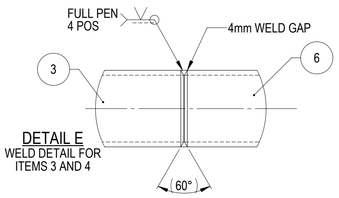

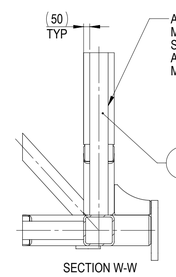

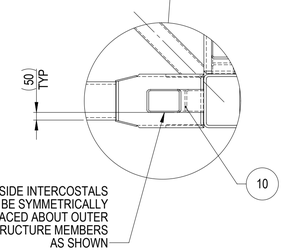

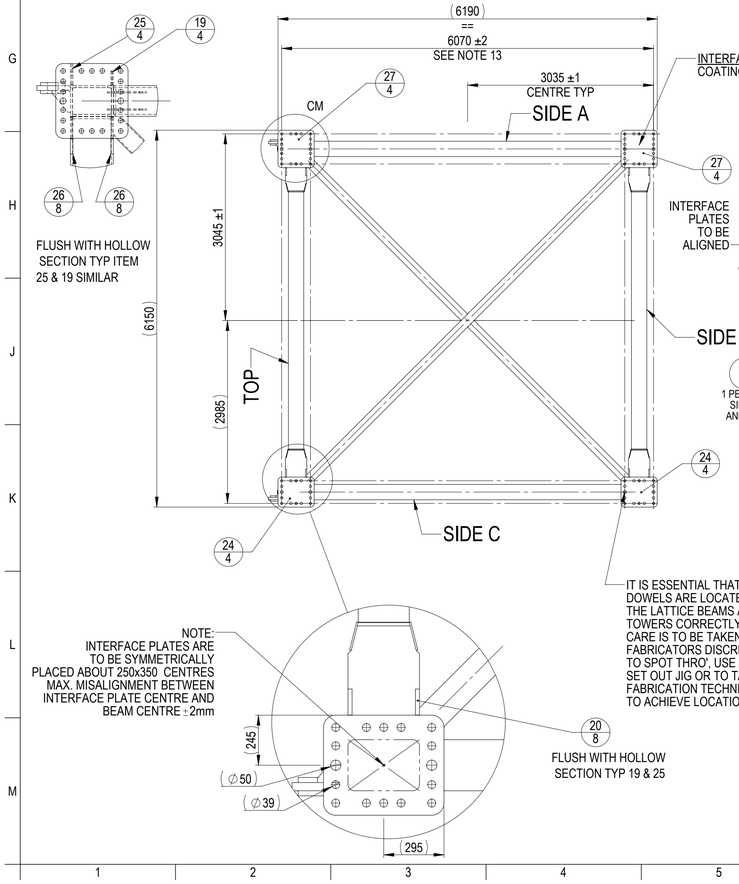

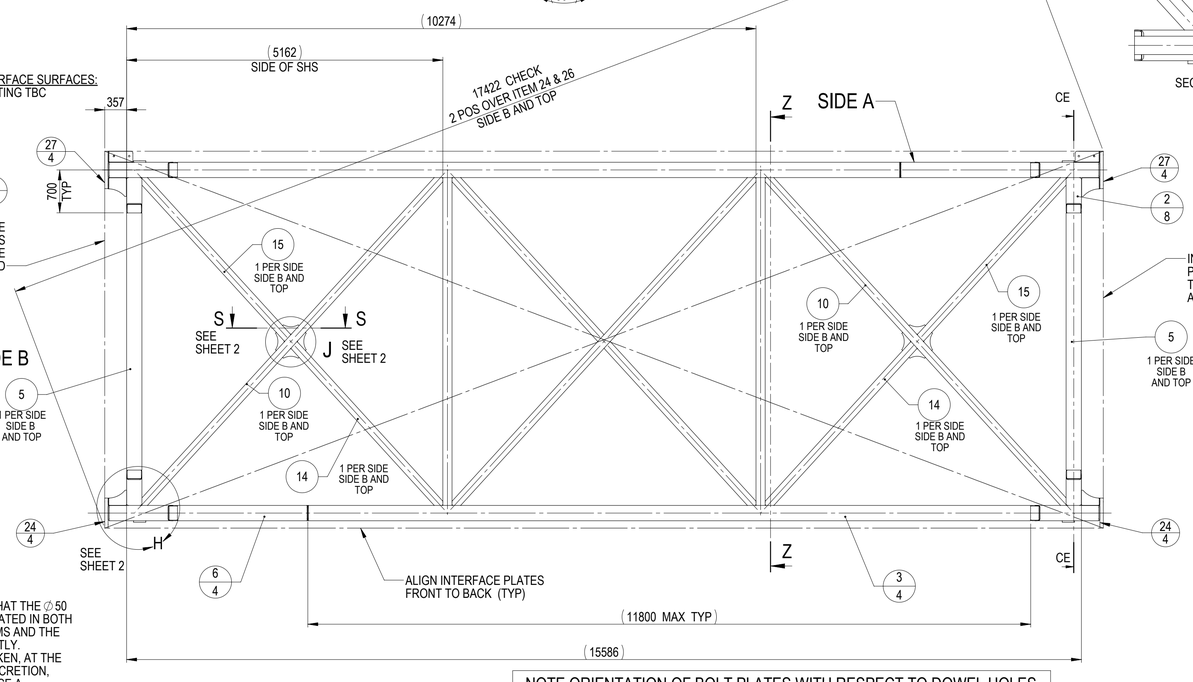

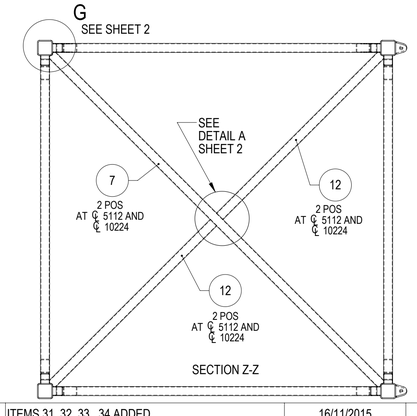

NOTE ORIENTATION OF BOLT PLATES WITH RESPECT TO DOWEL HOLES

REV.	DESCRIPTION	DATE	INITIALS
11	ITEMS 31, 32 ,33 , 34 ADDED	16/11/2015	RM
10	ITEMS 29 & 30 ADDED	05/11/2015	RM
9	ITEM 28 AND ITEM 25 CHANGED	03/11/2015	AF
8	VSF COMMENTS	29/10/2015	AF
7	BOLTING PLATES ADDED AND PROFILE MODIFIED	27/10/2015	AF
2	FIRST RELEASE		
1	FOR INFORMATION		

REVISIONS

3rd ANGLE PROJECTION

STEEL DETAILS NOT DIMENSIONED OR TOLERANCED ON DRAWING TO BE IN ACCORDANCE WITH BS EN 1090-2:2008+A1:2011

ALL DIMS IN mm U.O.S | DO NOT SCALE

GENERAL FABRICATION TOLERANCE IN ACCORDANCE WITH TABLE D2.7 ANNEX D OF EN1090-2
REMOVE ALL BURS AND SHARP EDGES 1.0 MAX

GENERAL MACHINING TOLERANCES
0 ±2.0 0.00 ±0.3
0.0 ±1.0 ANGULAR ±0.5°
SURFACE FINISH 3.2µm Ra MIN
REMOVE ALL BURS AND SHARP EDGES 0.3 MAX
UNSPECIFIED TOOL RADS R0.8

MATERIAL TYPE: SEE DRAWING
MATERIAL SPEC: SEE DRAWING
FINISH: PAINT IN ACCORDANCE WITH VSF COATING SYSTEM A (SEE PAINTING NOTE SHEET 1)

EST MASS: 23211.57kg
DATE: 16/06/2015
SHEET 1 OF 6
DRAWN: JW
A1 SHEET
CHECKED: AF

LARGE DIAMETER DRILLING LTD.
KERREK HOUSE
TOLVADDON BUSINESS PARK
CAMBORNE, CORNWALL
TR14 0HZ
TEL: 01209 861930
FAX: 01209 861110

DESCRIPTION: LATTICE BEAM PRIMARY WELDMENT

DRAWING NUMBER: A1000-00161

REV: 11

C

Inertia properties Pre-Piling Template

Table C.1: Main structural elements in the pre-piling template

RHS 350 x 250 x 16		
h	350	mm
b	250	mm
t	16	mm
I_y	3.00E+08	mm^4
I_z	1.76E+08	mm^4
A	17900	mm^2
ρ	1.36E+02	kg/m
SHS 250 x 250 x 16		
h	250	mm
b	250	mm
t	16	mm
I_y	1.33E+08	mm^4
I_z	1.33E+08	mm^4
A	14700	mm^2
ρ	1.11E+02	kg/m

- Center of Gravity is assumed to be in the centre of the x-y plane
- Center of Gravity is assumed at half of the height of the lattice beams
- Only main structural elements are considered of the outer shelf of the towers, lattice beams and the mud mats.

This appendix provides an approximation of the second order moment of area and the mass moment of inertia of the pre-piling template. The numbered elements in the following tables are equal numbers of the elements as used in the structural drawings of the template given in Appendix X. The second order moment of area incorporates the Rule of Steinar. The following equations are used to compute the S.o.M. of area and the mass moment of inertia.

$$I'_y = I_y + a^2 A \tag{C.1}$$

$$I_{m,y} = \int_A \rho(x,y,z) \cdot (y_2 - y_1) \cdot x^2 dx \tag{C.2}$$

Table C.2: Second order moment of Area of a single mud mat

Mud mat				
Element	I_y [mm^4]	a [mm]	A [mm^2]	I'_y [mm^4]
Mud mat	2007843.75	6365	1.07E+05	4.34E+12

Table C.3: Second order moment of Area of the lattice beam at the aft

Lattice beam (aft)				
Element	I_y [mm^4]	a [mm]	A [mm^2]	I'_y [mm^4]
1	3.00E+08	2800	17900	1.41E+11
2	3.00E+08	2800	17900	1.41E+11
3	1.33E+08	2800	14700	1.15E+11
4	1.33E+08	0	14700	1.33E+08
5	1.33E+08	2800	14700	1.15E+11
6	1.33E+08	2800	14700	1.15E+11
Top section:				
Elements at corner		1.13E+12	(8 p.)	
Horizontal beams		6.92E+11	(6 p.)	
Bottom section:				
Elements at corner		1.13E+12	(8 p.)	
Horizontal beams		6.92E+11	(6 p.)	
Vertical beams		5.32E+08	(4 p.)	

Table C.4: Second order moment of Area of the lattice beam at the PS & SB

Lattice beam (PS & SB)				
Element	I_y [mm^4]	a [mm]	A [mm^2]	I'_y [mm^4]
1	3.00E+08	2800	17900	1.41E+11
2	3.00E+08	2800	17900	1.41E+11
3	1.33E+08	2800	14700	1.15E+11
4	1.33E+08	0	14700	1.33E+08
5	1.33E+08	2800	14700	1.15E+11
6	1.33E+08	2800	14700	1.15E+11
Top section:				
Elements at corner		1.13E+12	(8 p.)	
Horizontal beams		6.92E+11	(6 p.)	
Bottom section:				
Elements at corner		1.13E+12	(8 p.)	
Horizontal beams		6.92E+11	(6 p.)	
Vertical beams		5.32E+08	(4 p.)	

Table C.5: Second order moment of Area of a single tower

Tower				
Element	I_y [mm^4]	a [mm]	A [mm^2]	I'_y [mm^4]
1	3.00E+08	2800	17900	1.41E+11
2	3.00E+08	2800	17900	1.41E+11
3	3.00E+08	2800	17900	1.41E+11
6	1.33E+08	285	14700	1.33E+09
7	1.33E+08	1280	14700	2.42E+10
8	1.33E+08	4490	14700	2.96E+11
9	1.33E+08	4490	14700	2.96E+11
10	1.33E+08	0	14700	1.33E+08
11	1.33E+08	2800	14700	1.15E+11
12	1.33E+08	2800	14700	1.15E+11
13	1.33E+08	2800	14700	1.15E+11
16	1.33E+08	4080	14700	2.45E+11
17	1.33E+08	3795	14700	2.12E+11
Lower part				
8 (upper)	1.33E+08	4080	14700	2.45E+11
8 (lower)	1.33E+08	5060	14700	3.77E+11
9 (upper)	1.33E+08	4080	14700	2.45E+11
9 (lower)	1.33E+08	5060	14700	3.77E+11
Top section:				
Elements on corners		8.44E+11	(6 p.)	
Horizontal beams		1.65E+12	(8 p.)	
Bottom section:				
Elements on corners		8.44E+11	(6 p.)	
Horizontal beams		2.95E+12	(12 p.)	
Vertical beams		1.15E+12	(9 p.)	

Table C.6: Approximation of the Second order moment of Area of the pre-piling template

Pre-piling template			
Element	I'_y [mm^4]	Amount	Total I'_y [mm^4]
Mud mats	4.34E+12	4	1.74E+13
Lattice beam (Fore/Aft)	3.64E+12	2	7.27E+12
Lattice beam (PS/SB)	3.64E+12	2	7.27E+12
Towers	7.43E+12	4	2.97E+13
TOTAL			6.16E+13

Table C.7: Mass moment of inertia of a single tower

Tower					
Outer section					
Element	ρ [kg/m]	dx [m]	x [m]	$I_{m,y}[kg \cdot m^2]$	
1	1.36E+02	1.332	14.3	3.70E+04	
8	1.11E+02	5.35	14.3	1.21E+05	
11	1.11E+02	4.625	14.3	1.05E+05	
Intermediate section					
Element	ρ [kg/m]	dx [m]	x [m]	$I_{m,y}[kg \cdot m^2]$	
3 (outer)	1.36E+02	0.717	13.8165	1.86E+04	
13	1.11E+02	3.9	11.508	5.73E+04	
3 (inner)	1.36E+02	0.717	9.2	8.25E+03	
12	1.11E+02	4.625	11.8625	7.22E+04	
1 (inner)	1.36E+02	1.332	8.884	1.43E+04	
9	1.11E+02	5.35	11.5	7.85E+04	
2 (inner)	1.36E+02	0.717	9.2	8.25E+03	
Inner section					
Element	ρ [kg/m]	dx [m]	x [m]	$I_{m,y}[kg \cdot m^2]$	
1	1.36E+02	1.332	8.7	1.37E+04	
8	1.11E+02	5.35	8.7	4.49E+04	
3	1.36E+02	0.717	8.7	7.38E+03	
13	1.11E+02	3.9	8.7	3.28E+04	
2	1.36E+02	0.717	8.7	7.38E+03	
		Outer section		6.48E+05	(7 p.)
		Intermediate section		8.13E+05	(16 p.)
		Inner section		2.36E+05	(10 p.)

Table C.8: Mass moment of inertia of the lattice beams at fore/aft and at portside/starboard

Lattice beam					
Fore & Aft					
Outer section					
Element	ρ [kg/m]	dx [m]	x [m]	$I_{m,y}[kg \cdot m^2]$	
1	1.36E+02	1.125	14.3	3.13E+04	
3	1.11E+02	11.8	14.3	2.68E+05	
6	1.11E+02	2.127	14.3	4.83E+04	
Intermediate section					
Element	ρ [kg/m]	dx [m]	x [m]	$I_{m,y}[kg \cdot m^2]$	
5	1.11E+02	4.2	11.5	6.17E+04	
2 (outer)	1.36E+02	0.573	13.8165	1.49E+04	
2 (inner)	1.36E+02	0.573	9.11	6.47E+03	
Inner section					
Element	ρ [kg/m]	dx [m]	x [m]	$I_{m,y}[kg \cdot m^2]$	
1	1.36E+02	1.125	8.7	1.16E+04	
3	1.11E+02	11.8	8.7	9.91E+04	
6	1.11E+02	2.127	8.7	1.79E+04	
		Outer section		7.57E+05	(8 p.)
		Intermediate section		3.32E+05	(12 p.)
		Inner section		2.80E+05	(8 p.)
Portside & Starboard					
Outer section					
Element	ρ [kg/m]	dx [m]	x [m]	$I_{m,y}[kg \cdot m^2]$	
1	1.36E+02	1.125	7.5875	8.81E+03	
3	1.11E+02	11.8	1.125	1.66E+03	
6	1.11E+02	2.127	5.9615	8.39E+03	
Intermediate section					
Element	ρ [kg/m]	dx [m]	x [m]	$I_{m,y}[kg \cdot m^2]$	
5	1.11E+02	4.2	7.668	2.74E+04	
2	1.36E+02	0.573	7.668	4.58E+03	
Inner section					
Element	ρ [kg/m]	dx [m]	x [m]	$I_{m,y}[kg \cdot m^2]$	
1	1.36E+02	1.125	7.5875	8.81E+03	
3	1.11E+02	11.8	1.125	1.66E+03	
6	1.11E+02	2.127	5.9615	8.39E+03	
		Outer section		5.53E+04	(8 p.)
		Intermediate section		1.46E+05	(12 p.)
		Inner section		5.53E+04	(8 p.)

Table C.9: Mass moment of inertia of a single mud mat

Mud mats				
Element	$\rho[kg/m^2]$	dx*dy [m^2]	x [m]	$I_{m,y}[kg \cdot m^2]$
Mud mat	318.3	50.97	11.5	8.39E+03

Table C.10: Approximation of the Mass moment of inertia of the pre-piling template

Pre-piling template			
Element	$I_{m,y}$ [kg $\cdot m^2$]	Amount	Total $I_{m,y}$ [kg $\cdot m^2$]
Mud mats	8.39E+03	4	3.36E+04
Lattice beam (Fore/Aft)	1.37E+06	2	2.74E+06
Lattice beam (PS/SB)	2.57E+05	2	5.14E+05
Towers	1.70E+06	4	6.79E+06
TOTAL			1.01E+07

D

Effect of changing operational limits - diagonal loading case

Single clay layer

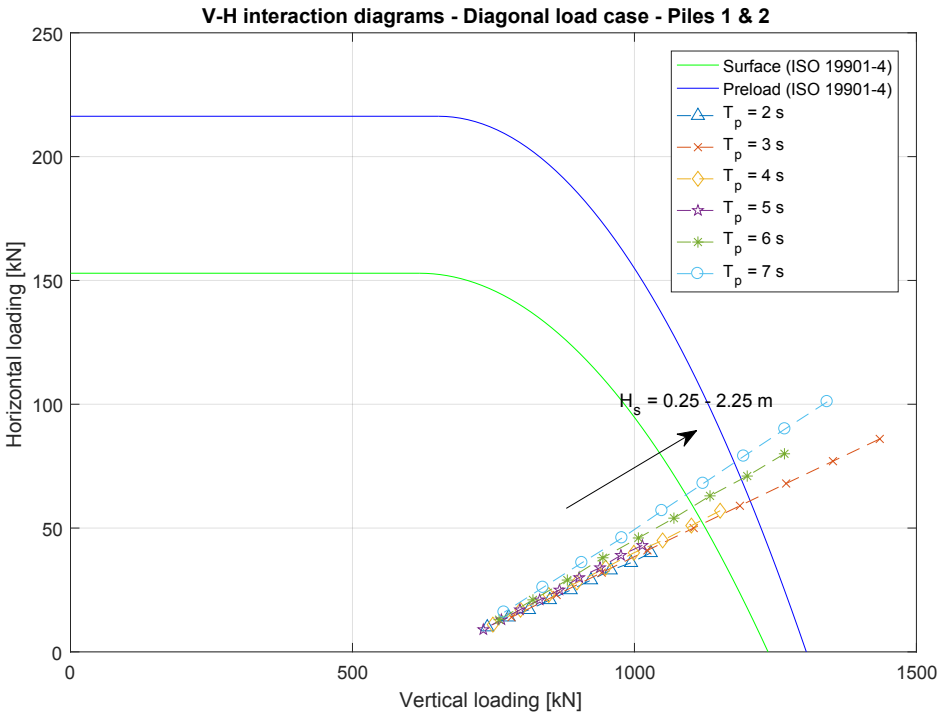

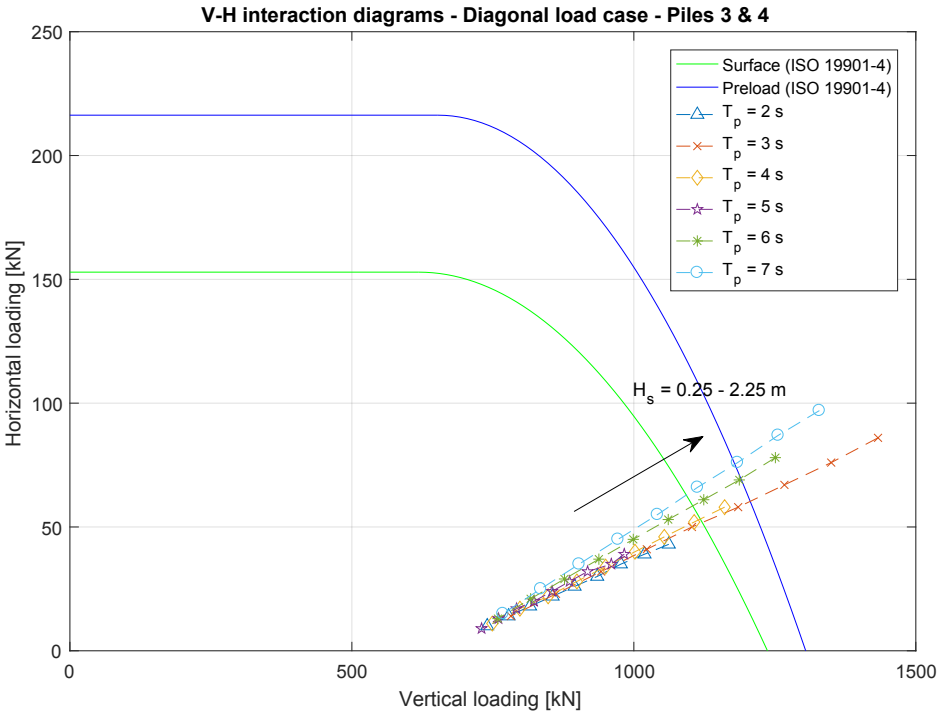
V-H interaction diagrams - Diagonal load case - Piles 3 & 4
Surface (ISO 19901-4)
Preload (ISO 19901-4)
T_p = 2 s
T_p = 3 s
T_p = 4 s
T_p = 5 s
T_p = 6 s
T_p = 7 s
H_s = 0.25 - 2.25 m
Horizontal loading [kN]
Vertical loading [kN]
0
50
100
150
200
250
0
500
1000
1500

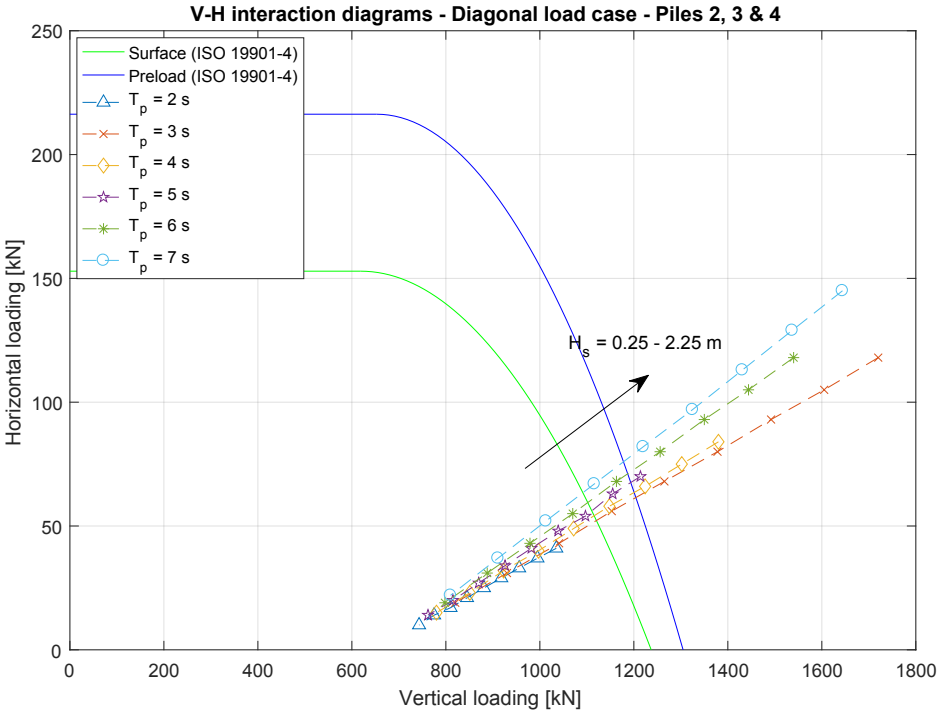
V-H interaction diagrams - Diagonal load case - Piles 2, 3 & 4
Surface (ISO 19901-4)
Preload (ISO 19901-4)
T_p = 2 s
T_p = 3 s
T_p = 4 s
T_p = 5 s
T_p = 6 s
T_p = 7 s
H_s = 0.25 - 2.25 m
Horizontal loading [kN]
Vertical loading [kN]
0
50
100
150
200
250
0
200
400
600
800
1000
1200
1400
1600
1800

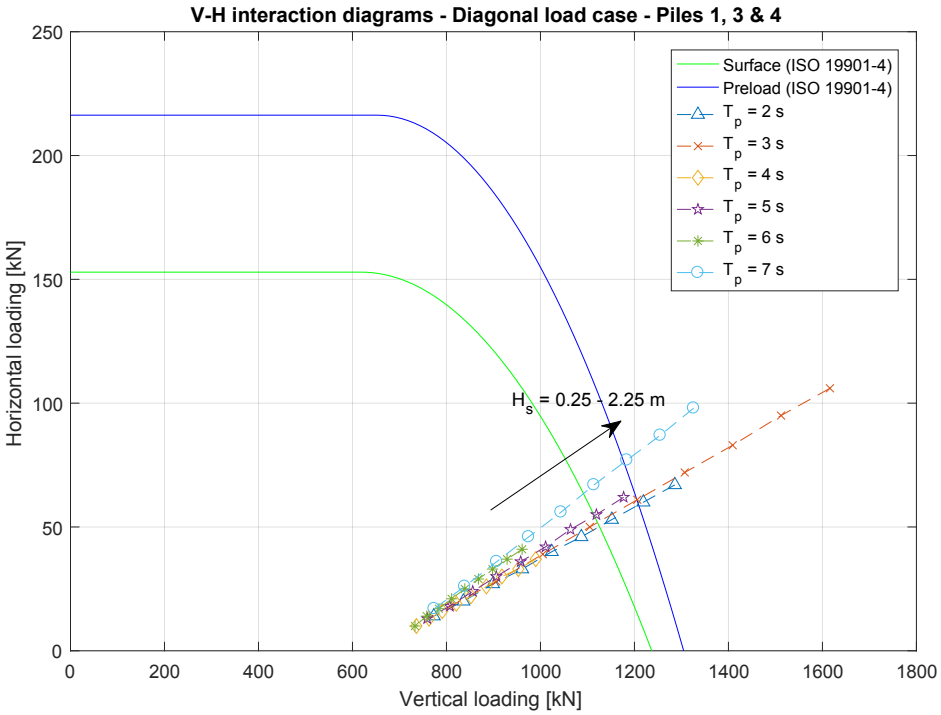
V-H interaction diagrams - Diagonal load case - Piles 1, 3 & 4
Surface (ISO 19901-4)
Preload (ISO 19901-4)
T_p = 2 s
T_p = 3 s
T_p = 4 s
T_p = 5 s
T_p = 6 s
T_p = 7 s
H_s = 0.25 - 2.25 m
Horizontal loading [kN]
Vertical loading [kN]
0
50
100
150
200
250
0
200
400
600
800
1000
1200
1400
1600
1800

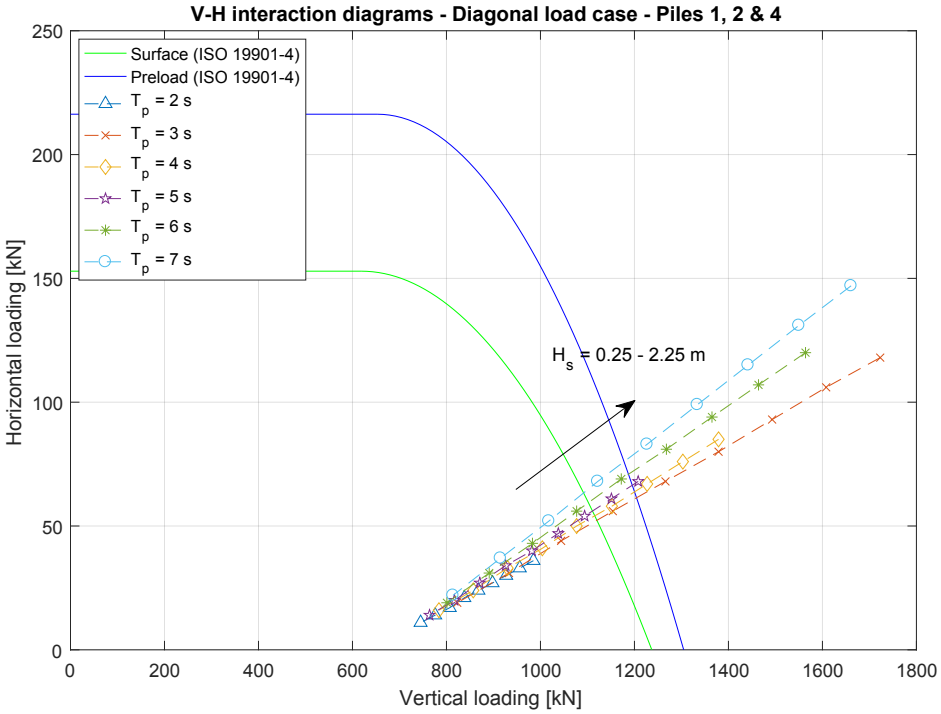
V-H interaction diagrams - Diagonal load case - Piles 1, 2 & 4
Surface (ISO 19901-4)
Preload (ISO 19901-4)
T_p = 2 s
T_p = 3 s
T_p = 4 s
T_p = 5 s
T_p = 6 s
T_p = 7 s
H_s = 0.25 - 2.25 m
Horizontal loading [kN]
Vertical loading [kN]
0
50
100
150
200
250
0
200
400
600
800
1000
1200
1400
1600
1800

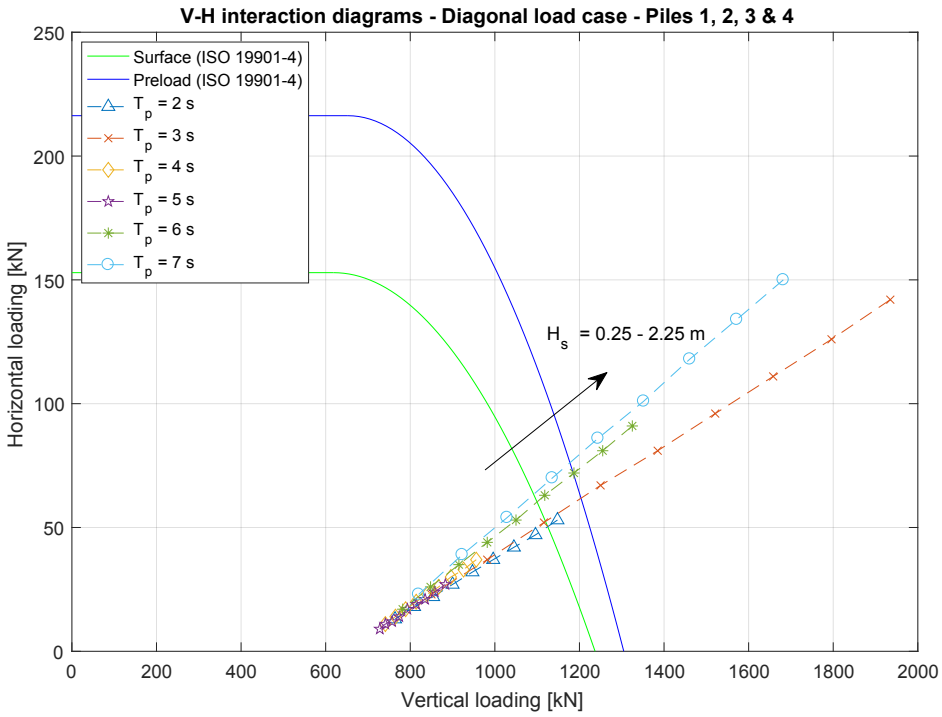
V-H interaction diagrams - Diagonal load case - Piles 1, 2, 3 & 4
Surface (ISO 19901-4)
Preload (ISO 19901-4)
T_p = 2 s
T_p = 3 s
T_p = 4 s
T_p = 5 s
T_p = 6 s
T_p = 7 s
H_s = 0.25 - 2.25 m
Horizontal loading [kN]
Vertical loading [kN]
0
50
100
150
200
250
0
200
400
600
800
1000
1200
1400
1600
1800
2000

Double layered system

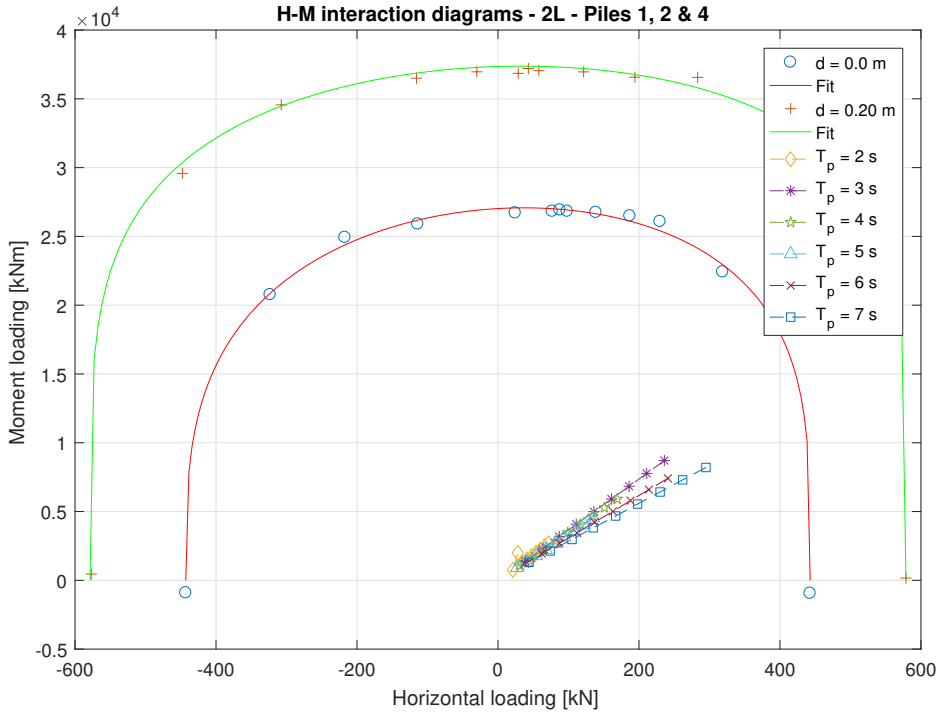

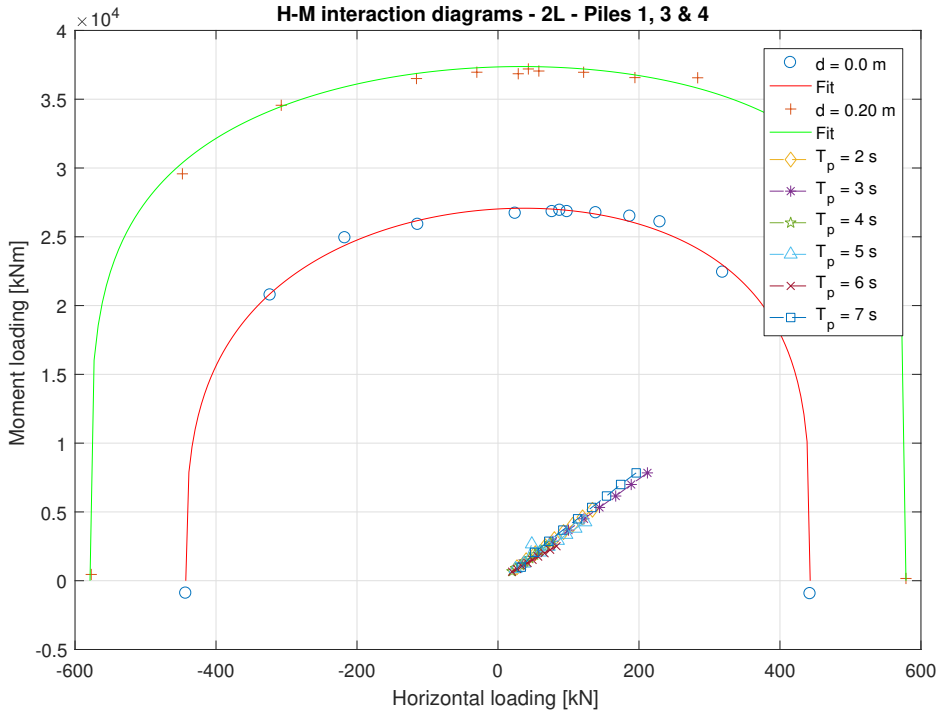

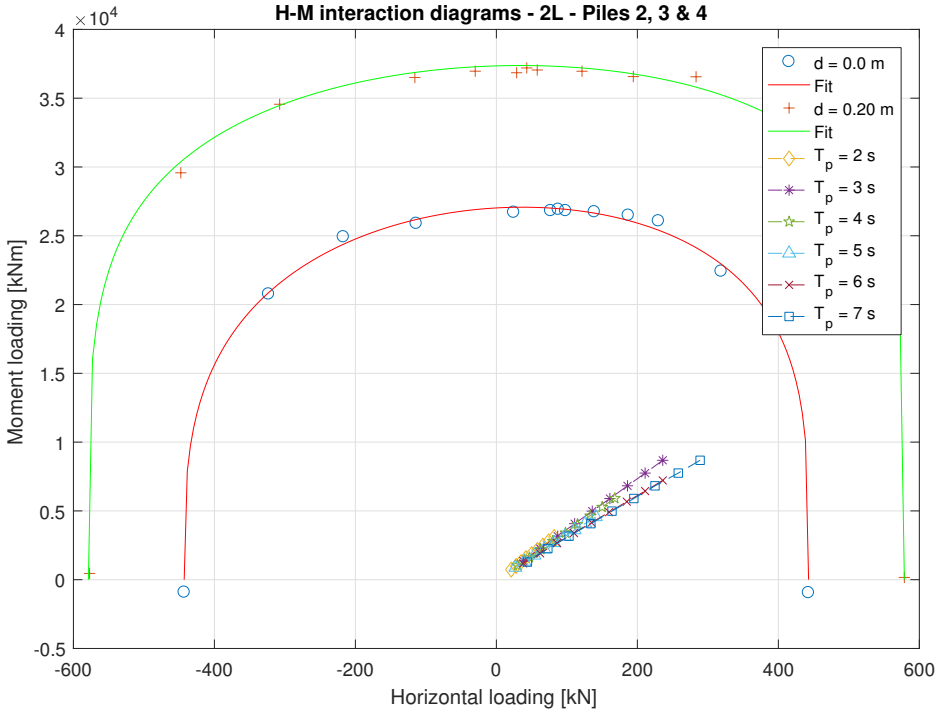
H-M interaction diagrams - 2L - Piles 2, 3 & 4
×10^4
Moment loading [kNm]
Horizontal loading [kN]
d = 0.0 m
Fit
d = 0.20 m
Fit
T_p = 2 s
T_p = 3 s
T_p = 4 s
T_p = 5 s
T_p = 6 s
T_p = 7 s

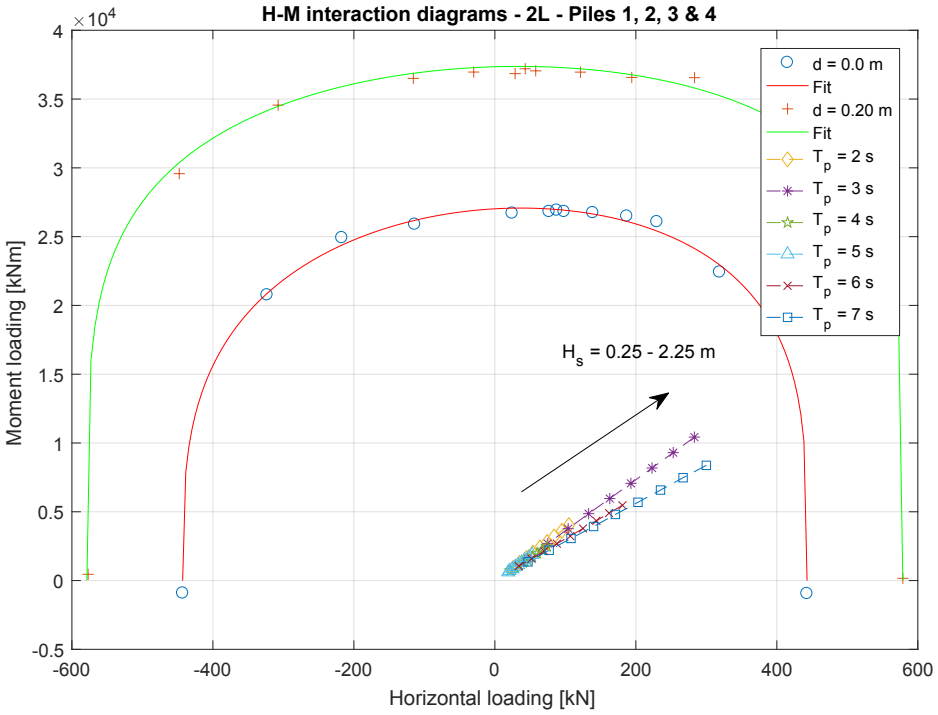
H-M interaction diagrams - 2L - Piles 1, 2, 3 & 4
×10^4
Moment loading [kNm]
Horizontal loading [kN]
d = 0.0 m
Fit
d = 0.20 m
Fit
T_p = 2 s
T_p = 3 s
T_p = 4 s
T_p = 5 s
T_p = 6 s
T_p = 7 s
H_s = 0.25 - 2.25 m

Bibliography

[1] M F. Bransby and M. F. Randolph. The Effect of Embedment Depth on the Undrained Response of Skirted Foundations to Combined Loading. *Japanese Geotechnical Society*, 39(4):19–33, 1999. ISSN 09168451. doi: 10.1248/cpb.37.3229.

[2] J. Brinch - Hansen. A Revised and Extended Formula for Bearing Capacity - Bulletin No. 28. Technical Report 28, Copenhagen, 1970.

[3] R. Butterfield. Standardized sign conventions and notation for generally loaded foundations. (January), 1997. doi: 10.1680/geot.1997.47.5.1051.

[4] G. Clauss. *Offshore structures, Volume 1, Conceptual Design and Hydromechanics*. Springer, London, UK., 1992.

[5] D. H. Edwards, L. Zdravkovic, and D. M. Potts. Depth factors for undrained bearing capacity. *Géotechnique*, 55(10):755–758, 2005. ISSN 0016-8505. doi: 10.1680/geot.2005.55.10.755.

[6] H. K. Engin. *Modelling Pile Installation Effects - A Numerical Approach*. Ph.d. thesis, Delft University of Technology, Delft, 2013.

[7] EWEA. 2050 : Facilitating 50 % Wind Energy - Recommendations on transmission infrastructure , system operation and electricity market integration. pages 1–11, 2011.

[8] R. Fell, P. MacGregor, D. Stapledon, and G. Bell. *Geotechnical Engineering of Dams*. CRC Press, 2005. URL `https://books.google.nl/books/about/Geotechnical{_}Engineering{_}of{_}Dams.html?id=N540YI6RA9oC{&}redir{_}esc=y`.

[9] X. Feng, M. F. Randolph, S. Gourvenec, and R. Wallerand. Design approach for rectangular mudmats under fully three- dimensional loading loading. *G{é}otechnique*, 64(January):51–63, 2014.

[10] R. Fisher and D. Cathie. Optimisation of gravity based design for subsea applications. In *International Conference on Foundations*, Dundee, 2003.

[11] G. Gazetas. Formulas and Charts for Impedances of Surface and Embedded Foundations. *Journal of Geotechnical Engineering*, 117(9):19, 1991.

[12] S. Gourvenec. Shape effects on the capacity of rectangular footings under general loading. *Geotechnique*, 57(February):637–646, 2007. doi: 10.1680/geot.2007.57.8.637.

[13] S. Gourvenec. Failure envelopes for offshore shallow foundations under general loading. *Géotechnique*, 57(9):715–728, 2007. ISSN 0016-8505. doi: 10.1680/geot.2007.57.9.715.

[14] S. Gourvenec. Effect of embedment on the undrained capacity of shallow foundations under general loading. *Géotechnique*, 58(3):177–185, 2008. ISSN 0016-8505. doi: 10.1680/geot.2008.58.3.177.

[15] S. Gourvenec and M. Steinepreis. Undrained Limit States of Shallow Foundations Acting in Consort. *International Journal of Geomechanics*, 7(3):194–205, 2007. ISSN 1532-3641. doi: 10.1061/(ASCE)1532-3641(2007)7:3(194). URL `http://ascelibrary.org/doi/10.1061/(ASCE)1532-3641(2007)7:3(194)`.

[16] S. Gourvenec, M. F. Randolph, and O. Kingsnorth. Undrained Bearing Capacity of Square and Rectangular Footings. *International Journal of Geomechanics*, 6(May/June):147–157, 2006. ISSN 1532-3641. doi: 10.1061/(ASCE)1532-3641(2006)6:6(421).

[17] A.P. Green. The plastic yielding of metal junctions due to combined shear and pressure. *Journal of the Mechanics and Physics of Soilds*, 2(3):197–211, 1954.

[18] A. Ho, A. Mbistrova, and G. Corbetta. The European Offshore Wind Industry: Key Trends and Statistics 2015. Technical Report February, European Wind Energy Association, 2016.

[19] M. Jamiolkowski, R. Lancellotta, S. Marchetti, R. Nova, and E. Pasqualini. Design parameters for soft clays. In *Proceedings of the 7th European Conference on Soil Mechanics and Foundation Engineering*, pages 10–13, Brighton, UK, 1979.

[20] J. M. J. Journee and W. W. Massie. *Offshore Hydromechanics*. Delft University of Technology, Delft, 2001 edition. doi: 10.1097/DCC.0b013e318276822f. URL `http://www.ncbi.nlm.nih.gov/pubmed/23242823`.

[21] C. C. Ladd and R. Foot. New Design Procedure for Stability of Soft Clays (SHANSEP). *Journal of the Geotechnical Engineering Division*, pages 763–786, 1974.

[22] I. Littleton. An experimental study of the Adhesion between Clay and Steel. *Journal of Terramechanics*, 13(3):141–152, 1976. ISSN 10535357. doi: 10.1016/1053-5357(93)90011-9.

[23] B. G. Look. *Handbook of Geotechnical Investigation and Design Tables*. Taylor & Francis, London, 2007. ISBN 9788578110796. doi: 10.1017/CBO9781107415324.004.

[24] NEN. NEN-EN 1997-1+C1+A1/NB. Technical report, 2016.

[25] Plaxis. Plaxis 3D Reference Manual. Technical Report April, 2016.

[26] D. M. Potts and L. Zdravković. *Finite Element Analysis in Geotechnical Engineering, Theory*. Thomas Telford Ltd., London, 1999.

[27] J. G. Potyondy. Skin Friction between Various Soils and Construction Materials. *Géotechnique*, 11:339–353, 1961. ISSN 0016-8505. doi: 10.1680/geot.1961.11.4.339.

[28] L. Prandtl. Über die Eindringungsfestigkeit (Härte) plastischer Baustoffe und die Festigkeit von Schneiden. *Zeitschrift für Angewandte Mathematik und Mechanik*, pages 15–20, 1921.

[29] Z. Shen, X. Feng, and S. Gourvenec. Undrained capacity of surface foundations with zero-tension interface under planar V-H-M loading. *Computers and Geotechnics*, 73(July):47–57, 2016. ISSN 18737633. doi: 10.1016/j.compgeo.2015.11.024.

[30] A.W. Skempton. The Bearing Capacity of Clays. pages 180–189, London, 1951. Building Research Congress.

[31] SNAME. Guidelines for Site Specific Assessment of Mobile Jack-Up Units, 2008.

[32] H. A. Taiebat and J.P. Carter. Numerical studies of the bearing capacity of shallow foundations on cohesive soil subjected to combined loading. *Geotechnique*, 50(4):409–418, 2000. ISSN 0016-8505. doi: 10.1680/geot.2000.50.4.409.

[33] K. Terzaghi. *Theoretical Soil Mechanics*. John Wiley & Sons, Inc., New York, 1943.

[34] M. J. Tomlinson. *Foundation Design and Construction*. Pearson Education Ltd, Essex, 2 edition, 1969.